UNIVERSIDADE NOVA DE LISBOA
Faculdade de Ciências e Tecnologia

Filipe dos Santos Folgosa

Structural and Mechanistic Studies of Iron Containing Proteins

Lisboa
2008

Filipe dos Santos Folgosa

Structural and Mechanistic Studies of Iron Containing Proteins

Dissertação apresentada para obtenção do Grau de Doutor em Bioquímica, ramo de Bioquímica-Física, pela Universidade Nova de Lisboa, Faculdade de Ciências e Tecnologia

Lisboa
2008

Nº de arquivo
“Copyright”

Agradecimentos

A execução desta tese só foi possível com a colaboração de algumas pessoas.

Assim, em primeiro lugar gostaria de agradecer ao Prof. Pedro Tavares, meu orientador, não só por me ter recebido aquando do meu estágio de licenciatura mas principalmente por me ter guiado ao longo da realização deste trabalho. Muito obrigado pela dedicação. Muito obrigado por tudo!

Seguidamente gostaria de agradecer à Prof. Alice Pereira, não só pela enorme ajuda científica, mas principalmente pela amizade, disponibilidade e por todos os bons conselhos.

Aos Profs. José Moura e Isabel Moura agradeço o facto de me terem recebido nos seus laboratórios e facultado a utilização dos seus equipamentos, bem como pela amizade demonstrada.

Aos meus colegas Américo, Márcia e Cristina Timóteo gostaria de agradecer não só pela amizade e companheirismo demonstrado mas sobretudo pela ajuda importante para a realização do segundo capitulo desta tese.

Gostaria também de agradecer ao Prof. Boi Hanh (Vincent) Huynh, ao Doutor Sunil Naik e ao Doutor Danilo Ortillo pela forma de como fui recebido no Departamento de Física da Universidade de Emory e pela ajuda não só na obtenção de alguns dos dados desta tese como da discussão cientifica.

À Joana Santos gostaria de agradecer não só a ajuda (fantástica!) no plano cientifico mas sobretudo pela boa disposição e pelos momentos de “gargalhada” no laboratório.

Não posso também deixar de agradecer ao Rui Almeida pela amizade, companheirismo, disponibilidade e ajuda sempre prestada ao longo destes anos, em especial na revisão desta tese.

Aos meus colegas de laboratório Andrea, Carlos, Cristina Cordas, Cristiano, Simone, Susana, Tiago e Rui Duarte, bem como a todos os outros que cá continuam e aos que já foram embora (Anders e Patrícia Raleiras), gostaria de agradecer a vossa ajuda, amizade e disponibilidade em alguns momentos ao longo destes anos.

Aos outros colegas “doutorandos” do DQ, António Nunes, Diogo Latino, Inês Gomes e Vítor Rosa gostaria de agradecer os grandes momentos de boa disposição e companheirismo.

Ao grande amigo Bruno Pedras gostaria de agradecer os todos os bons momentos passados ao longo destes anos e em especial por me fazer sempre lembrar que há outras coisas na vida para além da ciência!

À Margarida queria agradecer por, de uma forma ou de outra, ter estado sempre comigo quer nos momentos bons quer nos menos bons. Muito obrigado por estares “aqui”...

Aos todos os outros meus amigos, especialmente ao David, Inês, Marta, Miguel, Pedro, Ricardo, gostaria de agradecer o facto de terem estado sempre presentes, mesmo quando eu não podia estar! Prometo que um dia vos vou recompensar!

Aos meus pais e a toda a minha família (aos que estão e ao que já não podem assistir...) tenho de agradecer por todo o apoio demonstrado desde sempre, nunca dizendo que não a nada. Assim é bem mais fácil andar para a frente.

À Fundação para a Ciência e Tecnologia pelo financiamento (SFRH/BD/18905/2004) sem o qual a execução deste trabalho não seria possível.

FCT
Fundação para a Ciência e a Tecnologia
MINISTÉRIO DA CIÊNCIA, TECNOLOGIA E ENSINO SUPERIOR

Resumo

Ao longo das últimas décadas tem-se assistido a um grande desenvolvimento no campo da bioquímica estrutural e funcional tendo por base o estudo de proteínas, especificamente enzimas, que possuem na sua constituição centros metálicos.

Nesta tese são abordadas diferentes proteínas com diferentes tipos de centros de ferro não-hémico. A relação destas quer com o oxigénio molecular quer com espécies reactivas de oxigénio encontra-se também em estudo.

Na realização deste trabalho foram utilizadas diversas técnicas de cinética rápida, acopladas a técnicas espectroscópicas como a Ressonância Paramagnética Electrónica (RPE), Espectroscopia de Mössbauer e UV-Visível.

Incorporação de ferro pela ferritina de *Desulfovibrio vulgaris* Hildenborough

As ferritinas são proteínas globulares compostas por 24 subunidades e que podem comportar no seu interior até 4500 átomos de ferro provenientes da sua actividade ferroxidática.

Este tipo de proteínas pode ser encontrado em praticamente todos os organismos e tem quase sempre como substrato, para além do ferro, o oxigénio molecular.

O objectivo deste trabalho visa a caracterização não só cinética mas também espectroscópica (espectroscopias de RPE e Mössbauer) da incorporação de ferro pela ferritina de *Desulfovibrio vulgaris* Hildenborough.

A elaboração destes estudos também com uma proteína contendo um aminoácido mutado, E130A, ajudou a compreender a importância de um terceiro sítio de ligação ao ferro (presente nesta proteína) para a formação de algumas espécies intermediárias, como um radical tirosil e uma espécie de valência mista, não identificadas noutras ferritinas.

A redução do radical anião superóxido pelo redutase do superóxido

Os redutases do superóxido são enzimas não-hémicos, de pequena massa molecular, com centros metálicos de ferro coordenados por enxofre, normalmente associado à protecção contra o *stress* oxidativo.

Foi estudado o processo de transferência electrónica entre três diferentes formas deste enzima e o seu doador electrónico. Um estudo da transferência electrónica mediada pelo consumo de superóxido foi também realizado. O conjunto destes dados permitiu compreender a relevância de um dos centros desta proteína para a sua actividade.

Finalmente, foi efectuada uma caracterização por espectroscopia de Mössbauer de uma SOR, pertencente à classe II.

Estudo da incorporação de metais numa forma Apo da rubredoxina de *Desulfovibrio gigas*

A caracterização, bem como o estudo de metaloproteínas, envolve maioritariamente a utilização de técnicas espectroscópicas (espectroscopias de RPE, Mössbauer, Ressonância Raman, Fluorescência, entre outras). Contudo, a complexidade das proteínas e dos seus centros metálicos pode causar algumas dificuldades quer na escolha da técnica a usar, quer na análise dos dados obtidos.

O estudo de proteínas estruturalmente mais simples ou que possuam características espectroscópicas singulares pode torná-las modelos para proteínas mais complexas.

Neste caso, a proteína em estudo, a rubredoxina de *Desulfovibrio gigas*, foi utilizada não só como modelo para as espectroscopias de UV-Visível e Mössbauer mas também para a incorporação de metais em proteínas.

Com este estudo ficou também claro que a incorporação de um metal numa proteína é um processo que depende de outros factores (estabilidade ou potencial redox) para além da cinética da sua incorporação.

Abstract

Over the last few decades a large effort has been done in the structural biochemistry field. This effort is based on the study of some proteins, namely metalloproteins, that contain cofactors and/or active sites with metal ions in their constitution.

This thesis will focus on different studies performed in metalloproteins that contain non-heme iron centers. An important point is their relation to oxygen and reactive oxygen species.

To perform these studies, fast kinetic techniques were used coupled to spectroscopic techniques, such as Electronic Paramagnetic Resonance (EPR), Mössbauer and UV-Visible.

Metal incorporation by *Desulfovibrio vulgaris* Hildenborough ferritin

Ferritins are globular proteins composed by 24 subunits that are able to store about 4500 iron atoms in an inner central cavity. These iron atoms are rescued from solution and concomitantly oxidized from the ferrous to the ferric state using molecular oxygen as co-substrate. Such activity is, for fast ferritins, called ferroxidase activity.

These proteins are found in most organisms (including bacteria, plants and animals) and serve the dual purpose of regulating iron concentration and detoxification.

The metal incorporation process performed by *Desulfovibrio vulgaris* Hildenborough ferritin was studied by fast kinetic techniques coupled to spectroscopies like EPR and Mössbauer.

The use of a mutant protein, E130A, to perform the same studies brought new insights about the relevance of a third metal binding site to the formation of intermediate species like tyrosyl radical and mixed-valence species, that were not identified in other ferritins.

Superoxide reduction by superoxide reductase

Superoxide reductases (SOR) are small proteins with non-heme iron centers coordinated by sulfur, oxygen and nitrogen atoms. These proteins are usually associated with oxidative stress regulation.

Three different forms of a class I SOR were studied. The studies performed aimed the characterization of both direct and superoxide mediated electron transfer between SOR and it physiological donor, rubredoxin.

The results obtained were helpful in order to understand the relevance of center I of class I SOR to the enzyme’s activity.

Another study based on Mössbauer spectroscopy was also performed in a class II SOR.

Metal incorporation in an Apoprotein form of *Desulfovibrio gigas* rubredoxin

As mentioned before, the characterization of metalloproteins is directly connected to the use of spectroscopic techniques like EPR, Mössbauer, Resonance Raman, Fluorescence and others). However, some proteins have a complex assortment of several metallic centers making difficult a complete spectral analysis.

The use of smaller, less complex proteins and enzymes that contain in their structure features that simplify the spectroscopic analysis can be very helpful since they can be used as model to more complex systems.

In this thesis, a small electron transfer protein, rubredoxin from *Desulfovibrio gigas*, was used not only as a model for techniques like Mössbauer spectroscopy and UV-Visible, but also to study metal incorporation processes in this type of proteins.

These studies also pointed out that the metal incorporation process inside of a living cell should not depend only on the kinetics but also in other factors like stability or redox potential.

Symbols and Abbreviations

Symbols

ΔE_Q	Quadrupole Splitting
δ	Isomer shift
Γ	Mössbauer spectrum linewidth
v	Reaction rate
k	Kinetic rate constant
k'	Apparent kinetic rate constant
V	Volt

Abbreviations

a.a	Amino acid
Apo	Apoprotein
BSA	Bovine Serum Albumin
CcO	Cytochrome *c* Oxidase (EC 1.9.3.1)
CcP	Cytochrome *c* Peroxidase (EC 1.11.1.5)
CCR	Closed-Cycle Refrigerator
D.	*Desulfovibrio*
DEAE	Diethylaminoethylethane
Dfx	Desulfoferredoxin
Dg	*Desulfovibrio gigas*
DNA	Deoxyribonucleic acid
Dps	DNA protection during starvation
Dv	*Desulfovibrio vulgaris* Hildenborough
DTT	Dithiothreitol
EDTA	Ethylenediaminetetraacetic acid
EPR	Electron Paramagnetic Resonance
E. coli	*Escherichia coli*
FAD	Flavin Adenine Dinucleotide

Ftn	Ferritin
FtnA	Ferritin A from *E. coli*
HPLC	High Performance Liquid Chromatography,
LB	Luria-Bertani broth or medium
M.	Methanobacterium
MES	4-Morpholineethanesulfonic acid
MMO	Methane Monooxygenase (EC 1.14.13.25)
NADH	Nicotinamide Adenine Dinucleotide
Nlr	Neelaredoxin (EC 1.15.1.2)
NOS	Nitric Oxide Synthase (EC 1.14.13.39)
O.D.	Optical Density
PDB	Protein Data Bank
RFQ	Rapid Freeze-Quench
Rd	Rubredoxin
RNR-R2	Ribonucleotide Reductase R2 (EC 1.17.4.1)
RO	Rieske Oxygenase (EC 1.14.12.18)
SDS-PAGE	Sodium Dodecyl Sulfate Polyacrylamide Gel Electrophoresis
SF	Stopped-Flow
SOD	Superoxide dismutase (EC 1.15.1.1)
SOR	Superoxide reductases (EC 1.15.1.2)
TCA	Trichloroacetic Acid
TPTZ	Tripyridyl-s-triazine
Tris-HCl	Tris(hydroxymethyl)aminomethane
Tyr	Tyrosine
UV-Vis	UV-Visible
wt	Wild type

Index

Chapter I

General Introduction

Chapter II

Structural and mechanistic features of Ferritin from *Desulfovibrio vulgaris* Hildenborough

Chapter III

Structural and mechanistic features of SORs from *Desulfovibrio vulgaris* Hildenborough and *Desulfovibrio gigas*

Chapter IV

Structural and mechanistic studies of metal incorporation in rubredoxin from *Desulfovibrio gigas*

Appendix A

Methods

Appendix B

Equipment

Figures Index

Chapter I

General Introduction

Chapter II

Structural and mechanistic features of Ferritin from *Desulfovibrio vulgaris* Hildenborough

Chapter III

Structural and mechanistic features of SORs from *Desulfovibrio vulgaris* Hildenborough and *Desulfovibrio gigas*

Chapter IV

Structural and mechanistic studies of metal incorporation in rubredoxin from *Desulfovibrio gigas*

Appendix A

Methods

Appendix B

Equipment

Tables Index

Chapter II

Structural and mechanistic features of Ferritin from *Desulfovibrio vulgaris* Hildenborough

Chapter III

Structural and mechanistic features of SORs from *Desulfovibrio vulgaris* Hildenborough and *Desulfovibrio gigas*

Chapter IV

Structural and mechanistic studies of metal incorporation in rubredoxin from *Desulfovibrio gigas*

Appendix A

Methods

General Introduction

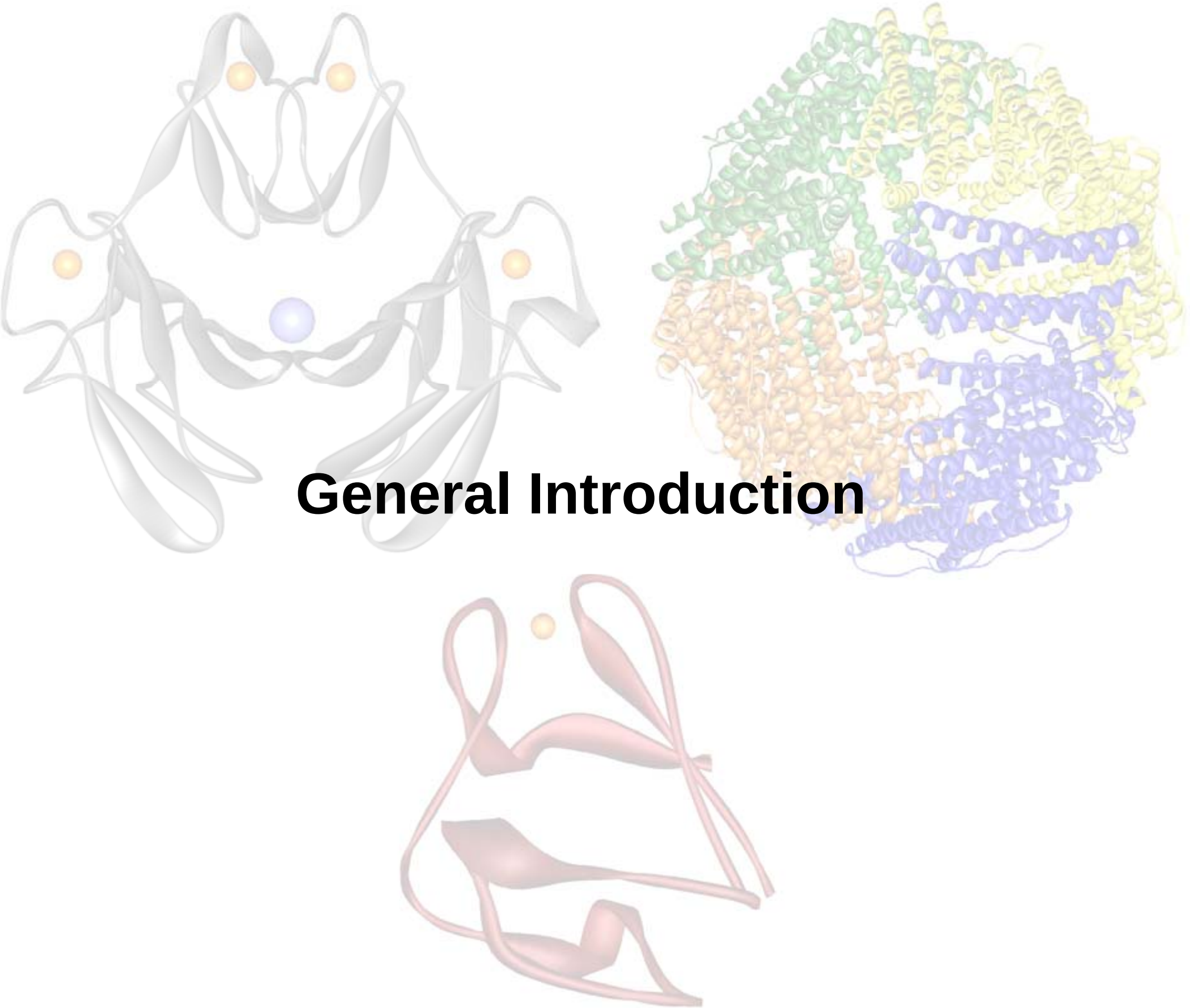

Index

Chapter I

Introduction

I. – Introduction

Life, as we know it, is supported by several chemical elements. Two of them, iron and oxygen, are essential for all organisms. Despite that, iron and oxygen metabolisms are yet to be fully understood. This thesis aims to gather further understanding of iron and oxygen interplay in biology and reveal details related to iron and oxygen toxicity.

The first chapter of this thesis provides a brief description of several concepts important for the understanding of the presented work.

I.1 – Biological Mechanisms of Oxygen Activation

Oxygen was discovered in 1774 by the British chemist Joseph Priestley and, independently, by the Swedish pharmacist Carl Wilhelm Scheele. Scheele had produced oxygen gas by heating mercuric oxide and various nitrates. He called the gas “fire air” because it was the only known supporter of combustion[1, 2].

About the same time, the French chemist Antoine Laurent Lavoisier claimed the discovery of the new substance. However, Priestley visited Lavoisier in October 1774 and told him about his experiment and how he liberated the new gas. Scheele also posted a letter to Lavoisier on September 30, 1774 that described his own discovery of the previously-unknown substance, but Lavoisier never acknowledged receiving it (a copy of the letter was found in Scheele's belongings after his death)[2].

What Lavoisier undoubtedly did was to conduct the first adequate quantitative experiments on oxidation and give the first correct explanation of how combustion works.

Since then, several techniques of molecular oxygen production have been developed making possible its use in many different purposes, like science, space industry and heavy industry, among others.

Molecular oxygen also plays a key role in Nature as a powerful oxidant, reducing itself into species such as water or hydrogen peroxide. Although the oxidation of almost all biological molecules is a thermodynamically favorable process, it doesn't occur spontaneously. This is due to the fact that, in its ground state, O_2 is a triplet while most of reactants are singlets leading to spin forbidden processes. Thus, reactions between molecular oxygen and other molecules should be kinetically unfavorable, requiring a large activation energy[3, 4]. Over the years, Nature overcame this problem by using transition metals for pairing electrons. This process is called "oxygen activation".

This complementarity enables oxygen to participate in biological cycles but can lead also to the formation of reactive oxygen species (ROS). This behavior requires a large protection mechanism in order to overcome the possible lethal effects of the reactive species formed.

Thus, if we look inside a cell we will see a complementary system that involves groups of enzymes that use O_2 for catalysis and another group that eliminates the excess of hazardous metabolites formed.

In this subject several enzymes will be described. Since the main goal is to give introductory remarks on mechanisms of oxygen activation and ROS detoxification, only bacterial ferritin and superoxide reductases (SOR) will be described with detail. The description of all the other mentioned proteins will serve only as an overview/review of oxygen activation and as a guide to understand both ferritin and SOR unanswered questions, and will be based only in recently published reviews.

I.1.1 – Heme monooxygenases

Peroxidases

Despite peroxidases not being monooxygenases, it is important to refer them since much of the terminology used to define monooxygenase complexes derives from the ones established for these enzymes.

Peroxidases were the first enzymes in which high-valent iron intermediates were detected[5, 6]. These enzymes promote peroxides heterolysis, mainly hydrogen peroxide, in order to obtain a potent oxidizing agent used to react with the substrate.

Heterolysis is a two electron process where an oxidized intermediate is formed, **compound I**, which is a ferryl heme complex (Fe^{4+}=O)[3, 6]. Depending on the organism, the second oxidizing equivalent can be stored either on the porphyrin ring as a porphyrin π–cation radical or on a tryptophan residue[6].

On the other hand, there are other peroxidases such as cytochrome *c* peroxidases (CcP) (EC 1.11.1.5), isolated from organisms like *Pseudomonas stutzeri*, that are able to reduce hydrogen peroxide to water. Formation of high-valent species such as a ferryl intermediate (Fe^{4+}=O) also occurs in these type peroxidases[7].

Due to the relatively long half-life of peroxidases intermediate species and their similarities with the ones found in monooxygenases, they are commonly used as model for extrapolation.

Cytochrome *c* Oxidase

Cytochrome *c* Oxidase (CcO) (EC 1.9.3.1) is a membrane bound metalloprotein, involved in the respiratory chains of mitochondria and aerobic bacteria. It catalyzes the $4e^-/4H^+$ reduction of O_2 to H_2O without the formation of ROS as shown in Eq. I.1[8, 9].

$$4CcO^{2+} + 8H_{in}^{+} + O_2 \longrightarrow 4CcO^{3+} + 4H_{out}^{+} + 2H_2O \qquad \text{Eq.I. 1}$$

The other important feature of this enzyme is its ability to translocate protons across the membrane. These protons will be used later for ATP synthase for the endergonic synthesis of ATP[10, 11].

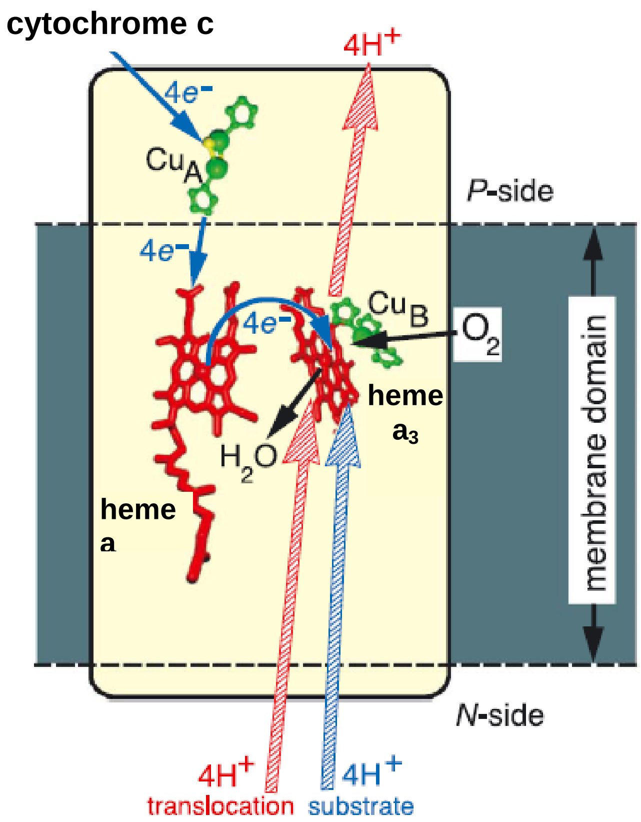

Figure I. 1 – Schematic representation of CcO function. The blue arrows represent the O_2 reduction to water. The red arrows represent the proton translocation coupled to the enzymatic activity. Adapted from [10].

Despite the biological importance of the mechanism of proton translocation, this subject will focus only on the oxygen activation mechanism performed by this enzyme.

CcO has two subunits, one inside of the membrane, where one Cu_B atom, one heme *a* and one heme a_3 (myoglobin-type iron center) is located. The 3D structures demonstrate that the O_2 activation site is formed by the Cu_B and heme a_3 [8, 12].

The characterization of the enzymatic mechanism has been described essentially by Resonance Raman spectroscopy coupled with X-ray data, pointing to a first intermediate formed between O_2 and $Fe_{a_3}^{2+}$, Fe^{2+}-O_2. The Cu^{1+}_B interaction is thought to be weak due to the trigonal planar geometry[13].

The next step involves a conformational change consistent with the formation of a hydrogen bond between a tyrosine (Tyr) residue and the Fe^{2+}-O_2 site, giving rise to a hydroperoxy state Fe^{3+}-O-OH. The covalent bond between the tyrosine and the histidine coordinated to Cu_B provides an effective electron transfer pathway from Cu_B to the OH group of tyrosine[12, 13].

The reaction follows with the appearance of a ferryl intermediate, Fe^{4+}=O_2, formed via two electron reduction. One electron is provided by $Fe_{a_3}^{3+}$, which is converted to $Fe_{a_3}^{4+}$, and the other electron from Tyr-O^- which is converted to a Tyr radical. This third intermediate is finally converted into a ferric Fe^{3+}-OH^- (figure I.2)[8, 12, 13].

In order to clarify and thus provide additional data related with the CcO O_2 activation mechanism, several studies have been performed[8, 14].

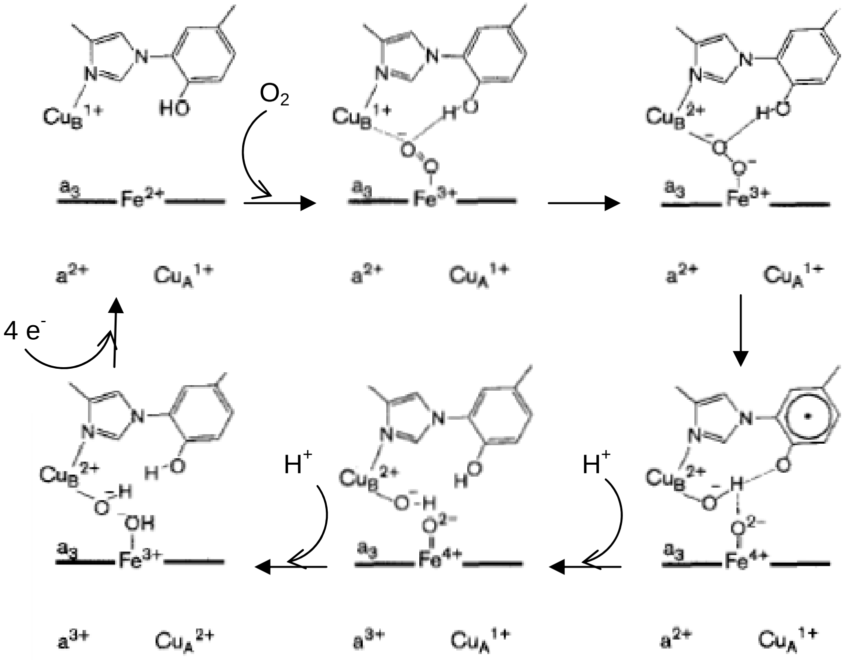

Figure I. 2 – Schematic representation of CcO enzymatic mechanism. Adapted from[12].

Nitric Oxide Synthase

Nitric Oxide Synthase (NOS) (EC 1.14.13.39) is one of the most complex enzymes involved in oxygen activation. This is probably due to the fact that this enzyme is related to the production of a vital molecule in mammals, NO. Depending on the location, the NO produced is not only used as second messenger by activation of soluble guanylyl cyclase in the cardiovascular and nervous systems, but also as a cytotoxic agent in the immune system[15].

NOS produce NO from L-arginine in the presence of O_2 and NADPH. The enzymatic mechanism is very similar to other heme monooxygenases, exception being the presence of another redox cofactor called tetrahydrobiopterin, H_4B, and a regulatory protein, calmodulin (CaM)[12, 15].

The redox cofactor H_4B is thought to have a main function which is related to the high rigidity of NOS structure, which leads to the exposure of the catalytic site to solvent that would cause the formation of $Fe^{3+}OOH^-$. This species, in turn, could be subjected to uncoupling by the solvent, with possible release of H_2O_2. Therefore, a fast and coupled proton-electron transfer system is needed to ensure the formation of Fe^{3+}-OOH_2[16].

Besides the structural complexity of this enzyme compared to other heme monooxygenases, there is an additional issue for the overall mechanism. The final product, NO, is a heme diatomic ligand, like O_2, which leads NOS to feedback inhibition[15].

NOS mechanism presents a resting state Fe^{3+}/H_4B, which is reduced to Fe^{2+}/H_4B to be able to bind O_2. The oxygen binding will set up an equilibrium between the $(Fe^{2+}\text{-}O_2)/H_4B$ and $(Fe^{3+}\text{-}O_2^-)/H_4B$ forms. The iron-oxygen complex is then reduced by H_4B, forming $(Fe^{3+}\text{-}O_2^{2-})/H_4B^+$. It is assumed that the next step involves the consecutive addition of two protons for O-O bond cleavage, giving $(Fe^{3+}\text{-O-O-}H_2)/H_4B$, resulting in a Fe^{3+}-O or its electronic equivalent Fe^{4+}=O state. However, these last intermediates are yet to be trapped and characterized spectroscopicaly. The reaction ends with the formation of the products, NO and citrulline[12, 15, 16].

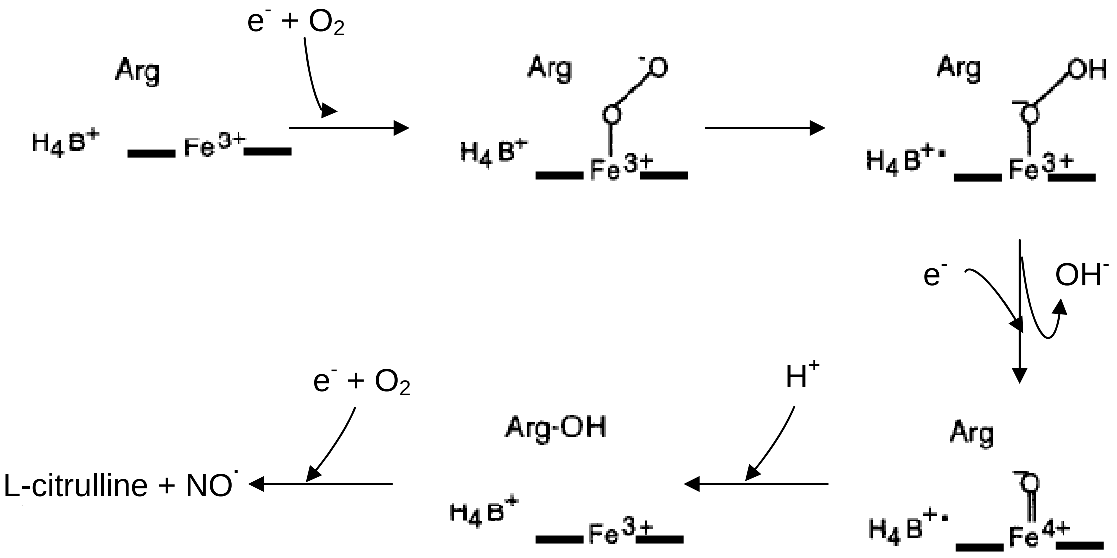

Figure I. 3 - Schematic representation of NOS enzymatic mechanism. Adapted from[12].

P450

Cytochrome P450 is probably the most recognized of all heme monooxygenases. This is probably due to its presence in a large number of organisms from bacteria to humans. P450s are able to catalyze the hydroxylation and epoxidation of a wide range of organic compounds. These enzymes are involved in several metabolisms, like sexual hormones, vitamin D, bile acids, drugs and xenobiotics, among others. They are so important for the overall metabolism that one single organism can contain several dozens of different P450s. For instance a small flowering plant, *Arabidopsis*, has 273 sequences in the genome that codify to P450s (or homologues)[17].

One of the interesting features of this enzyme is its 3D structure. Contrary to NOS, P450 presents structural changes depending on the presence of substrate. These changes can be related to the control of enzyme activity. Like in NOS, it is important to prevent the exposure to solvent and the consequent Fe^{3+}-OOH^- uncoupling, with formation of hydrogen peroxide[16].

From the catalytic point of view P450, is not so different from other heme monooxygenases like NOS. The catalytic cycle begins with a low-spin Fe^{3+} heme, coordinated to a water molecule. This water molecule will be displaced by the substrate turning it into a high-spin Fe^{3+} heme. The following step comprises a one electron reduction coupled to the oxygenation process, forming the oxy intermediate Fe^{3+}-O_2^-. A second electron will generate the peroxy species Fe^{3+}-O_2^{2-}. The capture of two protons will drive the O-O cleavage via hydroperoxy (Fe^{3+}-O-O-H^-) and dihydroperoxy (Fe^{3+}-O-O-H_2) leading to the formation of the ferryl intermediate (Fe^{4+}=O) the so called **compound I** (named due to the similarity to peroxidases' reaction intermediates)[3, 16-18].

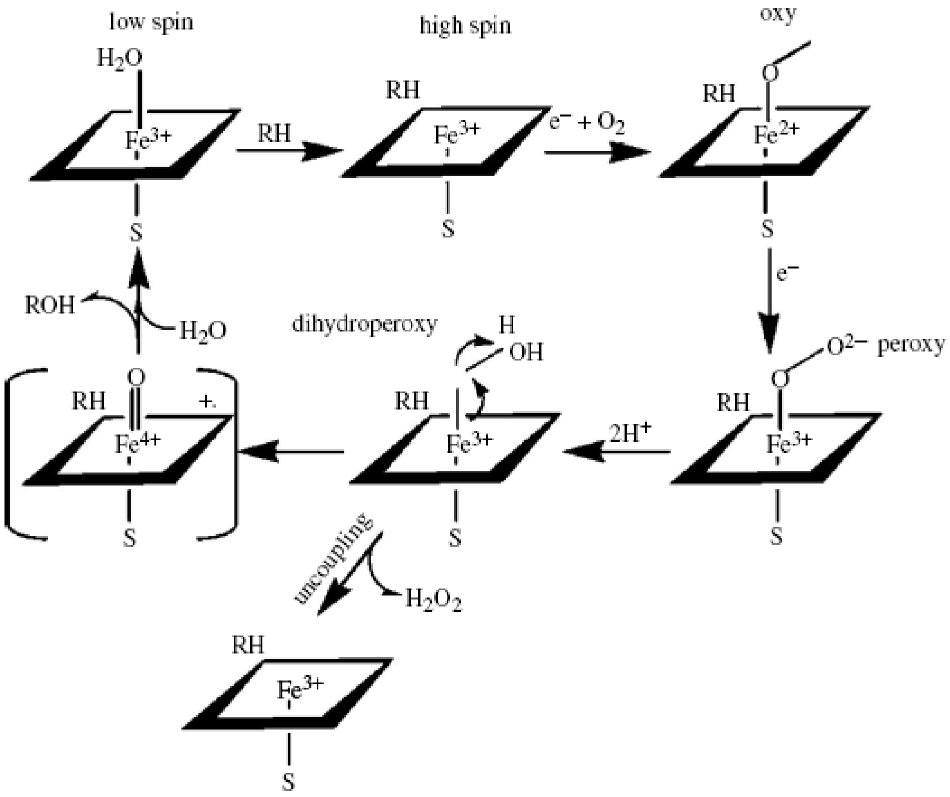

Figure I. 4 – Schematic representation of cytochrome P450 catalytic cycle. Adapted from [17].

For the past few years, the scientific community has performed several studies in order to isolate and characterize the catalytic intermediates. However, contrary to the results obtained for peroxidases, only the first intermediates could be trapped. This may mean that some steps, such as the addition of the second proton, occur too fast (little stability of the formed species), in the experimental timescale, and can only be assumed by comparison to similar mechanisms like peroxidases or based on density functional theory (DFT) calculations[16, 17].

From the examples given it is possible to conclude that oxygen activation processes will, in principle, undergo several intermediates like, **oxy**, **peroxy**, **hydroperoxy**, **dihydroperoxy** and **ferryl**.

Most of the studies performed, concern the understanding of electron pathways and proton delivery. These are the main steps for the heterolytic cleavage of O-O bond and subsequent formation of the ferryl species (active), which consists of an O atom with six valence electrons, a strong oxidant. Another important aspect is the uncoupling reaction, which can be promoted by the inappropriate protonation of the hydroperoxy species, leading to H_2O_2 release.

Structural changes are also important for catalysis since they are strongly related to the regulation of the enzymatic activity. In NOS, for example, it is important to ensure that the product, NO, is released while in P450 these changes ensure that the catalysis follows the correct pathway without uncoupling.

I.1.2 – Non-Heme monooxygenases

Like heme monooxygenases, non-heme monooxygenases are also involved in a variety of reactions that use molecular oxygen to metabolize a wide range of compounds. However, the fact that they have a binuclear iron center as cofactor instead of an heme group, make them a unique case study in terms of both spectroscopic and biochemical characterization.

Methane Monooxygenases

Soluble Methane Monooxygenases (sMMO) (EC 1.14.13.25) belong to a large group of bacterial oxygenases that are responsible for the oxidation of the highly stable methane molecule to methanol in a NADH-dependent reaction[19].

Like other non-heme oxygenases, sMMOs have been described as a multicomponent class of enzymes. Structural analysis shows that sMMO has 3 components, a hydroxylase subunit (MMOH), a reductase subunit (MMOR) and a regulatory protein subunit (MMOB)[19, 20].

The active site is composed of a carboxylate-bridge diiron center located at the MMOH component. The MMOR subunit transfers electrons from NADH through its FAD and [2Fe-2S] cofactors to the active site. MMOB is a small α/β protein related to putidaredoxin both in structure and genetics. Despite its function not being yet well understood, some studies point to its role in electron transfer and in substrate binding during catalysis[19, 20].

The fine interaction between these three components is fundamental for proper catalysis. Like in heme monooxygenases, it is important to ensure that the cycle undergoes the correct pathway to prevent incorrect reduction of the oxygenated species, which would lead to the formation of ROS. This control is provided by the competition between MMOB and MMOR for binding the MMOH. Recent studies reveal that the electron transfer is dependent of the ratio on MMOB and MMOR, since it may be related to a structural change in MMOH, thus modifying the electron transfer rates[21].

The catalytic cycle begins with a two-electron reduction of the diferric center with generation of the reactive all ferrous state. The existent oxo/hydroxo bridges are lost, presumably, by protonation upon reduction. The ferrous diiron species reacts rapidly with molecular oxygen to form a peroxodiferric (Fe^{3+}-O-O-Fe^{3+}). This first intermediate decays into a higher-valent species Q ($Fe^{4+}(\mu\text{-}O_2)Fe^{4+}$), similar to X species in ribonucleotide reductase R2 (RNR-R2). Both peroxodiferric and Q species are reactive with substrates, in a manner similar to the one observed in cytochrome P450[21, 22].

Studies with several substrates were performed in order to compare the reactivity of both intermediates. The results showed that the difference between these two species was related to the type of substrate used, since they have different ways to metabolize substrates. The peroxodiferric species reacts preferentially by two-electron or hydride abstraction, whereas the Q species follows one-electron oxidation[20, 21]. In order to understand the biochemical and spectroscopic characteristics of these systems, several synthetic compounds were used[20, 23].

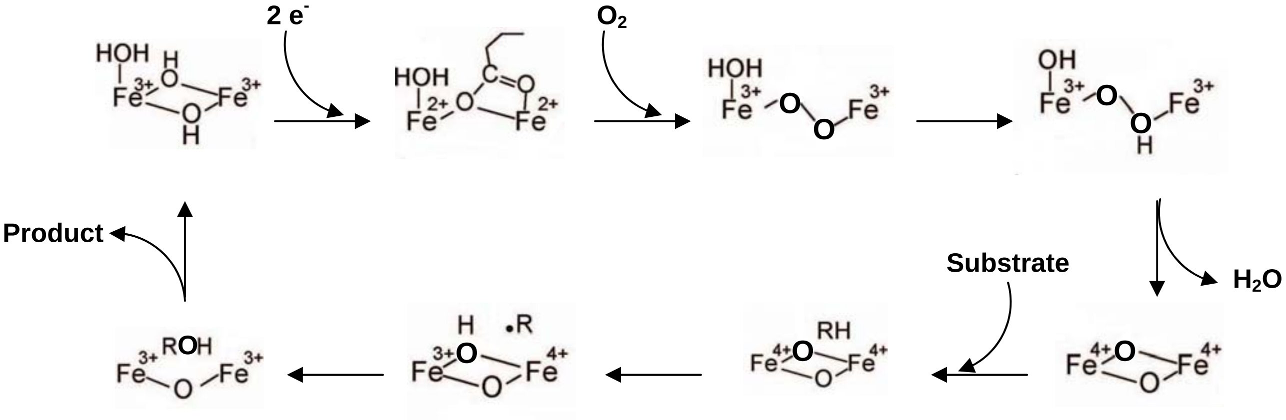

Figure I. 5 – Schematic representation of sMMO catalytic cycle. Adapted from [6, 24, 25].

Rieske Oxygenases

Rieske Oxygenases (RO) (EC 1.14.12.18) are part of the same group of bacterial oxygenases as sMMO, and are responsible for the generation of *cis*-dihydroxylated metabolites, the first step in bacterial degradation of many aromatic compounds[26].

Like sMMOs, the ROs are multicomponent enzymes, formed usually by three components that use molecular oxygen for catalysis. They are similar to the ones found in sMMO, an oxygenase component, a reductase component and a ferredoxin component. The difference is the existence of a Rieske cluster located in the oxygenase component which is responsible for the main differences between the catalytic cycle of sMMO and RO. These are related with the electron transfer between the reductase and hydroxylase components[24, 26, 27].

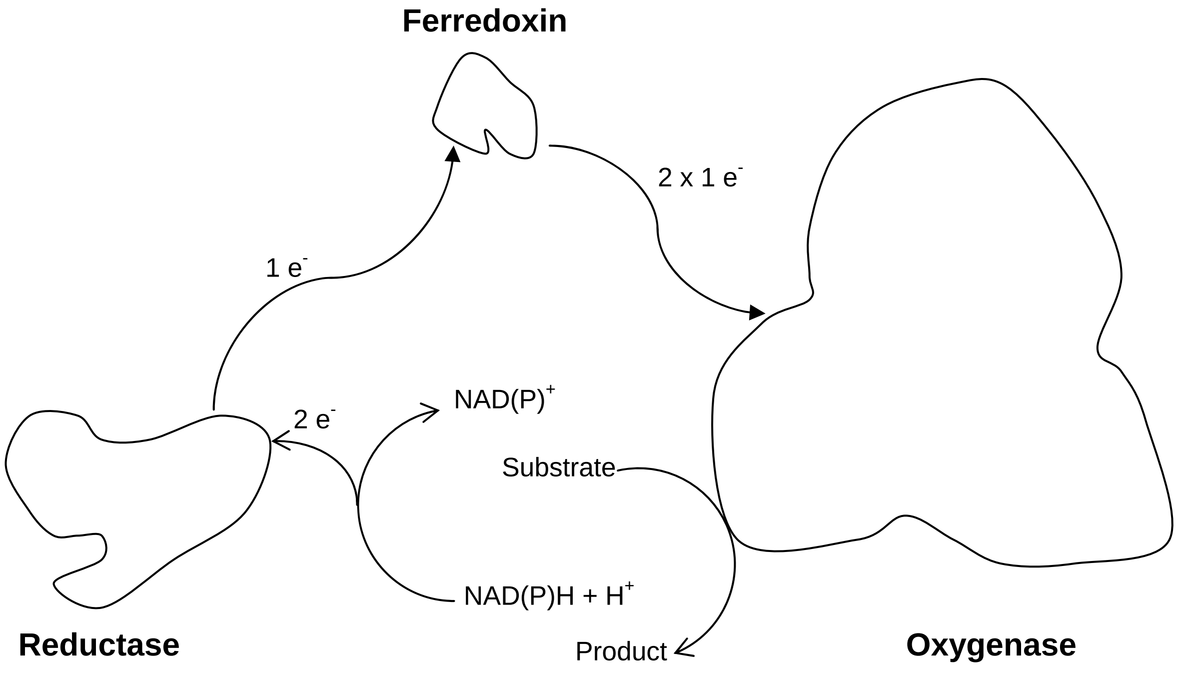

Figure I. 6 – Schematic representation of the three components of a Rieske Oxygenase system. Adapted from [26].

I.1.3 – Bacterial Ferritins

In the beginning of this chapter, the relationship between iron and oxygen was mentioned and some examples of enzymes that use molecular oxygen to perform their catalysis have been described.

In the examples mentioned above, iron was part of the catalytic site of the protein. There is, however, a class of enzymes that uses iron not only to build the catalytic site but also as one of the substrates for catalysis (the other being molecular oxygen). These enzymes are called ferritins.

Ferritins are large spherical protein cages (10-12 nm) that, depending on the type, can have 24 (maxi-ferritin) or 12 (mini-ferritin) subunits. Each subunit has about 20 kDa and is composed by four-helixes bundles with a fifth short helix in the C-terminal region. Depending on the organism (and sometimes the organ), ferritin can be either a homo or heteropolymer. In mammals for example, ferritin can appear with different proportions of H-chain and L-chain while in bacteria it will appear mostly as a homopolymer of H-chain homologue[28, 29]. The difference between these two chains is related to the presence of conserved binuclear iron site, known as ferroxidase center, responsible for the catalysis in the H-chain[30].

Ferritins are present in almost all living organisms, from humans to anaerobic bacteria. The absence of these proteins is incompatible with life in animals and very harmful for bacteria (increasing their oxygen sensitivity)[31-35]. This ability to protect the organism is related to ferritin’s catalytic mechanism.

Ferritins can use either molecular oxygen (for the majority of maxi-ferritins) or hydrogen peroxide (for the majority of mini-ferritins) as a co-substrate for iron storage. Iron storage capacity is particularly important if we consider that only Fe^{2+} is moderately soluble (10^{-4} M) in aqueous solutions at pH 7, while Fe^{3+} is extremely insoluble (10^{-18} M)[36, 37]. As such, ferritin becomes fundamental for cells both as an iron homeostasis “regulator” (chelating the iron and releasing it only when needed) and as an oxygen/hydrogen peroxide “removal tool”[36-40]. In addition to these functions, ferritins are also related to DNA protection in cells. The so called DNA protection during starvation proteins, Dps, are mini-ferritins that bind DNA and protect it against several types of stress situations[37].

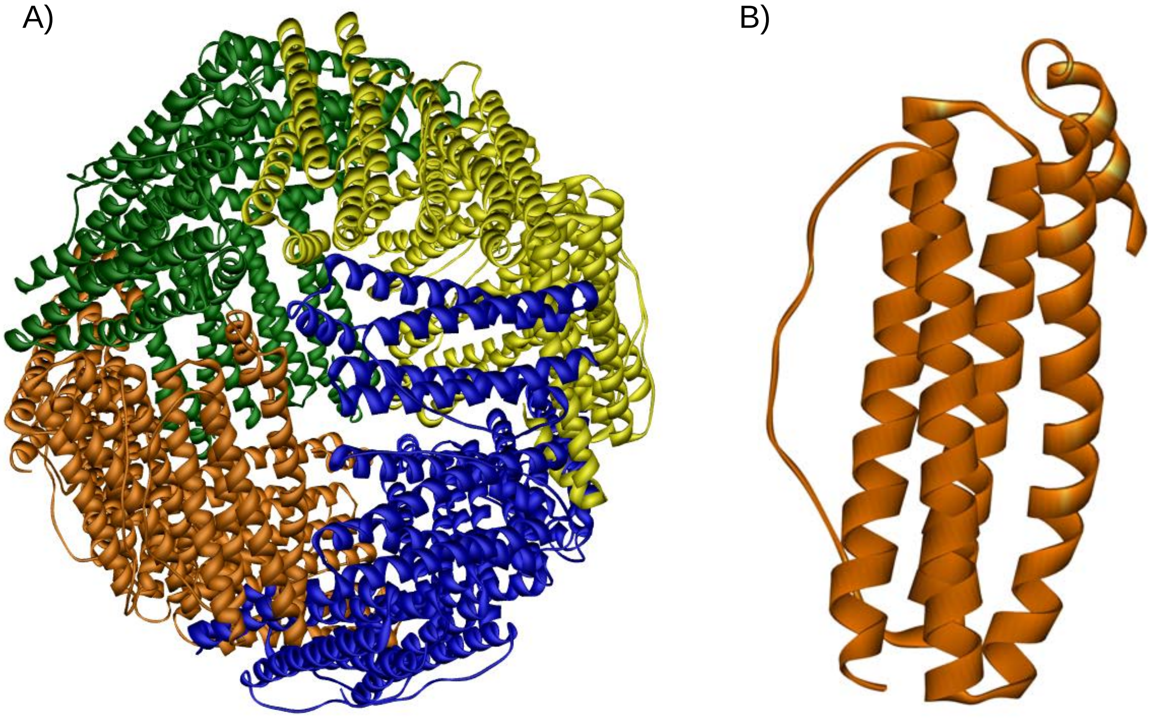

Figure I. 7 - A) 3D Structure of 24-mer FtnA from *Escherichia coli* (PDB Id. 1EUM). 2.05 Å resolution (Stillman, T.J., [41]). B) Subunit of the FtnA from *Escherichia coli*.

From the mechanistic point of view, bacterial ferritins are similar to the previously described proteins involved in oxygen activation, presenting catalytic intermediates with comparable spectroscopic behaviour.

According to the published reports, iron oxidation proceeds via the formation of an μ-1,2-peroxodiferric intermediate, with a characteristic blue colour (with maximum absorption near 600 nm)[42-44]. This species will decay to a more stable μ-1,2-oxodiferric species with the concomitant release of hydrogen peroxide. The amount of hydrogen peroxide produced is not always stoichiometric in relation to the amount of oxo intermediate produced[45, 46]. Mössbauer studies revealed that this μ-1,2-oxodiferric species will decay spontaneously to a μ-1,2-hydroxo-bridged dimer[47]. The formation of the mineral core would be the last step.

Like in some monooxygenases such as RNR-R2, in ferritin it was also reported the formation of a tyrosyl radical during the ferroxidatic process[48-55].

Regarding the stoichiometry, these reactions show in general a 2:1 ratio between the iron and oxygen where two electrons from the iron oxidation will reduce the oxygen to hydrogen peroxide[56, 57]. However, the presence of a third site (site C) in some bacterial ferritins, like FtnA from *E. coli*, introduced some complexity to the mechanism, and so, in this cases a 3-4:1 iron-oxygen ratio is observed[58]. The possibility of a 4:1 stoichiometry instead of 3:1 that would be expected in this particular case can be related to the presence of a fourth iron binding site or an active amino acid residue. In this case, the oxygen would be reduced to water rather than to hydrogen peroxide.

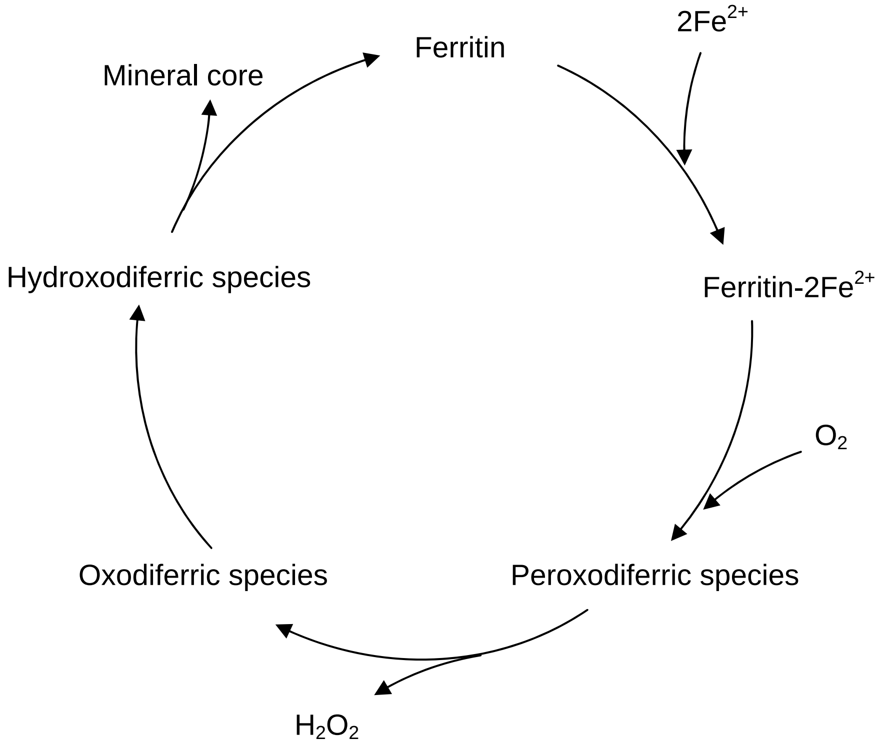

Figure I. 8 - Generic scheme of ferritin catalytic cycle. Adapted from [42-45].

I.2 – Detoxification of Reactive Oxygen Species

As mentioned in the beginning of this chapter, there is a complementarity between the enzymes that use oxygen for catalysis like ferritins and the enzymes that metabolize the ROS formed in the oxygen activation reactions.

ROS can be divided in two groups, radical (superoxide, hydroxyl, peroxyl, alkoxyl and hydroperoxyl) and nonradical (hydrogen peroxide, ozone, singlet oxygen, peroxynitrite and hypochlorous acid). When in excess, these species are usually involved in cellular destruction by different mechanisms like lipid oxidation and DNA and amino acid damage[59-64]. This thesis will focus on the superoxide degradation by SORs.

Superoxide radical can be generated by different sources through a variety of mechanisms. In an aqueous solution, at pH 7.0, superoxide will dismutate into hydrogen peroxide and O_2 with a very high rate constant, about 5 x 10^5 $M^{-1}.s^{-1}$. Thus, once generated, superoxide can be harmful to the cell both directly, and indirectly via the formation of hydrogen peroxide[65, 66].

I.2.1 – Superoxide Reductases

Since the beginning of the 90's several unusual non-heme iron proteins have been isolated and characterized [67-76]. Although the function of these proteins was partially unveiled in 1996 when Touati and coworkers reported that a protein from *Desulfovibrio baarsii* suppressed all the effects caused by the absence of superoxide dismutase (SOD) (EC 1.15.1.1) in *E. coli*, only in 1999 the real function of these proteins was assigned[77-79]. The so called superoxide reductases (SORs) (EC 1.15.1.2) revealed their ability to reduce the superoxide anion to hydrogen peroxide instead of the common dismutation, performed by the well know SOD[71, 74, 77, 80].

$$O_2^- + 2H^+ + e^- \longrightarrow H_2O_2 \text{ (SOR)} \qquad \text{Eq.I.2}$$

$$2O_2^- + 2H^+ \longrightarrow O_2 + H_2O_2 \text{ (SOD)} \qquad \text{Eq.I.3}$$

This ability has an enormous biological relevance if we consider that the major part of these SOR proteins were first purified from anaerobes, thus enabling them to survive when exposed to small amounts of oxygen[81].

SORs are usually divided in three classes according to both the number of iron centers (1Fe-SOR and 2Fe-SOR) and the presence in their primary structure of an N-terminal domain[82].

Class I SORs, historically called desulfoferrodoxins, were first isolated by Moura and coworkers and are characterized by the presence of two iron centers. Center I is very similar to the one found in desulforedoxin isolated from *D. gigas* (one iron atom coordinated by four cysteine residues) and center II (one iron atom coordinated by four histidine residues in the equatorial plane and one cysteine in the axial plane) [68, 70, 83, 84]. These class I SORs can attain three different oxidation states: fully-reduced (colorless, with both centers in the ferrous state), half-reduced (“pink” form, due to the oxidized center I and reduced center II) and fully-oxidized (“gray” form, due to the both oxidized center I and II).

In the pink form the protein exhibits spectroscopic features of a high-spin ferric ion ($S=5/2$) with absorption maxima at 495, 368 and 279 nm. The EPR spectrum shows resonances at $g=7.7$, 5.7, 4.1 and 1.8 with $E/D = 0.08$, while the Mössbauer spectroscopy characterization indicates the presence of two high-spin iron centers, one ferric and one ferrous. The gray form shows additional absorption bands at 335 and 635 nm and the EPR spectrum has additional resonances at $g = 4.3$ and 9.6. The Mössbauer spectrum reveals another component characteristic of a high-spin ferric ion with $E/D = 1/3$ [70, 85, 86].

Class II SORs, historically called neelaredoxins (the protein exhibited a blue color when in the oxidized state and “neela” means “blue” in Sanskrit), were first isolated by Chen and coworkers and are characterized by the presence of one iron center, similar to center II of class I SORs[68]. The absorption spectrum shows features at 666 (pH dependent), 325 and 280 nm.

Contrary to class I and II, which were only found in anaerobic or microaerotolerant bacteria, a new class of SOR was isolated from a microaerophilic organism, the syphilis spirochete *Treponema pallidum*[69, 74, 87]. This new class, class III, is spectroscopicaly similar to class II, presenting only one iron center coordinated by four histidine residues in the equatorial plane and one cysteine residue in the axial plane. Gene sequence analysis showed that the gene product should be a 14 kDa protein with two domains, homologous to class I SOR. However, in this protein, three of the four cysteine residues of center I were not present. The crystal structure of this class III SOR shows a homodimeric protein, very similar to the structure obtained for class I SOR despite possessing only iron center[88].

Besides the biochemical and spectroscopic characterization of these enzymes, several studies concerning the characterization of reaction intermediates have been performed in order to obtain an overall reaction mechanism for these enzymes. Therefore, a possible mechanism can be described by having a pentacoordinate ferrous active site which is in a pH-dependent equilibrium with the hexacoordinate resting ferric state.

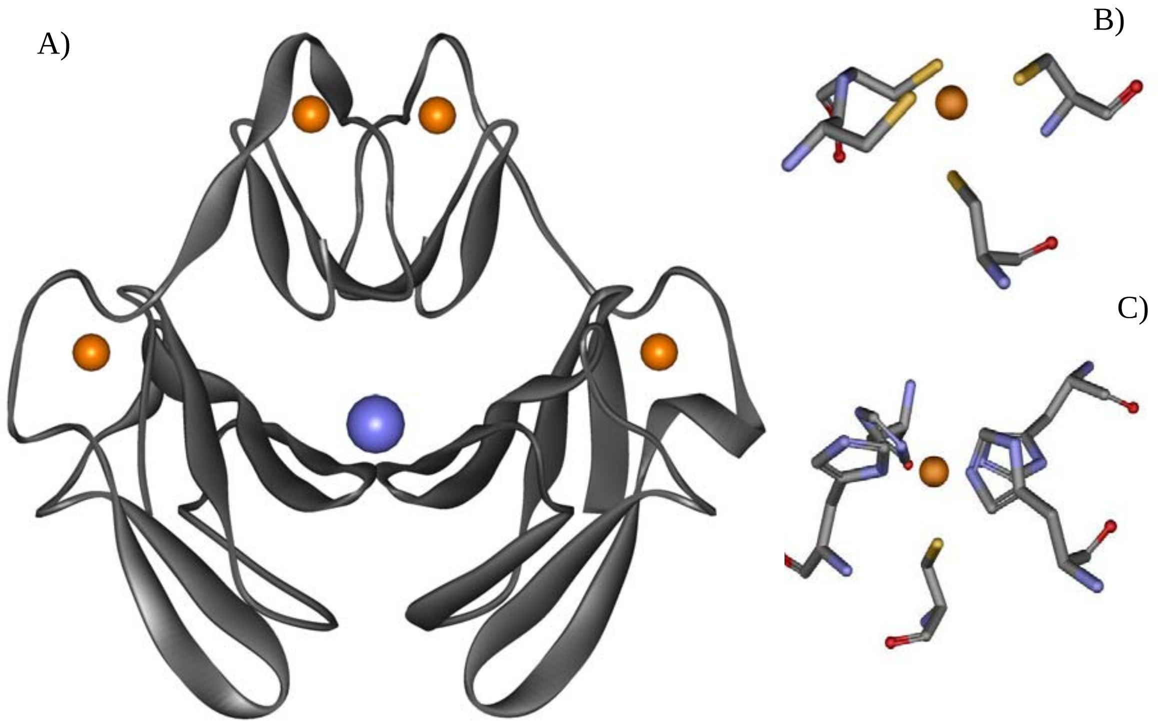

Figure I. 9 – A) 3D Structure of SOR from *Desulfovibrio desulfuricans* ATCC 27774 (PDB Id. 1DFX). 1.9 Å resolution (Coelho *et al.*, [89]). B) Scheme of SOR's center I. C) Scheme of SOR's center II. The dark orange spheres represent the iron atom and the blue sphere represents the calcium atom.

This ferric state can have either a hydroxide or a glutamate as the sixth ligand in a pH dependent equilibrium (high pH values favor the hydroxide binding). After substrate binding to the ferrous site a ferric peroxo species is formed with a rate constant close to 10^9 $M^{-1}.s^{-1}$. The presence of a second intermediate species is currently under discussion, since some authors claim that the direct protonation of the ferric-peroxo species yields the final product, while others suggest the formation of a hydroperoxo species in a process dependent on the proton concentration of the solvent[90-93].

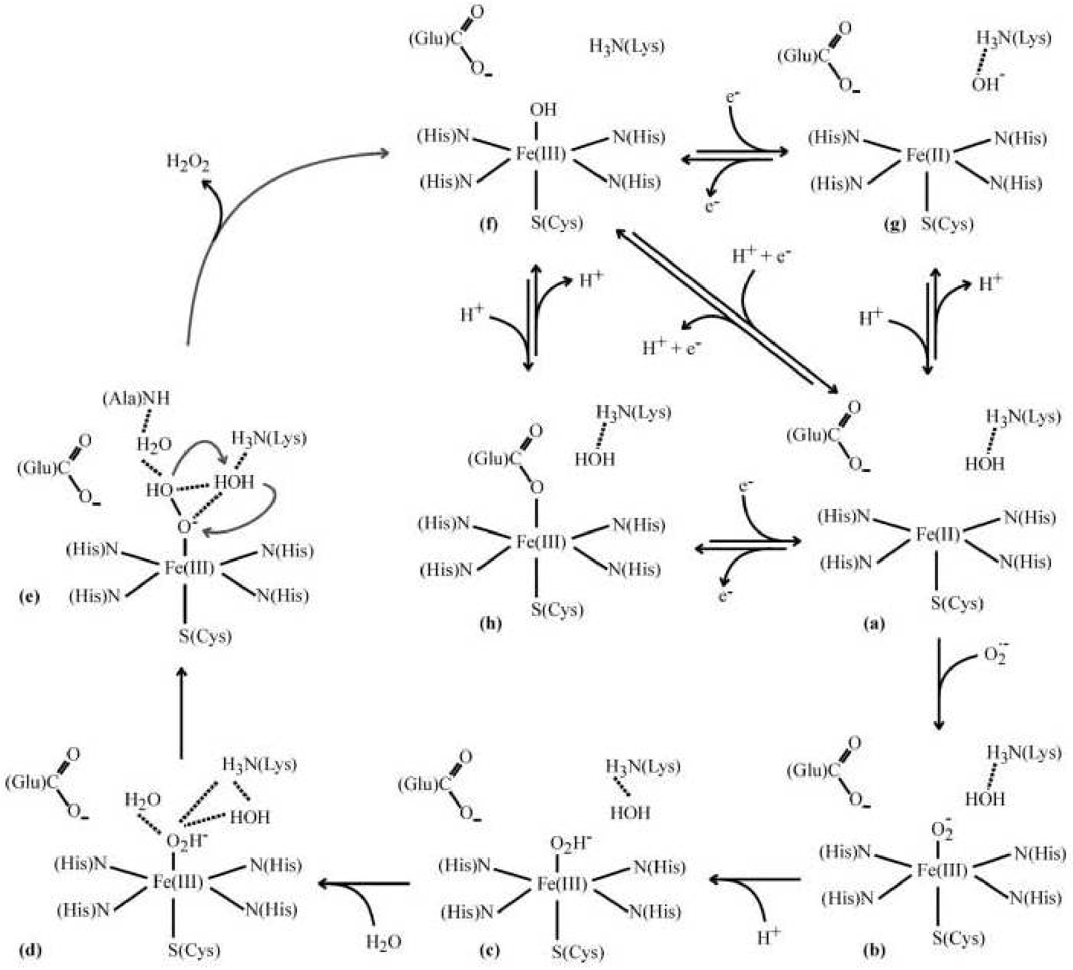

Figure I. 10 – Schematic representation of a proposed catalytic mechanism of SOR considering the following forms: (a) ferrous active state; (b) ferric peroxo intermediate; (c) ferric hydroperoxo intermediate; (d) an extra water molecule is recruited; (e) rearrangement leading to protonation; (f) ferric hydroxyl-bound resting state and (h) ferric carboxylate-bound resting state. Adapted from [82].

The protonation of this second intermediate leads to the formation of the product, hydrogen peroxide.

However, this catalytic process depends not only on protonation but also on electrons that are necessary for superoxide reduction. Until now, two possibilities could be considered: the electron could be transferred directly to the center II to reduce the substrate, or to the center I and then transferred to the center II via intramolecular electron transfer. The reduction via center I could be an important way to prevent the formation of a glutamate-coordinated species[94].

On the other hand, there are evidences that prove that it is possible to reduce superoxide without the involvement of center I, like in the C13S mutant from *D. vulgaris* strain Hildenborough SOR. The resulting protein (lacking center I) revealed catalytic properties similar to the wild type protein[95]. Thus, this result could eliminate the biological relevance of center I. This subject will be studied and discussed later on in this thesis.

I.2.2 – SOR Electron Donor, Rubredoxin

Rubredoxins (Rd) are small (in average, just over 50 amino acids residues), monomeric, non-heme iron proteins with approximately 6 kDa molecular mass[96, 97]. These proteins contain a single iron center, coordinated by four cysteine residues very similar to the center I in the SORs[98-101].

Rds were first isolated from *Clostridium pasteurianum* by Lovenberg and coworkers more than forty years ago. Since then several other rubredoxins have been isolated and characterized both structurally and spectroscopically[96, 101-104]. A large number of X-Ray crystal structures can be found in the Protein Data Bank (PDB).

Rubredoxins are often associated with electron transfer processes in biological systems, working as an electron donor to proteins in many different pathways, like cellular detoxification[96, 105, 106]. Several electron transfer studies between rubredoxin and SORs were recently published[94, 107-109].

In the work presented in this thesis two different recombinant rubredoxins (from *D. vulgaris* Hildenborough and *D. gigas*) will be used. The first will be used as an electron donor to the *D. vulgaris* Hildenborough SOR. These studies will be based on rubredoxin’s ability to reduce SOR[82, 94, 107-109].

A different study, involving *D. gigas* rubredoxin, intends to characterize, kinetic and spectroscopicaly, metal incorporation into an apo form of the protein. The absence of both metallochaperones and inorganic sulfide (or other cofactors) may indicate that rubredoxin doesn’t need specialized machinery to incorporate iron during its expression[97]. This information, combined with the previously published work concerning rubredoxin stability, makes it a perfect probe for understanding, from a biological point of view, the metal incorporation in these type of metallic centers[110, 111].

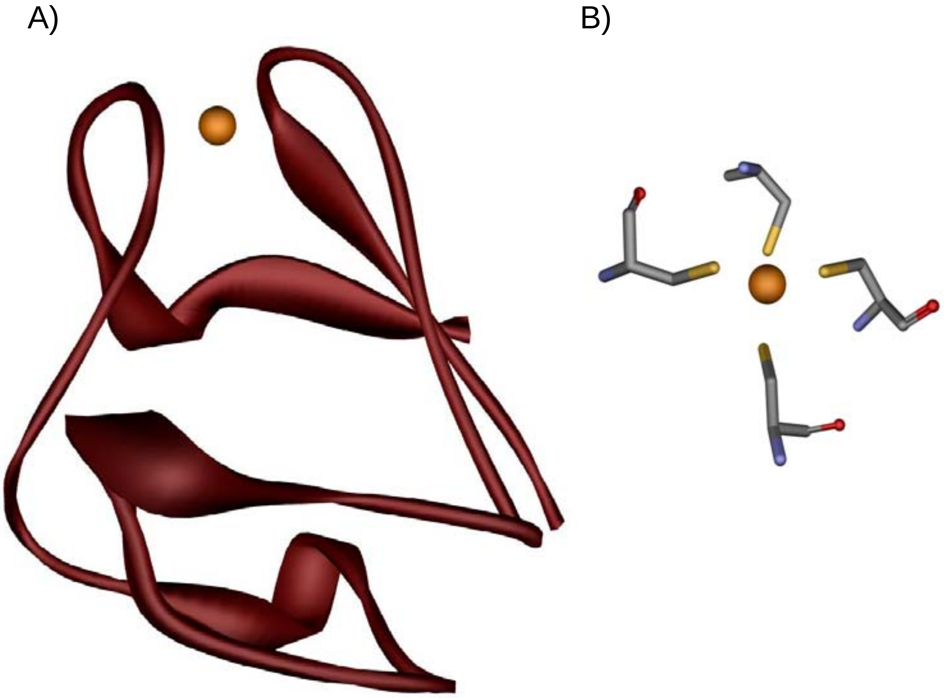

Figure I. 11 – A) 3D Structure of rubredoxin from *Desulfovibrio vulgaris* strain Hildenborough (PDB Id. 1RB9). 0.92 Å resolution. (Dauter Z., *et al.*). B) Schematic representation of rubredoxin’s iron center. Iron atom coordinated by the four cysteine residues. The dark orange spheres represent the iron atom.

Recent studies also point to a flexible structure of apo rubredoxin which folds into the “native” structure upon the incorporation of iron. These studies also show that the metal incorporation follows a number of steps that are dependent from the iron binding to the protein. This incorporation is also dependent on the use of high concentrations of denaturating agents such as urea and guanidine hydrochloride[97].

I.3 – References

[1] L.O. Bram, N.H. Dickey, Funk & Wagnalls New Encyclopedia, Funk & Wagnalls Corporation, New York, 1983.

[2] J. Emsley, "Oxygen", Nature's Building Blocks: An A-Z Guide to the Elements., Oxford University Press, Oxford, 2001.

[3] T.L. Poulos, Structural biology of heme monooxygenases, Biochem Biophys Res Commun 338 (2005) 337-345.

[4] E.F. Elstner, Oxygen Activation and Oxygen-Toxicity, Annual Review of Plant Physiology and Plant Molecular Biology 33 (1982) 73-96.

[5] A.N. Hiner, E.L. Raven, R.N. Thorneley, F. Garcia-Canovas, J.N. Rodriguez-Lopez, Mechanisms of compound I formation in heme peroxidases, J Inorg Biochem 91 (2002) 27-34.

[6] J.M. Bollinger, Jr., C. Krebs, Stalking intermediates in oxygen activation by iron enzymes: motivation and method, J Inorg Biochem 100 (2006) 586-605.

[7] G.W. Pettigrew, A. Echalier, S.R. Pauleta, Structure and mechanism in the bacterial dihaem cytochrome c peroxidases, J Inorg Biochem 100 (2006) 551-567.

[8] Y. Naruta, T. Sasaki, F. Tani, Y. Tachi, N. Kawato, N. Nakamura, Heme-Cu complexes as oxygen-activating functional models for the active site of cytochrome c oxidase, J Inorg Biochem 83 (2001) 239-246.

[9] B. Ludwig, E. Bender, S. Arnold, M. Huttemann, I. Lee, B. Kadenbach, Cytochrome C oxidase and the regulation of oxidative phosphorylation, Chembiochem 2 (2001) 392-403.

[10] M. Wikstrom, Cytochrome c oxidase: 25 years of the elusive proton pump, Biochim Biophys Acta 1655 (2004) 241-247.

[11] M. Wikstrom, M.I. Verkhovsky, Mechanism and energetics of proton translocation by the respiratory heme-copper oxidases, Biochim Biophys Acta 1767 (2007) 1200-1214.

[12] T.L. Poulos, H. Li, C.S. Raman, Heme-mediated oxygen activation in biology: cytochrome c oxidase and nitric oxide synthase, Curr Opin Chem Biol 3 (1999) 131-137.

[13] S. Yoshikawa, K. Muramoto, K. Shinzawa-Itoh, H. Aoyama, T. Tsukihara, T. Ogura, K. Shimokata, Y. Katayama, H. Shimada, Reaction mechanism of bovine heart cytochrome c oxidase, Biochim Biophys Acta 1757 (2006) 395-400.

[14] E.E. Chufan, S.C. Puiu, K.D. Karlin, Heme-copper/dioxygen adduct formation, properties, and reactivity, Acc Chem Res 40 (2007) 563-572.

[15] H. Li, T.L. Poulos, Structure-function studies on nitric oxide synthases, Journal of Inorganic Biochemistry 99 (2005) 293-305.

[16] T.L. Poulos, Structural and functional diversity in heme monooxygenases, Drug Metab Dispos 33 (2005) 10-18.

[17] T.L. Poulos, Intermediates in P450 catalysis, Philos Transact A Math Phys Eng Sci 363 (2005) 793-806; discussion 1035-1040.

[18] T.M. Makris, R. Davydov, I.G. Denisov, B.M. Hoffman, S.G. Sligar, Mechanistic enzymology of oxygen activation by the cytochromes P450, Drug Metab Rev 34 (2002) 691-708.

[19] J.G. Leahy, P.J. Batchelor, S.M. Morcomb, Evolution of the soluble diiron monooxygenases, FEMS Microbiol Rev 27 (2003) 449-479.

[20] S.J. Lippard, Hydroxylation of C-H bonds at carboxylate-bridged diiron centres, Philos Transact A Math Phys Eng Sci 363 (2005) 861-877; discussion 1035-1040.

[21] L.J. Murray, S.J. Lippard, Substrate trafficking and dioxygen activation in bacterial multicomponent monooxygenases, Acc Chem Res 40 (2007) 466-474.

[22] L. Que, Jr., The oxo/peroxo debate: a nonheme iron perspective, J Biol Inorg Chem 9 (2004) 684-690.

[23] I.V. Korendovych, S.V. Kryatov, E.V. Rybak-Akimova, Dioxygen activation at non-heme iron: insights from rapid kinetic studies, Acc Chem Res 40 (2007) 510-521.

[24] E.G. Kovaleva, M.B. Neibergall, S. Chakrabarty, J.D. Lipscomb, Finding intermediates in the O2 activation pathways of non-heme iron oxygenases, Acc Chem Res 40 (2007) 475-483.

[25] S.K. Lee, J.C. Nesheim, J.D. Lipscomb, Transient intermediates of the methane monooxygenase catalytic cycle, J Biol Chem 268 (1993) 21569-21577.

[26] D.J. Ferraro, L. Gakhar, S. Ramaswamy, Rieske business: structure-function of Rieske non-heme oxygenases, Biochem Biophys Res Commun 338 (2005) 175-190.

[27] D.T. Gibson, R.E. Parales, Aromatic hydrocarbon dioxygenases in environmental biotechnology, Curr Opin Biotechnol 11 (2000) 236-243.

[28] P.M. Harrison, P. Arosio, The ferritins: molecular properties, iron storage function and cellular regulation, Biochim Biophys Acta 1275 (1996) 161-203.

[29] E.C. Theil, The ferritin family of iron storage proteins, Adv Enzymol Relat Areas Mol Biol 63 (1990) 421-449.

[30] D.M. Lawson, P.J. Artymiuk, S.J. Yewdall, J.M. Smith, J.C. Livingstone, A. Treffry, A. Luzzago, S. Levi, P. Arosio, G. Cesareni, et al., Solving the structure of human H ferritin by genetically engineering intermolecular crystal contacts, Nature 349 (1991) 541-544.

[31] L. Chen, L. Keramati, J.D. Helmann, Coordinate regulation of Bacillus subtilis peroxide stress genes by hydrogen peroxide and metal ions, Proc Natl Acad Sci U S A 92 (1995) 8190-8194.

[32] O.M. Hartford, B.C. Dowds, Isolation and characterization of a hydrogen peroxide resistant mutant of Bacillus subtilis, Microbiology 140 (Pt 2) (1994) 297-304.

[33] A. Kauko, S. Haataja, A.T. Pulliainen, J. Finne, A.C. Papageorgiou, Crystal structure of Streptococcus suis Dps-like peroxide resistance protein Dpr: implications for iron incorporation, J Mol Biol 338 (2004) 547-558.

[34] E.R. Rocha, G. Owens, Jr., C.J. Smith, The redox-sensitive transcriptional activator OxyR regulates the peroxide response regulon in the obligate anaerobe Bacteroides fragilis, J Bacteriol 182 (2000) 5059-5069.

[35] C. Ferreira, D. Bucchini, M.E. Martin, S. Levi, P. Arosio, B. Grandchamp, C. Beaumont, Early embryonic lethality of H ferritin gene deletion in mice, J Biol Chem 275 (2000) 3021-3024.

[36] E.C. Theil, M. Matzapetakis, X. Liu, Ferritins: iron/oxygen biominerals in protein nanocages, J Biol Inorg Chem 11 (2006) 803-810.

[37] A. Lewin, G.R. Moore, N.E. Le Brun, Formation of protein-coated iron minerals, Dalton Trans (2005) 3597-3610.

[38] X. Liu, E.C. Theil, Ferritins: dynamic management of biological iron and oxygen chemistry, Acc Chem Res 38 (2005) 167-175.

[39] X. Liu, E.C. Theil, Ferritin as an iron concentrator and chelator target, Ann N Y Acad Sci 1054 (2005) 136-140.

[40] M.A. Carrondo, Ferritins, iron uptake and storage from the bacterioferritin viewpoint, Embo J 22 (2003) 1959-1968.

[41] T.J. Stillman, P.D. Hempstead, P.J. Artymiuk, S.C. Andrews, A.J. Hudson, A. Treffry, J.R. Guest, P.M. Harrison, The high-resolution X-ray crystallographic structure of the ferritin (EcFtnA) of Escherichia coli; comparison with human H ferritin (HuHF) and the structures of the Fe(3+) and Zn(2+) derivatives, J Mol Biol 307 (2001) 587-603.

[42] A.S. Pereira, W. Small, C. Krebs, P. Tavares, D.E. Edmondson, E.C. Theil, B.H. Huynh, Direct spectroscopic and kinetic evidence for the involvement of a peroxodiferric intermediate during the ferroxidase reaction in fast ferritin mineralization, Biochemistry 37 (1998) 9871-9876.

[43] F. Bou-Abdallah, G.C. Papaefthymiou, D.M. Scheswohl, S.D. Stanga, P. Arosio, N.D. Chasteen, mu-1,2-Peroxobridged di-iron(III) dimer formation in human H-chain ferritin, Biochem J 364 (2002) 57-63.

[44] P. Moenne-Loccoz, C. Krebs, K. Herlihy, D.E. Edmondson, E.C. Theil, B.H. Huynh, T.M. Loehr, The ferroxidase reaction of ferritin reveals a diferric mu-1,2 bridging peroxide intermediate in common with other O2-activating non-heme diiron proteins, Biochemistry 38 (1999) 5290-5295.

[45] G.N. Jameson, W. Jin, C. Krebs, A.S. Pereira, P. Tavares, X. Liu, E.C. Theil, B.H. Huynh, Stoichiometric production of hydrogen peroxide and parallel formation of ferric multimers through decay of the diferric-peroxo complex, the first detectable intermediate in ferritin mineralization, Biochemistry 41 (2002) 13435-13443.

[46] G. Zhao, F. Bou-Abdallah, X. Yang, P. Arosio, N.D. Chasteen, Is hydrogen peroxide produced during iron(II) oxidation in mammalian apoferritins?, Biochemistry 40 (2001) 10832-10838.

[47] E.R. Bauminger, A. Treffry, M.A. Quail, Z. Zhao, I. Nowik, P.M. Harrison, Stages in iron storage in the ferritin of Escherichia coli (EcFtnA): analysis of Mossbauer spectra reveals a new intermediate, Biochemistry 38 (1999) 7791-7802.

[48] G.S. Waldo, E.C. Theil, Formation of iron(III)-tyrosinate is the fastest reaction observed in ferritin, Biochemistry 32 (1993) 13262-13269.

[49] G.S. Waldo, J. Ling, J. Sanders-Loehr, E.C. Theil, Formation of an Fe(III)-tyrosinate complex during biomineralization of H-subunit ferritin, Science 259 (1993) 796-798.

[50] D. Yun, R. Garcia-Serres, B.M. Chicalese, Y.H. An, B.H. Huynh, J.M. Bollinger, Jr., (Mu-1,2-peroxo)diiron(III/III) complex as a precursor to the diiron(III/IV) intermediate X in the assembly of the iron-radical cofactor of ribonucleotide reductase from mouse, Biochemistry 46 (2007) 1925-1932.

[51] D. Yun, L. Saleh, R. Garcia-Serres, B.M. Chicalese, Y.H. An, B.H. Huynh, J.M. Bollinger, Jr., Addition of oxygen to the diiron(II/II) cluster is the slowest step in formation of the tyrosyl radical in the W103Y variant of ribonucleotide reductase protein R2 from mouse, Biochemistry 46 (2007) 13067-13073.

[52] J.M. Bollinger, Jr., D.E. Edmondson, B.H. Huynh, J. Filley, J.R. Norton, J. Stubbe, Mechanism of assembly of the tyrosyl radical-dinuclear iron cluster cofactor of ribonucleotide reductase, Science 253 (1991) 292-298.

[53] N. Ravi, J.M. Bollinger, B.H. Huynh, D.E. Edmondson, J. Stubbe, Mechanism of Assembly of the Tyrosyl Radical-Diiron(Iii) Cofactor of Escherichia-Coli Ribonucleotide Reductase .1. Mossbauer Characterization of the Diferric Radical Precursor, Journal of the American Chemical Society 116 (1994) 8007-8014.

[54] J.M. Bollinger, W.H. Tong, N. Ravi, B.H. Huynh, D.E. Edmondson, J. Stubbe, Mechanism of Assembly of the Tyrosyl Radical-Diiron(Iii) Cofactor of Escherichia-Coli Ribonucleotide Reductase .3. Kinetics of the Limiting Fe2+ Reaction by Optical, Epr, and Mossbauer Spectroscopies, Journal of the American Chemical Society 116 (1994) 8024-8032.

[55] J.M. Bollinger, W.H. Tong, N. Ravi, B.H. Huynh, D.E. Edmondson, J. Stubbe, Mechanism of Assembly of the Tyrosyl Radical-Diiron(Iii) Cofactor of Escherichia-Coli Ribonucleotide Reductase .2. Kinetics of the Excess Fe2+ Reaction by Optical, Epr, and Mossbauer Spectroscopies, Journal of the American Chemical Society 116 (1994) 8015-8023.

[56] X. Yang, Y. Chen-Barrett, P. Arosio, N.D. Chasteen, Reaction paths of iron oxidation and hydrolysis in horse spleen and recombinant human ferritins, Biochemistry 37 (1998) 9743-9750.

[57] B. Xu, N.D. Chasteen, Iron oxidation chemistry in ferritin. Increasing Fe/O2 stoichiometry during core formation, J Biol Chem 266 (1991) 19965-19970.

[58] A. Treffry, Z. Zhao, M.A. Quail, J.R. Guest, P.M. Harrison, How the presence of three iron binding sites affects the iron storage function of the ferritin (EcFtnA) of Escherichia coli, FEBS Lett 432 (1998) 213-218.

[59] K. Keyer, A.S. Gort, J.A. Imlay, Superoxide and the production of oxidative DNA damage, J Bacteriol 177 (1995) 6782-6790.

[60] B. Halliwell, J.M. Gutteridge, C.E. Cross, Free radicals, antioxidants, and human disease: where are we now?, J Lab Clin Med 119 (1992) 598-620.

[61] B. Halliwell, M. Dizdaroglu, The measurement of oxidative damage to DNA by HPLC and GC/MS techniques, Free Radic Res Commun 16 (1992) 75-87.

[62] C.E. Cross, P.A. Motchnik, B.A. Bruener, D.A. Jones, H. Kaur, B.N. Ames, B. Halliwell, Oxidative damage to plasma constituents by ozone, FEBS Lett 298 (1992) 269-272.

[63] J.M. Gutteridge, B. Halliwell, Iron toxicity and oxygen radicals, Baillieres Clin Haematol 2 (1989) 195-256.

[64] J.M. Gutteridge, Iron and oxygen: a biologically damaging mixture, Acta Paediatr Scand Suppl 361 (1989) 78-85.

[65] J.M. Gutteridge, B. Halliwell, Free Radicals in Biology and Medicine, 4th ed., Oxford University Press, 2007.

[66] I. Fridovich, Superoxide radical and superoxide dismutases, Annu Rev Biochem 64 (1995) 97-112.

[67] Y.K. Chae, Expression, purification, and characterization of the oligomeric states of rubredoxin oxidoreductase from Methanobacterium thermoautotrophicum, Mol Cells 13 (2002) 259-263.

[68] L. Chen, P. Sharma, J. Le Gall, A.M. Mariano, M. Teixeira, A.V. Xavier, A blue non-heme iron protein from Desulfovibrio gigas, Eur J Biochem 226 (1994) 613-618.

[69] M. Lombard, D. Touati, M. Fontecave, V. Niviere, Superoxide reductase as a unique defense system against superoxide stress in the microaerophile Treponema pallidum, J Biol Chem 275 (2000) 27021-27026.

[70] I. Moura, P. Tavares, J.J. Moura, N. Ravi, B.H. Huynh, M.Y. Liu, J. LeGall, Purification and characterization of desulfoferrodoxin. A novel protein from Desulfovibrio desulfuricans (ATCC 27774) and from Desulfovibrio vulgaris (strain Hildenborough) that contains a distorted rubredoxin center and a mononuclear ferrous center, J Biol Chem 265 (1990) 21596-21602.

[71] I.A. Abreu, L.M. Saraiva, J. Carita, H. Huber, K.O. Stetter, D. Cabelli, M. Teixeira, Oxygen detoxification in the strict anaerobic archaeon Archaeoglobus fulgidus: superoxide scavenging by neelaredoxin, Mol Microbiol 38 (2000) 322-334.

[72] J.V. Rodrigues, L.M. Saraiva, I.A. Abreu, M. Teixeira, D.E. Cabelli, Superoxide reduction by Archaeoglobus fulgidus desulfoferrodoxin: comparison with neelaredoxin, J Biol Inorg Chem 12 (2007) 248-256.

[73] A.P. Yeh, Y. Hu, F.E. Jenney, Jr., M.W. Adams, D.C. Rees, Structures of the superoxide reductase from Pyrococcus furiosus in the oxidized and reduced states, Biochemistry 39 (2000) 2499-2508.

[74] T. Jovanovic, C. Ascenso, K.R. Hazlett, R. Sikkink, C. Krebs, R. Litwiller, L.M. Benson, I. Moura, J.J. Moura, J.D. Radolf, B.H. Huynh, S. Naylor, F. Rusnak, Neelaredoxin, an iron-binding protein from the syphilis spirochete, Treponema pallidum, is a superoxide reductase, J Biol Chem 275 (2000) 28439-28448.

[75] R.G. Zhang, Y. Kim, T. Skarina, S. Beasley, R. Laskowski, C. Arrowsmith, A. Edwards, A. Joachimiak, A. Savchenko, Crystal structure of Thermotoga maritima 0065, a member of the IclR transcriptional factor family, J Biol Chem 277 (2002) 19183-19190.

[76] F.E. Jenney, M. Verhagen, M.W.W. Adams, Neelaredoxin from Pyrococcus furiosus is a novel type of superoxide dismutase, Journal of Inorganic Biochemistry 74 (1999) 181-181.

[77] F.E. Jenney, Jr., M.F. Verhagen, X. Cui, M.W. Adams, Anaerobic microbes: oxygen detoxification without superoxide dismutase, Science 286 (1999) 306-309.

[78] M.J. Pianzzola, M. Soubes, D. Touati, Overproduction of the rbo gene product from Desulfovibrio species suppresses all deleterious effects of lack of superoxide dismutase in Escherichia coli, J Bacteriol 178 (1996) 6736-6742.

[79] S.I. Liochev, I. Fridovich, A mechanism for complementation of the sodA sodB defect in Escherichia coli by overproduction of the rbo gene product (desulfoferrodoxin) from Desulfoarculus baarsii, J Biol Chem 272 (1997) 25573-25575.

[80] M. Lombard, M. Fontecave, D. Touati, V. Niviere, Reaction of the desulfoferrodoxin from Desulfoarculus baarsii with superoxide anion. Evidence for a superoxide reductase activity, J Biol Chem 275 (2000) 115-121.

[81] J.K. Voordouw, G. Voordouw, Deletion of the rbo gene increases the oxygen sensitivity of the sulfate-reducing bacterium Desulfovibrio vulgaris Hildenborough, Appl Environ Microbiol 64 (1998) 2882-2887.

[82] A.S. Pereira, P. Tavares, F. Folgosa, R.M. Almeida, I. Moura, J.J.G. Moura, Superoxide reductases, European Journal of Inorganic Chemistry (2007) 2569-2581.

[83] B. Devreese, P. Tavares, J. Lampreia, N. Van Damme, J. Le Gall, J.J. Moura, J. Van Beeumen, I. Moura, Primary structure of desulfoferrodoxin from Desulfovibrio desulfuricans ATCC 27774, a new class of non-heme iron proteins, FEBS Lett 385 (1996) 138-142.

[84] I. Moura, M. Bruschi, J. Le Gall, J.J. Moura, A.V. Xavier, Isolation and characterization of desulforedoxin, a new type of non-heme iron protein from Desulfovibrio gigas, Biochem Biophys Res Commun 75 (1977) 1037-1044.

[85] P. Tavares, N. Ravi, J.J. Moura, J. LeGall, Y.H. Huang, B.R. Crouse, M.K. Johnson, B.H. Huynh, I. Moura, Spectroscopic properties of desulfoferrodoxin from Desulfovibrio desulfuricans (ATCC 27774), J Biol Chem 269 (1994) 10504-10510.

[86] I. Moura, P. Tavares, N. Ravi, Characterization of three proteins containing multiple iron sites: rubrerythrin, desulfoferrodoxin, and a protein containing a six-iron cluster, Methods Enzymol 243 (1994) 216-240.

[87] K.R. Hazlett, D.L. Cox, R.A. Sikkink, F. Auch'ere, F. Rusnak, J.D. Radolf, Contribution of neelaredoxin to oxygen tolerance by Treponema pallidum, Methods Enzymol 353 (2002) 140-156.

[88] T. Santos-Silva, J. Trincao, A.L. Carvalho, C. Bonifacio, F. Auchere, I. Moura, J.J. Moura, M.J. Romao, Superoxide reductase from the syphilis spirochete Treponema pallidum: crystallization and structure determination using soft X-rays, Acta Crystallogr Sect F Struct Biol Cryst Commun 61 (2005) 967-970.

[89] A.V. Coelho, P. Matias, V. Fulop, A. Thompson, A. Gonzalez, M.A. Carrondo, Desulfoferrodoxin Structure Determined by MAD Phasing and Refinement to 1.9 Angstroms Resolution Reveals a Unique Combination of a Tetrahedral Fes4 Centre with a Square Pyramidal Fesn4 Centre, J.Biol.Inorg.Chem. 2 (1997) 680-689.

[90] V. Niviere, M. Lombard, M. Fontecave, C. Houee-Levin, Pulse radiolysis studies on superoxide reductase from Treponema pallidum, FEBS Lett 497 (2001) 171-173.

[91] M. Lombard, C. Houee-Levin, D. Touati, M. Fontecave, V. Niviere, Superoxide reductase from Desulfoarculus baarsii: reaction mechanism and role of glutamate 47 and lysine 48 in catalysis, Biochemistry 40 (2001) 5032-5040.

[92] V. Niviere, M. Asso, C.O. Weill, M. Lombard, B. Guigliarelli, V. Favaudon, C. Houee-Levin, Superoxide reductase from Desulfoarculus baarsii: identification of protonation steps in the enzymatic mechanism, Biochemistry 43 (2004) 808-818.

[93] J.P. Emerson, E.R. Farquhar, L. Que, Jr., Structural "snapshots" along reaction pathways of non-heme iron enzymes, Angew Chem Int Ed Engl 46 (2007) 8553-8556.

[94] J.V. Rodrigues, I.A. Abreu, D. Cabelli, M. Teixeira, Superoxide reduction mechanism of Archaeoglobus fulgidus one-iron superoxide reductase, Biochemistry 45 (2006) 9266-9278.

[95] J.P. Emerson, D.E. Cabelli, D.M. Kurtz, Jr., An engineered two-iron superoxide reductase lacking the [Fe(SCys)4] site retains its catalytic properties in vitro and in vivo, Proc Natl Acad Sci U S A 100 (2003) 3802-3807.

[96] W. Lovenberg, B.E. Sobel, Rubredoxin: a new electron transfer protein from Clostridium pasteurianum, Proc Natl Acad Sci U S A 54 (1965) 193-199.

[97] F. Bonomi, S. Iametti, P. Ferranti, D.M. Kurtz, Jr., A. Morleo, E.M. Ragg, "Iron priming" guides folding of denatured aporubredoxins, J Biol Inorg Chem (2008).

[98] M. Frey, L. Sieker, F. Payan, R. Haser, M. Bruschi, G. Pepe, J. LeGall, Rubredoxin from Desulfovibrio gigas. A molecular model of the oxidized form at 1.4 A resolution, J Mol Biol 197 (1987) 525-541.

[99] E.T. Adman, L.C. Sieker, L.H. Jensen, M. Bruschi, J. Le Gall, A structural model of rubredoxin from Desulfovibrio vulgaris at 2 A resolution, J Mol Biol 112 (1977) 113-120.

[100] M. Bruschi, Non-heme iron proteins. The amino acid sequence of rubredoxin from Desulfovibrio vulgaris, Biochim Biophys Acta 434 (1976) 4-17.

[101] E.J. Laishley, J. Travis, H.D. Peck, Jr., Amino acid composition of ferredoxin and rubredoxin isolated from Desulfovibrio gigas, J Bacteriol 98 (1969) 302-303.

[102] W. Lovenberg, W.M. Williams, Further observations on the chemical nature of rubredoxin from Clostridium pasteurianum, Biochemistry 8 (1969) 141-148.

[103] J.A. Peterson, M.J. Coon, Enzymatic omega-oxidation. 3. Purification and properties of rubredoxin, a component of the omega-hydroxylation system of Pseudomonas oleovorans, J Biol Chem 243 (1968) 329-334.

[104] J. Le Gall, [Partial purification and study of NAD:rubredoxin oxidoreductase from D. gigas], Ann Inst Pasteur (Paris) 114 (1968) 109-115.

[105] J.A. Peterson, M. Kusunose, E. Kusunose, M.J. Coon, Enzymatic omega-oxidation. II. Function of rubredoxin as the electron carrier in omega-hydroxylation, J Biol Chem 242 (1967) 4334-4340.

[106] M.J. Brumlik, G. Voordouw, Analysis of the transcriptional unit encoding the genes for rubredoxin (rub) and a putative rubredoxin oxidoreductase (rbo) in Desulfovibrio vulgaris Hildenborough, J Bacteriol 171 (1989) 4996-5004.

[107] F. Auchere, S.R. Pauleta, P. Tavares, I. Moura, J.J. Moura, Kinetics studies of the superoxide-mediated electron transfer reactions between rubredoxin-type proteins and superoxide reductases, J Biol Inorg Chem 11 (2006) 433-444.

[108] J.V. Rodrigues, I.A. Abreu, L.M. Saraiva, M. Teixeira, Rubredoxin acts as an electron donor for neelaredoxin in Archaeoglobus fulgidus, Biochem Biophys Res Commun 329 (2005) 1300-1305.

[109] F. Auchere, R. Sikkink, C. Cordas, P. Raleiras, P. Tavares, I. Moura, J.J. Moura, Overexpression and purification of Treponema pallidum rubredoxin; kinetic evidence for a superoxide-mediated electron transfer with the superoxide reductase neelaredoxin, J Biol Inorg Chem 9 (2004) 839-849.

[110] B.J. Henriques, L.M. Saraiva, C.M. Gomes, Combined spectroscopic and calorimetric characterisation of rubredoxin reversible thermal transition, J Biol Inorg Chem 11 (2006) 73-81.

[111] B.J. Henriques, L.M. Saraiva, C.M. Gomes, Probing the mechanism of rubredoxin thermal unfolding in the absence of salt bridges by temperature jump experiments, Biochem Biophys Res Commun 333 (2005) 839-844.

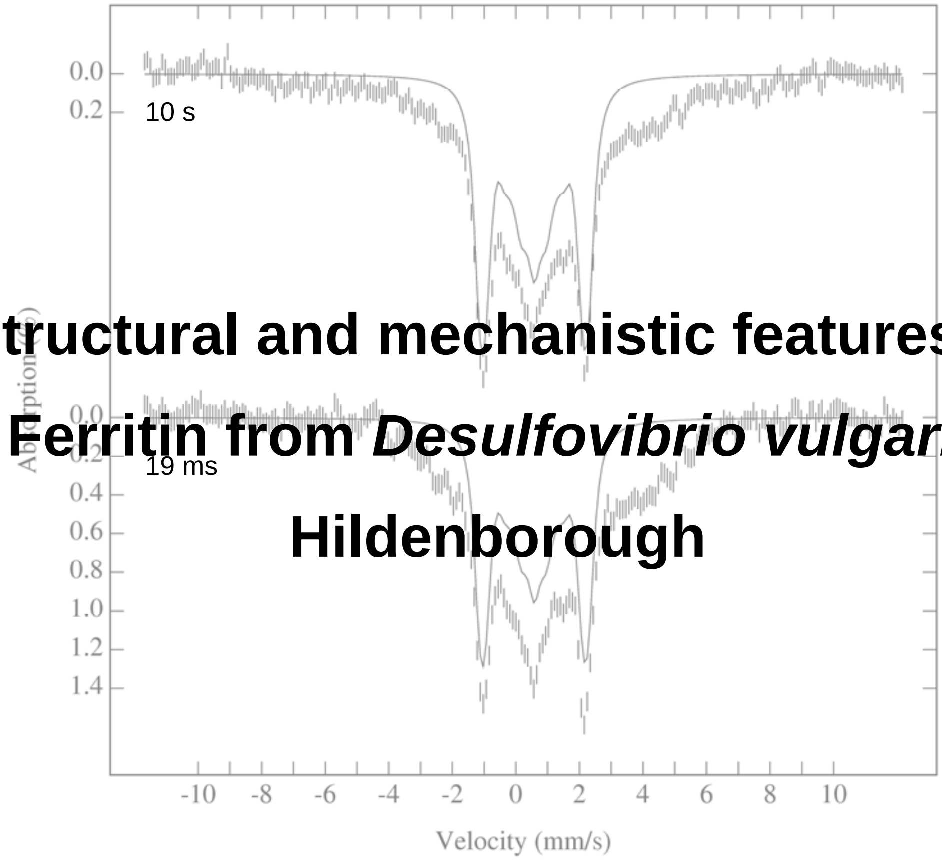

Structural and mechanistic features of Ferritin from *Desulfovibrio vulgaris* Hildenborough

Index

Chapter II

Structural and mechanistic features of Ferritin from *Desulfovibrio vulgaris* Hildenborough

II.1 – Overview

As described up to this point, organisms such as anaerobic bacteria occasionally have to deal with the presence of toxic compounds, like molecular oxygen or ROS. Thus, over the years, evolution favored bacteria like *D. vulgaris* Hildenborough, which use mechanisms that, together or on their own, are able to deal with those threats. Bacterial ferritin is going to be the first enzyme implicated in such mechanism described on this thesis.

Since this is a very complex subject, the main goal of this chapter is to present, in general, the results obtained until now concerning the capture and characterization of reaction intermediates, using fast kinetic techniques like stopped-flow (coupled with UV-Vis) and rapid freeze-quench (coupled with EPR and Mössbauer spectroscopy).

The experiments were performed with both the wild type protein and with a mutant protein, E130A. In this mutant, the glutamic acid at position 130 is substituted by an alanine. This mutation was designed to eliminate the third iron site that is thought to be present in this protein[1, 2]. The mechanistic changes due to this mutation will be discussed.

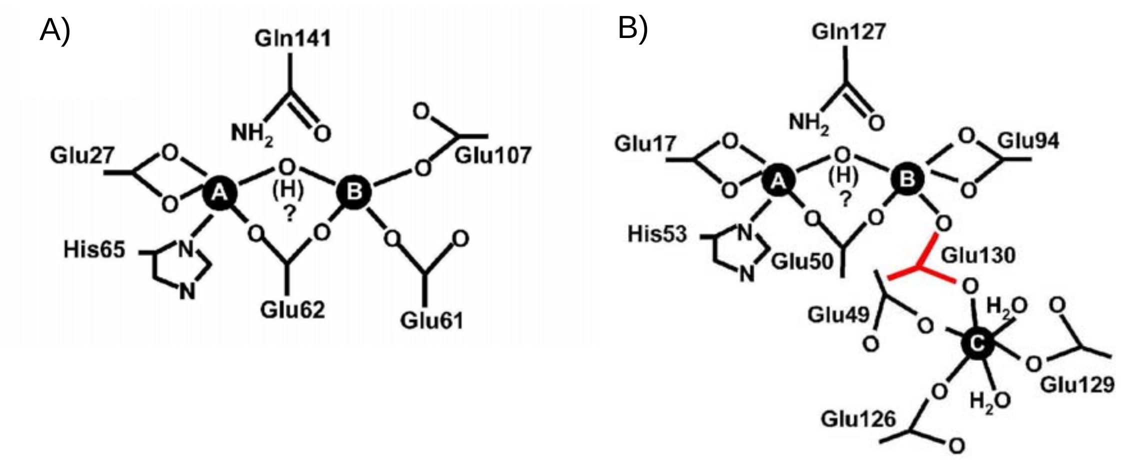

Figure II. 1 – A) Ferroxidase center of human H-chain ferritin. B) Ferroxidase center of E. coli FtnA. The glutamic acid at position 130 is marked in red. Adapted from [3].

II.2 – Experimental

II.2.1 – *Dv* Ferritin, overexpression and isolation

Both forms of recombinant ferritin, wild type (Ftn) and mutant (E130A), from *Desulfovibrio vulgaris* Hildenborough used in this work were cloned, overexpressed and isolated in our laboratory by Duarte and Guilherme[4]. All the protein samples that were used were analyzed for the iron content and purity. All samples contained less than 3 Fe/protein (data obtained by induced coupled plasma emission).

II.2.2 – Stopped-Flow and Rapid Freeze-Quench EPR and Mössbauer studies of pre-loaded wild type ferritin and E130A mutant

Two batches of protein, Ftn and E130A, were anaerobically incubated with a correct amount of a $FeSO_4$ solution in order to obtain a final ratio of 62 iron/protein. Each of these solutions was then mixed with an equal volume of an oxygen saturated buffer solution at 4 ºC and, depending on the experimental method, reactions were followed by EPR, Mössbauer or UV-Visible spectroscopies. At this temperature, it was expected to obtain a saturation of 1.2 mM O_2 in the buffer solution. Since oxygen is one of the reagents, it was important to have a concentration that ensures that it was not limiting. All these assays were performed at pH 7.6 in 200 mM Tris-HCl and 200 mM NaCl at pH 7.6.

II.2.2.1 - Rapid Freeze-Quench EPR and Mössbauer studies

The experimental setup and the procedures used in this work were identical to the previously described by Ravi and coworkers and consist of a set of drive syringes controlled by a Ram Unit and a home-built quenching bath. The bath holds liquid isopentane which is cooled and maintained at -140 ºC by liquid nitrogen and a precision temperature controller[5].

The RFQ procedure involves mixing two reactants rapidly and efficiently through a mixing chamber, allowing the reaction to proceed for a specific period of time, ranging from 19 ms to 1h and 30 min, freeze-quenching the reaction mixture by squirting it into the quenching bath containing isopentane at -140 ºC, and packing the frozen ice crystals of the reaction mixture through a sample-collecting apparatus into a Mössbauer sample cell. The different reaction times are controlled by the length, and diameter, of the aging hose as well as flow rate. For example, for a flow rate of 0.833 mL/s a hose with a cross-sectional area of 0.00203 cm^2 and a length of 40.7 cm one obtains a 100 ms reaction time[5-7].

As mentioned before, these experiments were carried out at 4 ºC. To accomplish this experimental request, both drive syringes and aging hoses were submerged in a temperature controlled water bath.

Mössbauer measurements were carried out at 4.2 K with an applied magnetic field parallel to the γ radiation beam either in a weak-field Mössbauer spectrometer or on a strong-field Mössbauer spectrometer. Both spectrometers were operated in a constant acceleration mode and the zero velocity of the Mössbauer spectra refers to the centroid of the room temperature spectrum of a metallic iron foil. The Mössbauer spectra analysis was performed using WMOSS software (WEB Research).

The experimental procedure used for the RFQ EPR experiments was similar to the one described for the RFQ Mössbauer. In this case, the samples were packed into an EPR tube instead.

EPR measurements were carried out at 12 K. The obtained spectra were converted with Condor software and analyzed with WinEPR and SimFonia (Bruker).

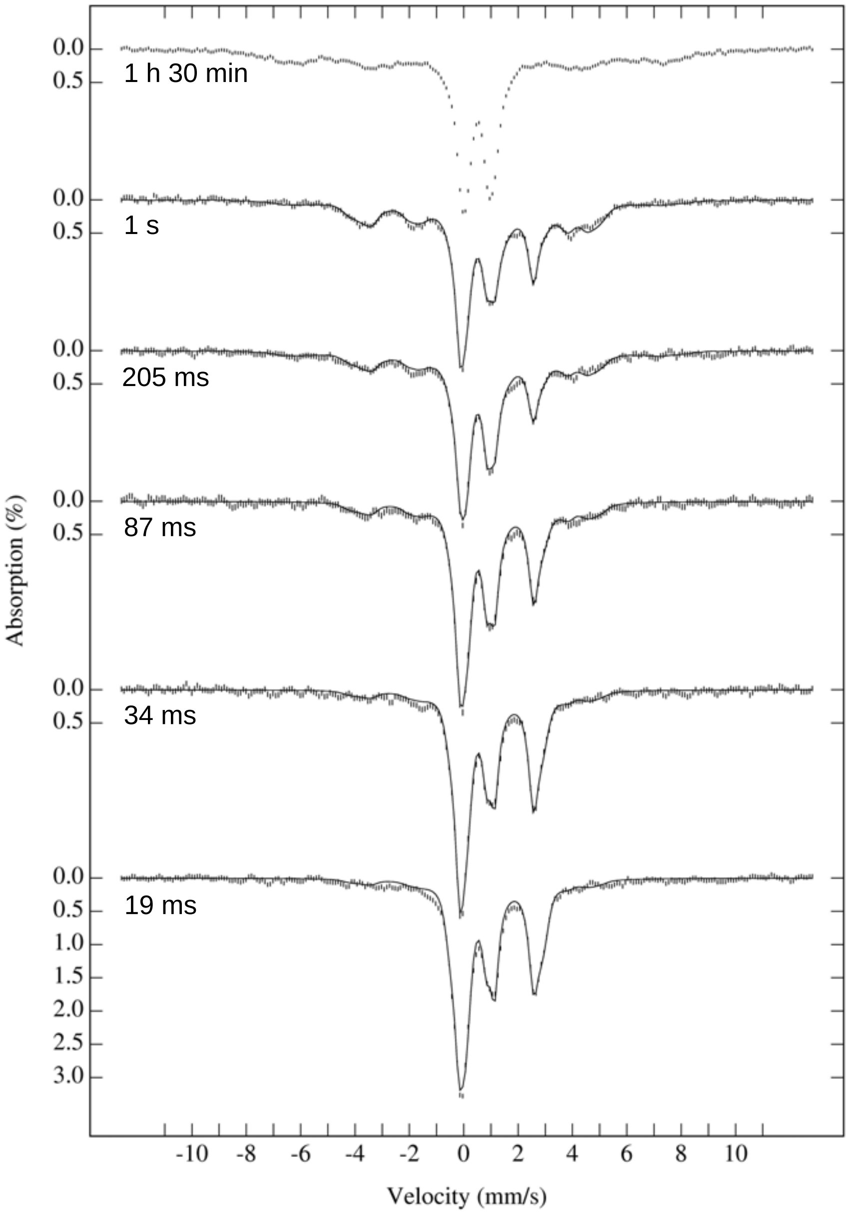

Figure II. 2 - Time dependent Mössbauer spectra of the reaction of *Dv* ferritin, 62 irons/protein, with O_2-saturated buffer. The solid lines over the experimental data are simulations of a sum of a ferrous species, a peroxodiferric species and a ferric species. The Mössbauer spectra were recorded at 4.2 K in the presence of a weak magnetic field of 500 G parallel to the γ radiation beam.

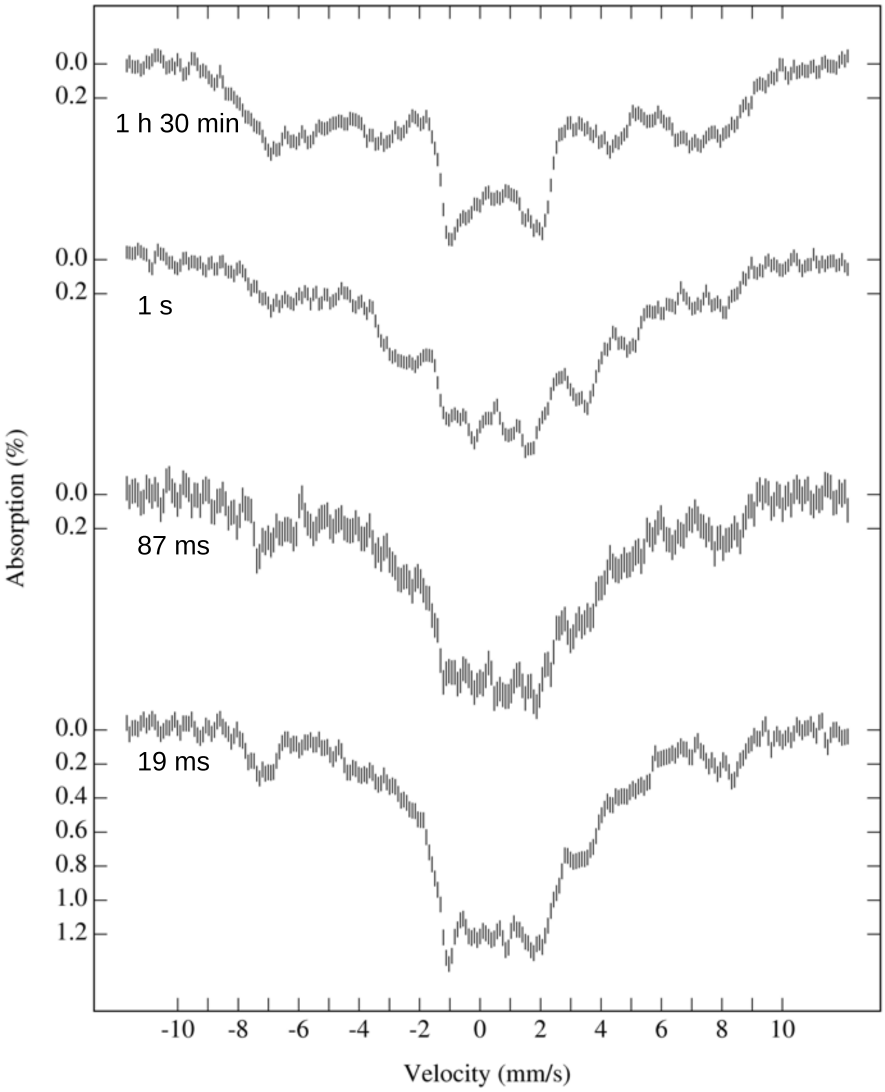

Figure II. 3 - Time dependent Mössbauer spectra of the reaction of *Dv* ferritin, 62 irons/protein, with O_2-saturated buffer. The Mössbauer spectra were recorded at 4.2 K in the presence of a strong magnetic field of 80 kG parallel to the γ radiation beam.

From the data analysis of both weak-field and strong-field Mössbauer spectra it was possible to detect the formation of two intermediate species between the initial ferrous species and the final young mineral core. One is a peroxodiferric species with parameters, ΔE_Q = 1.11 mm/s and δ = 0.58 mm/s, which are characteristic of this type of complexes and similar to the previously published in other diiron enzymes[8, 9]. The other is a mixed-valence species (Fe^{2+}-Fe^{3+}) with parameters, ΔE_Q = -1.03 mm/s and δ = 0.51 corresponding to a Fe^{3+} site (S=5/2) and ΔE_Q = 2.25 mm/s and δ = 1.16 corresponding to a Fe^{2+} site (S=2). The parameters calculated for the ferric species, ΔE_Q = 0.69 mm/s and δ = 0.50 mm/s, can represent a fast relaxation young core. The ferrous components with parameters ΔE_Q = 3.35 mm/s and δ = 1.25 mm/s for doublet I and ΔE_Q = 2.72 mm/s and δ = 1.20 mm/s for doublet II, correspond to the not-yet-reacted Fe^{2+}. All the parameters calculated for the Mössbauer spectra are summarized in the next tables.

Table II. 1 - Mössbauer parameters of ferrous species, peroxodiferric species and ferric species at weak magnetic field

	Ferrous species		Peroxodiferric species	Ferric species
	Doublet I	Doublet II		
δ (mm/s)	1.25 ± 0.04	1.20 ± 0.03	0.58 ± 0.03	0.50 ± 0.03
ΔE_Q (mm/s)	3.35 ± 0.03	2.72 ± 0.03	1.11 ± 0.03	0.69 ± 0.04
Γ (G)	-0.45/-0.45	0.35/0.45	0.35/0.35	0.40/0.40

Table II. 2 - Mössbauer parameters of the mixed-valence species

	Fe^{3+} site	Fe^{2+} site
δ (mm/s)	0.51 ± 0.03	1.16 ± 0.03
ΔE_Q (mm/s)	–1.03 ± 0.03	2.25 ± 0.03
η	1.0	0
$A/g_N\beta_N$ (G)	(–458, –531, –560)	(299, 203, 188)
Γ (G)	0.5	0.5
g-values	1.95, 1.82, 1.82	

Table II. 3 - Mössbauer percentage of the total Fe absorption of the different species at various reaction times

time	Ferrous species	Peroxodiferric species	Ferric species	Mixed-valence	Young mineral core
19 ms	47	23	19	11	0
34 ms	46	21	20	13	0
87 ms	36	19	22	23	0
205 ms	21	13	20	27	19
1 s	22	11	14	36	17

Given the information obtained from the above data, it was expected to identify the formation of a mixed-valence species in the EPR experiments. However, no mixed-valence species were identified. This fact can be associated to a possible light sensitivity of this mixed-valence species.

The formation of a radical species was identified instead. This species is similar to the previously identified as a tyrosyl radical in other diiron proteins such as RNR-R2[5, 10-12]. According to the samples studied, the tyrosyl radical is already formed at 19 ms and increases its signal until 1 s reaction time. Because this is an ongoing project, there is insufficient data to calculate formation and decay rates. Thus, it is difficult to predict the role of this species in the catalytic mechanism in study.

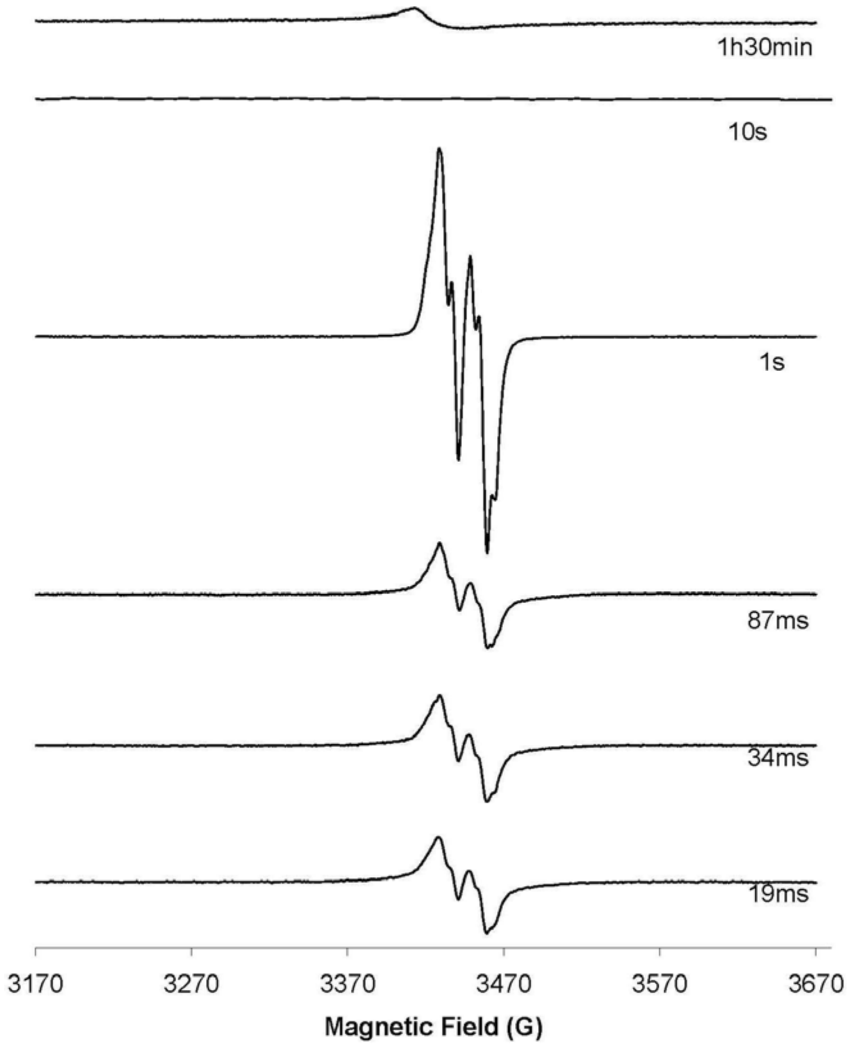

Figure II. 4 - Time dependent EPR spectra of the reaction of *Dv* ferritin with O_2-saturated buffer. The experimental conditions used were: temperature 12 K; microwave frequency 9.656 GHz; microwave power 2 mW; modulation amplitude 5 mT; receiver gain 1.26 x 10^5 and attenuation of 30 dB.

From the data analysis of both weak-field (figure II.5) and strong-field (figure II.6) Mössbauer spectra of E130A mutant samples, it was possible to detect the formation of only one intermediate species between the initial ferrous species and the final young mineral core. The calculated parameters point to a peroxodiferric species with, ΔE_Q = 1.11 mm/s and δ = 0.58 mm/s. These values are similar to the ones calculated for Ftn meaning that they are also similar to the previously published in other diiron enzymes[8, 9]. The ferrous components with parameters ΔE_Q = 3.27 mm/s and δ = 1.27 mm/s for site I and ΔE_Q = 2.75 mm/s and δ = 1.25 mm/s for site II, correspond to the not-yet-reacted Fe^{2+} (S=2). All the parameters calculated for the Mössbauer spectra are summarized in the next tables.

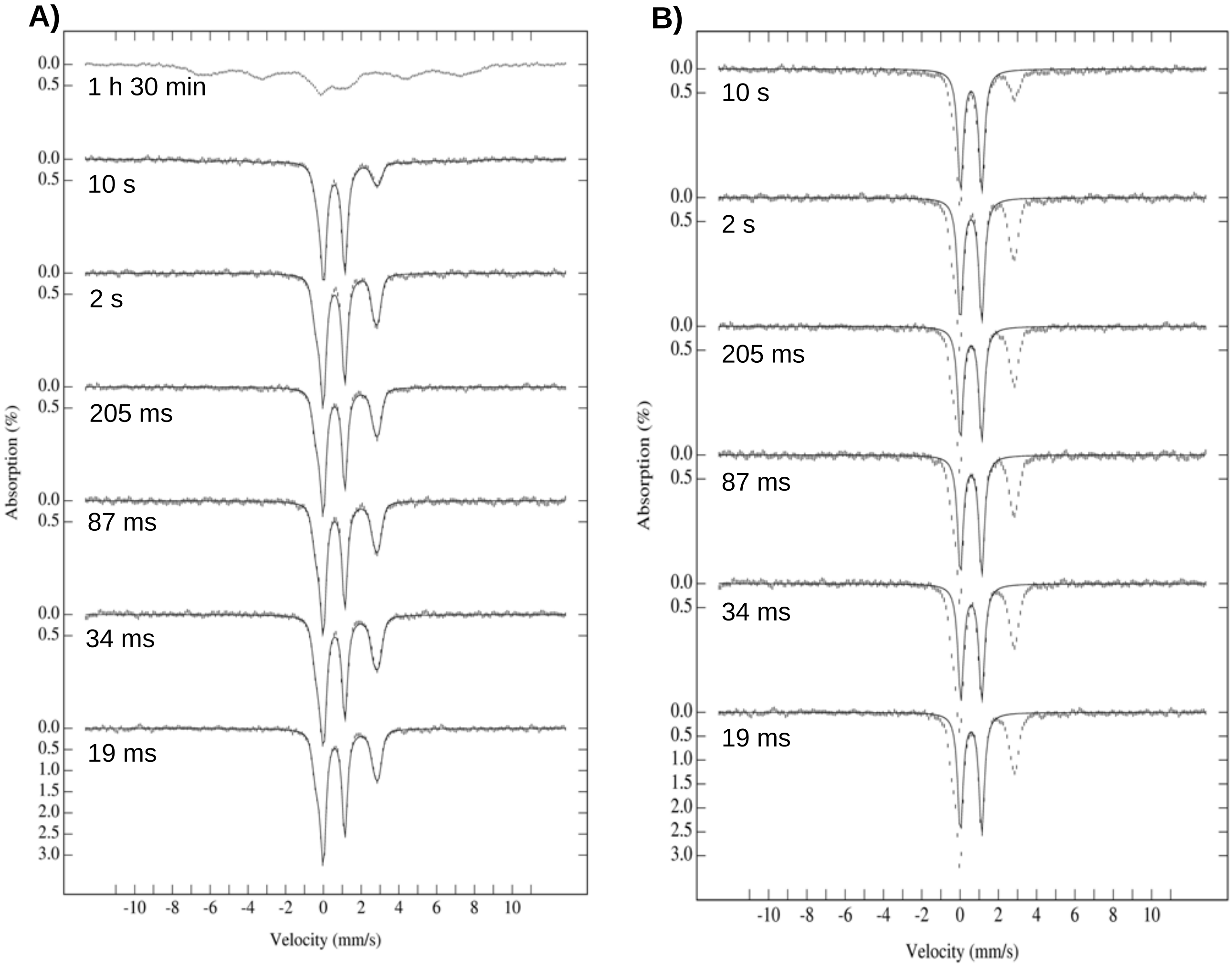

Figure II. 5 – A) Time dependent Mössbauer spectra of the reaction of E130A mutant, 62 irons/protein, with O_2-saturated buffer. The solid lines over the experimental data are simulations of a sum of a ferrous component and a peroxodiferric species. B) The experimental spectra are the same as in A) but the solid line represents only the simulation for the peroxodiferric species in each sample. The Mössbauer spectra were recorded at 4.2 K in the presence of a weak magnetic field of 500 G parallel to the γ radiation beam.

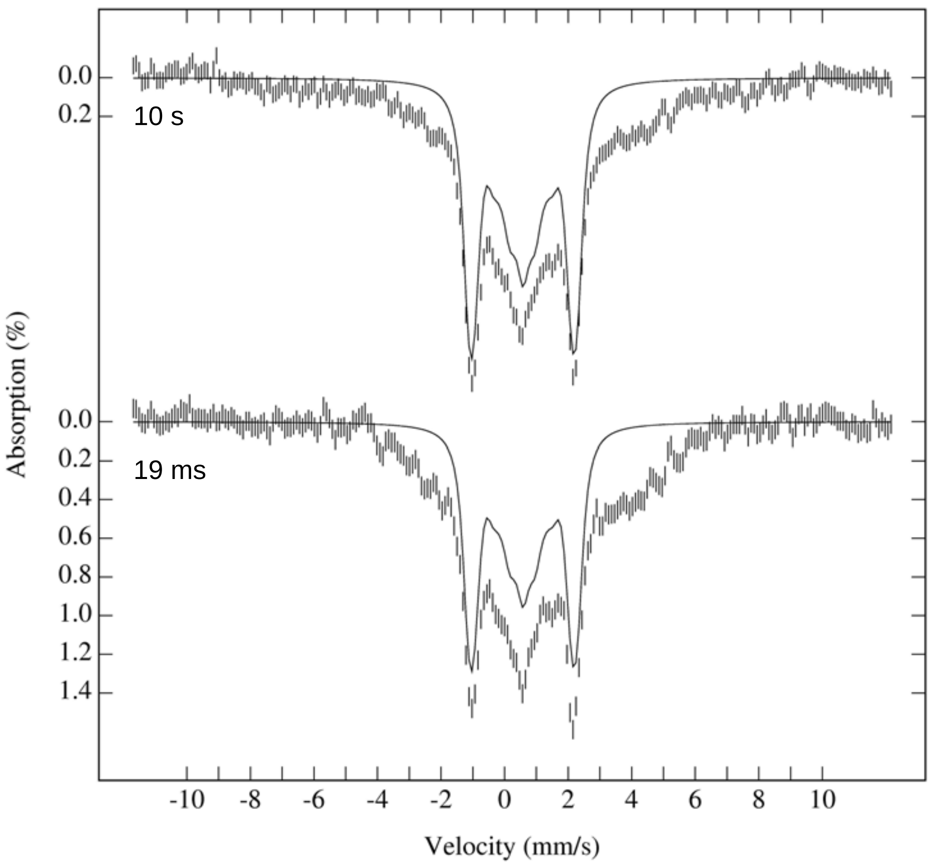

Figure II. 6 - Time dependent Mössbauer spectra of the reaction of E130A mutant with O_2-saturated buffer. The solid lines over the experimental data are simulations of the peroxodiferric species present in each sample. The Mössbauer spectra were recorded at 4.2 K in the presence of a strong magnetic field of 80 kG parallel to the γ radiation beam.

Table II. 4 - Mössbauer parameters of ferrous and peroxodiferric species

	Ferrous		Peroxodiferric	
	Weak field		Weak field	Strong field
	Site I	Site II		
δ (mm/s)	1.27 ± 0.03	1.25 ± 0.03	0.58 ± 0.03	0.57 ± 0.03
ΔE_Q (mm/s)	3.27 ± 0.03	2.75 ± 0.03	1.11 ± 0.03	1.13 ± 0.03
η	–	–	–	0.96
Width (G)	-0.44/-0.42	0.35/0.45	0.34	0.40

Table II. 5 – Mössbauer percentage of the total Fe absorption of the different species at various reaction times

time	Ferrous	Peroxodiferric	Core
19 ms	42	58	0
34 ms	45	55	0
87 ms	41	59	0
205 ms	39	61	0
2 s	38	62	0
10 s	19	61	20
1 h 30 min	0	<5.0	95-100

Contrary to the data obtained in the RFQ EPR studies performed with Ftn, the experiments with the E130A mutant didn't reveal any paramagnetic features in the EPR spectra. In a certain way this is in accordance with the absence of mixed-valence species detection in the Mössbauer spectra. Considering that, in this case, only the peroxodiferric species was observed besides the ferrous species and the mineral core it is possible to assume, in a first approach, that the glutamic acid 130 is directly related to the catalytic mechanism of the enzyme, preventing the formation of mixed-valence and tyrosyl radical species. On the other hand, it was observed that this mutation does not affect the formation of mineral core. Another difference is the formation and decay profile of the peroxodiferric species that, in this case, is somehow stabilized.

II.2.2.2 – Stopped-Flow studies

In order to have parallel UV-Vis data for these experiments, a similar study was performed by stopped-flow, coupled to a diode array spectrophotometer. In this case the entire procedure was performed anaerobically inside a glove box (UniLab from mBraun) (see Appendix B). The protein solutions were degassed in a Schlenk line before being introduced inside the glove box. The results were used to compare to the data obtained from the RFQ EPR and Mössbauer.

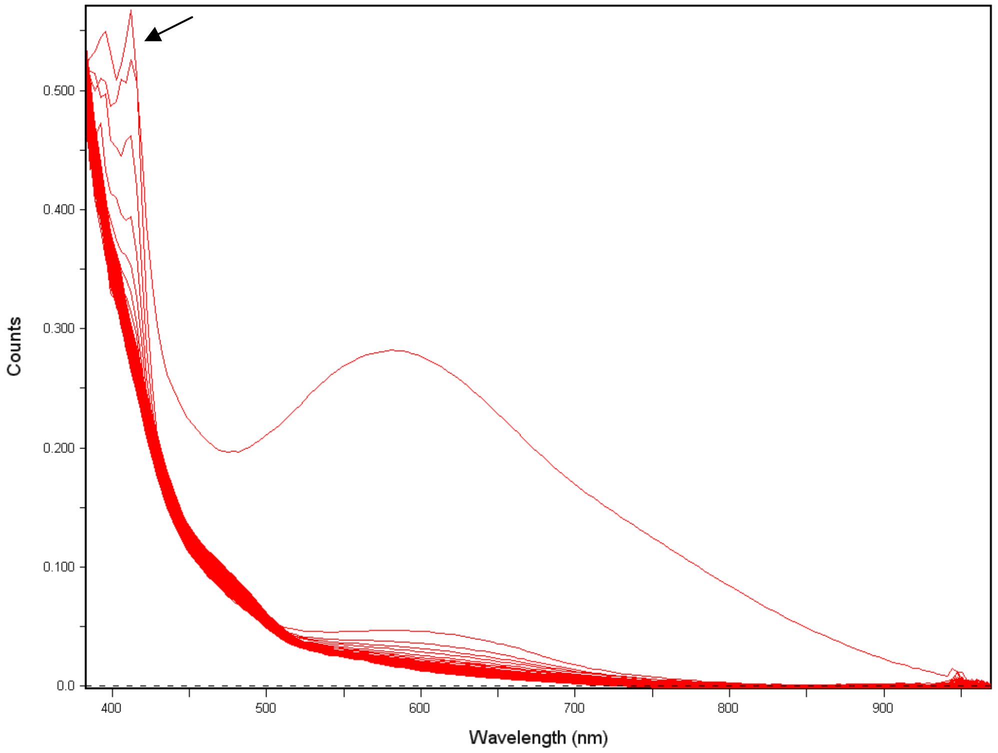

Figure II. 7 - 2D Spectral evolution of Fe^{2+} incorporation in ferritin. The assay was performed to a final concentration of 25 μM Ftn and 62 Fe/protein at pH 7.6 in 200 mM Tris-HCl plus 200 mM NaCl. The arrow points to the 412 nm peak.

As mentioned before, due to its complexity this project is still under study. However, it is possible to point out some experimental observations that, together with the data obtained by Mössbauer spectroscopy and EPR spectroscopy, can lead to a few preliminary conclusions. Thus, from the 2D spectra obtained from the stopped-flow experiment it is possible to identify the appearance of two features, a broad peak with maximum absorbance at 580 nm, and a sharp peak with maximum absorbance at 412 nm. Together with the information obtained from Mössbauer spectroscopy, it is possible to assume that the band around 580 nm can be due to the formation of a peroxodiferric species, similar to the described for other diiron proteins[9, 13, 14]. On the other hand, the sharp band with maximum at 412 nm resembles the tyrosyl radical species previously described by Bollinger and coworkers, for the RNR-R2 mechanism[8, 11, 15, 16]. This band can be also related to the radical species observed in the EPR spectra of the RFQ parallel samples.

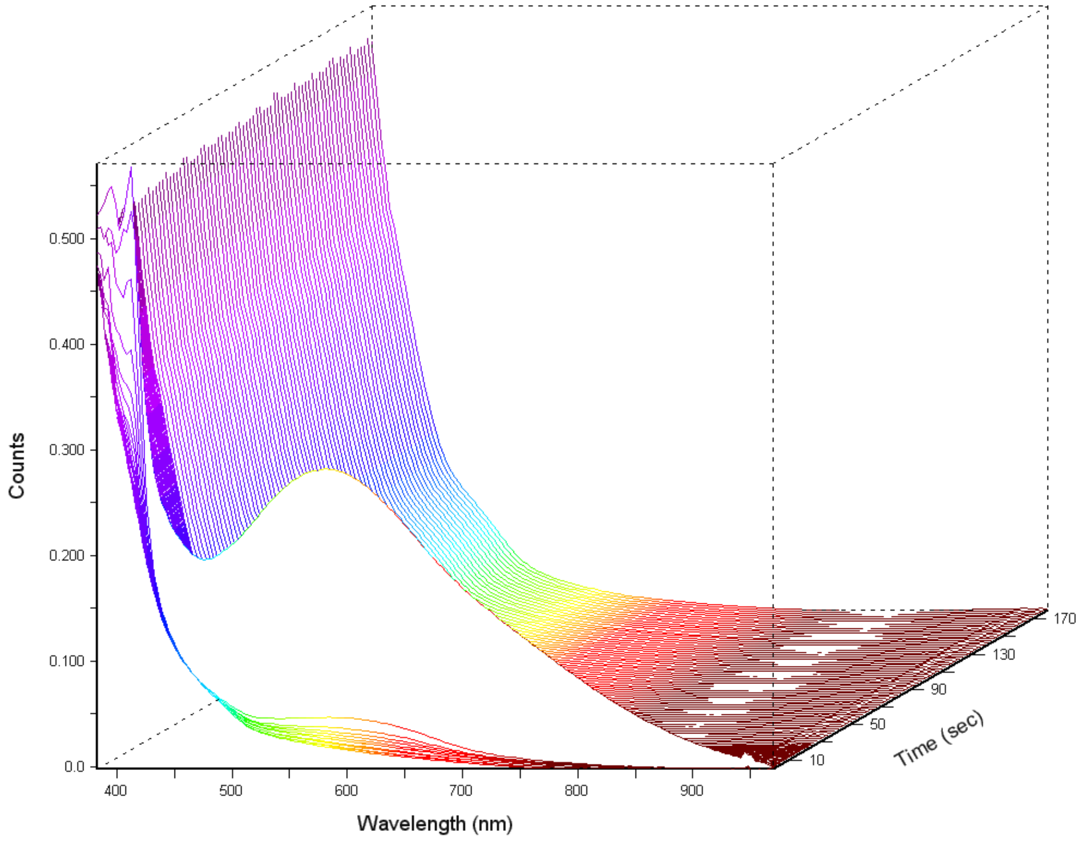

Figure II. 8 - 3D Spectral evolution of Fe^{2+} incorporation in ferritin. The assay was performed to a final concentration of 25 μM Ftn and 62 Fe/protein at pH 7.6 in 200 mM Tris-HCl plus 200 mM NaCl.

For an improved analysis, the data was collected in 3D mode. Thus, a special software, SPECFIT© (from Spectrum Software Associates), was used to in order to fit the original 3D data and calculate a reaction mechanism model where all wavelengths contribute to the kinetic constants calculation. Another advantage of this software is its ability to isolate the spectra of all intermediate species present in the reaction.

In order to fit the experimental data a set of different kinetic mechanisms were used. The best results were obtained when a four consecutive exponential model was applied. Each of these exponentials corresponds to a first order rate constant according to Eq. II.1.

$$A \xrightarrow{k_1} B \xrightarrow{k_2} C \xrightarrow{k_3} D \xrightarrow{k_4} E \qquad \text{Eq. II.1}$$

In this model A corresponds to a species, with no visible spectrum, where the ferrous iron is possibly attached to the protein, B corresponds to the peroxodiferric species, C corresponds to the tyrosyl radical, D corresponds to an unidentified reaction intermediate and E corresponds to the young mineral core. The formation of B was determined to be a very fast process, impossible to detect with this technique. Thus, only k_2, k_3 and k_4 were calculated and determined to be (222 ± 2) s^{-1}, (20.6± 0.1) s^{-1} and 0.02 s^{-1}, respectively.

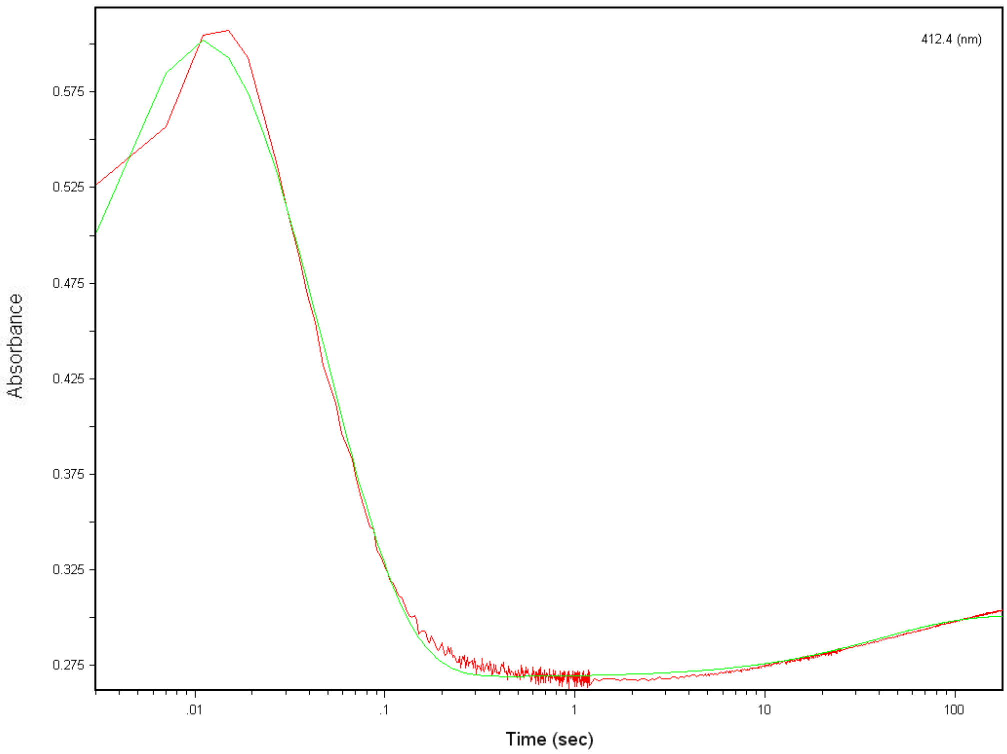

Figure II. 9 – Kinetic trace recorded at 412 nm of a 1:1 mixture (v/v) of 50 μM Ftn incubated anaerobically with $FeSO_4$ to a final ratio of 62 Fe/protein at pH 7.6 in 200 mM Tris-HCl plus 200mM NaCl. The green line represents the values obtained from the fit of the theoretical model to the experimental data.

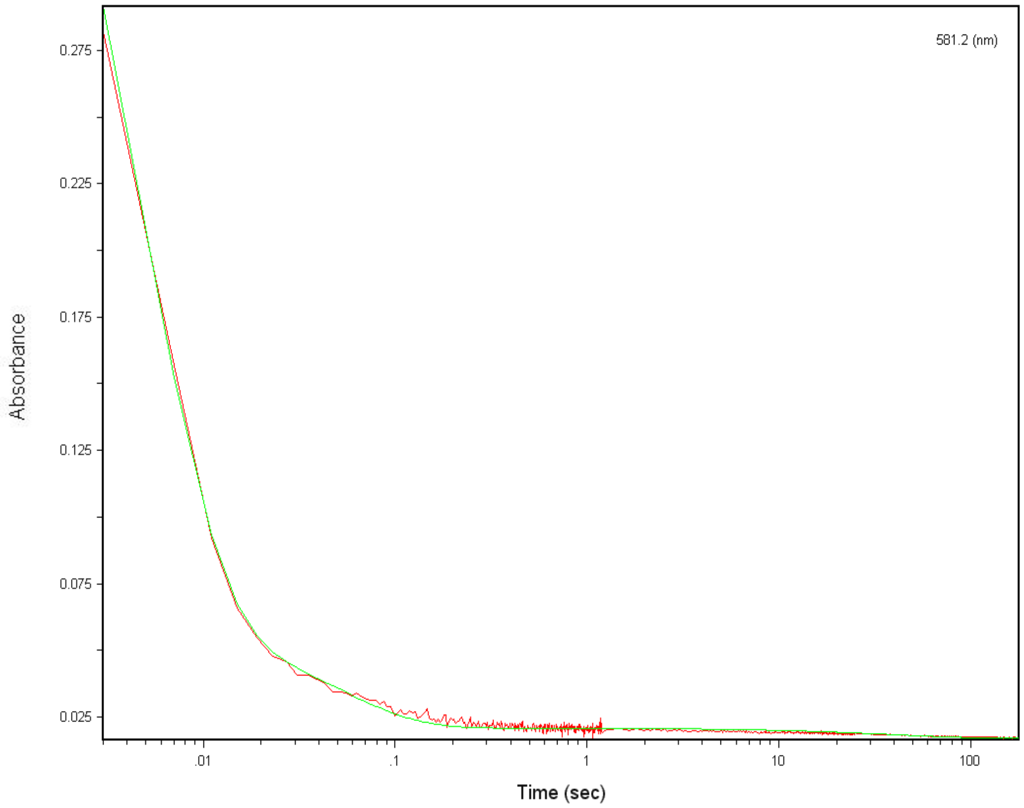

Figure II. 10 - Kinetic trace recorded at 581 nm of a mixture 1:1 (v/v) of 50 μM Ftn incubated anaerobically with $FeSO_4$ to a final ratio of 62 Fe/protein at pH 7.6 in 200 mM Tris-HCl plus 200mM NaCl. The green line represents the values obtained from the fit of the theoretical model to the experimental data.

From the two examples presented above (figure II.9 and figure II.10) it is possible to assume that the model applied is a good fit for the experimental data. This model also makes possible the spectral deconvolution of each species. To do that, the concentration of each species is calculated along the experimental time based on the respective extinction coefficients.

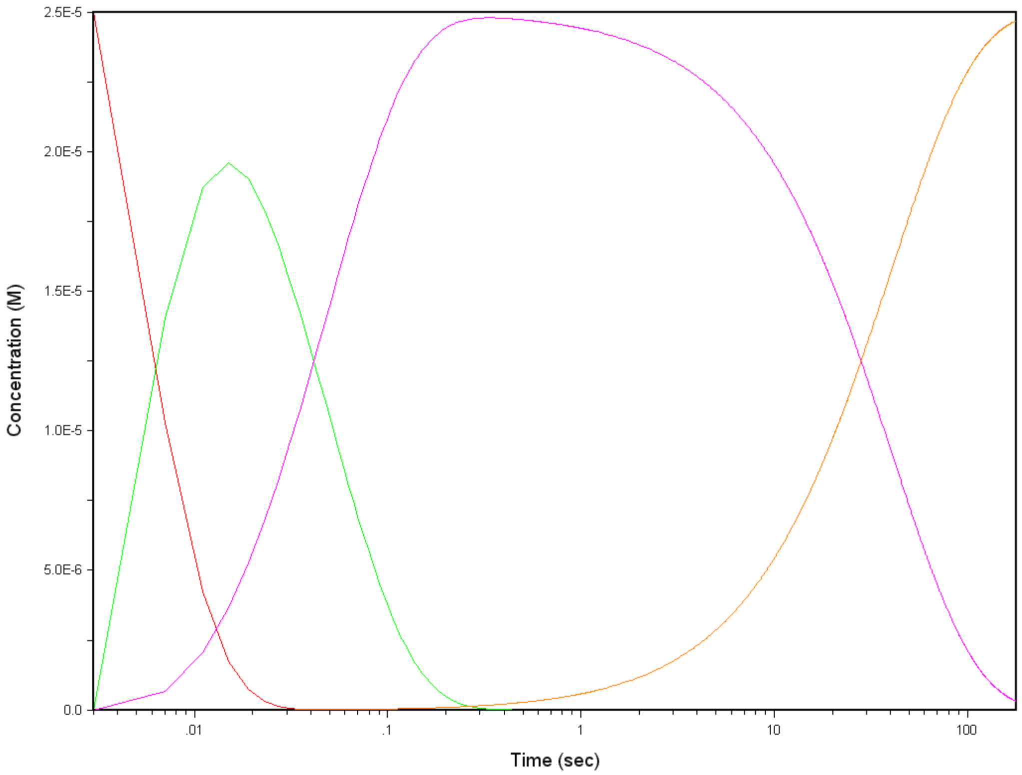

Figure II. 11 – Simulated species evolution through time of a 1:1 mixture (v/v) of 50 μM Ftn incubated anaerobically with $FeSO_4$ to a final ratio of 62 Fe/protein at pH 7.6 and 200 mM Tris-HCl plus 200 mM NaCl. Red line corresponds to B species (peroxodiferric), green line corresponds to C species (tyrosyl radical), pink line corresponds to D species and orange line corresponds to E species (young mineral core).

In accordance with the described above, figure II. 11 also shows that, in the experimental timescale, the peroxodiferric was already formed and is the first observable species, followed by the formation of the tyrosyl radical. These two species present distinct visible spectra, as showed in figure II.12. With the exception of the tyrosyl radical, the spectral properties of the observable species are very similar to the ones previously described by Bou-Abdallah and coworkers for the Human H-chain ferritin[17].

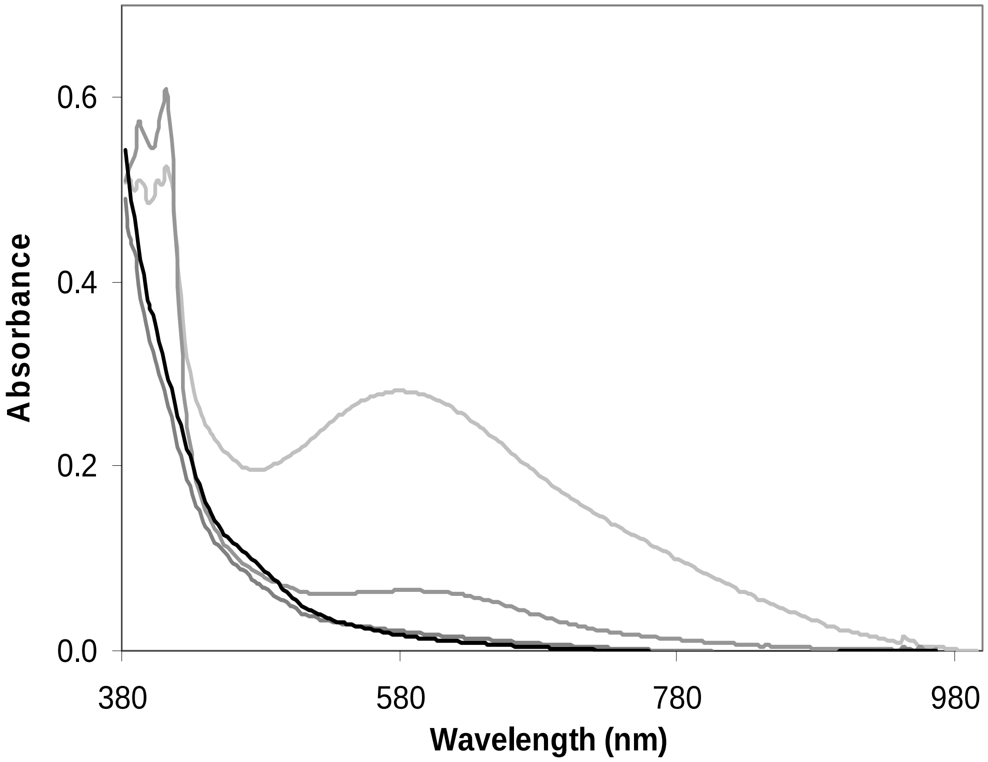

Figure II. 12 – Visible spectra obtained for each species isolated according to the kinetic model applied. Light gray stands for the peroxodiferric species, gray for tyrosyl radical species (B and C in the proposed mechanism, respectively), dark gray for D species and black for young mineral core (E in the proposed mechanism). These species were obtained from a 1:1 mixture (v/v) of 50 μM Ftn incubated anaerobically with $FeSO_4$ to a final ratio of 62 Fe/protein at pH 7.6 in 200 mM Tris-HCl plus 200 mM NaCl.

When the stopped-flow data was compared to the quantifications obtained from Mössbauer spectroscopy (figure II.13) it was possible to observe that the peroxodiferric species decay was superimposable to the 412 nm kinetic trace. This is a strange behaviour because the absorbance at 412 nm was attributed to the formation of a radical species and from the stopped-flow data the peroxodiferric species is formed before the tyrosyl radical. This aspect is still under study.

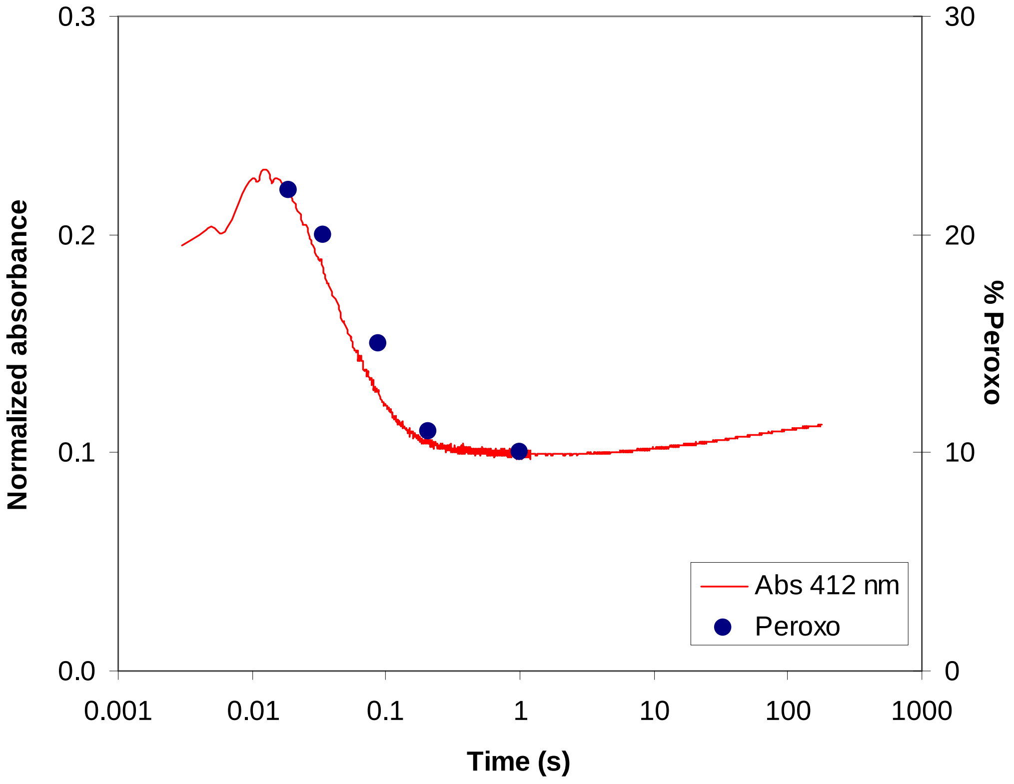

Figure II. 13 – Normalized absorbance at 412 nm superimposed with percentages obtained from the Mössbauer spectra for peroxodiferric species.

In order to compare the behaviour of Ftn versus the E130A mutant, the same set of experiments (in similar experimental conditions) was performed. The results will, hopefully, help to understand the existence and functionality of the third iron site in this ferritin.

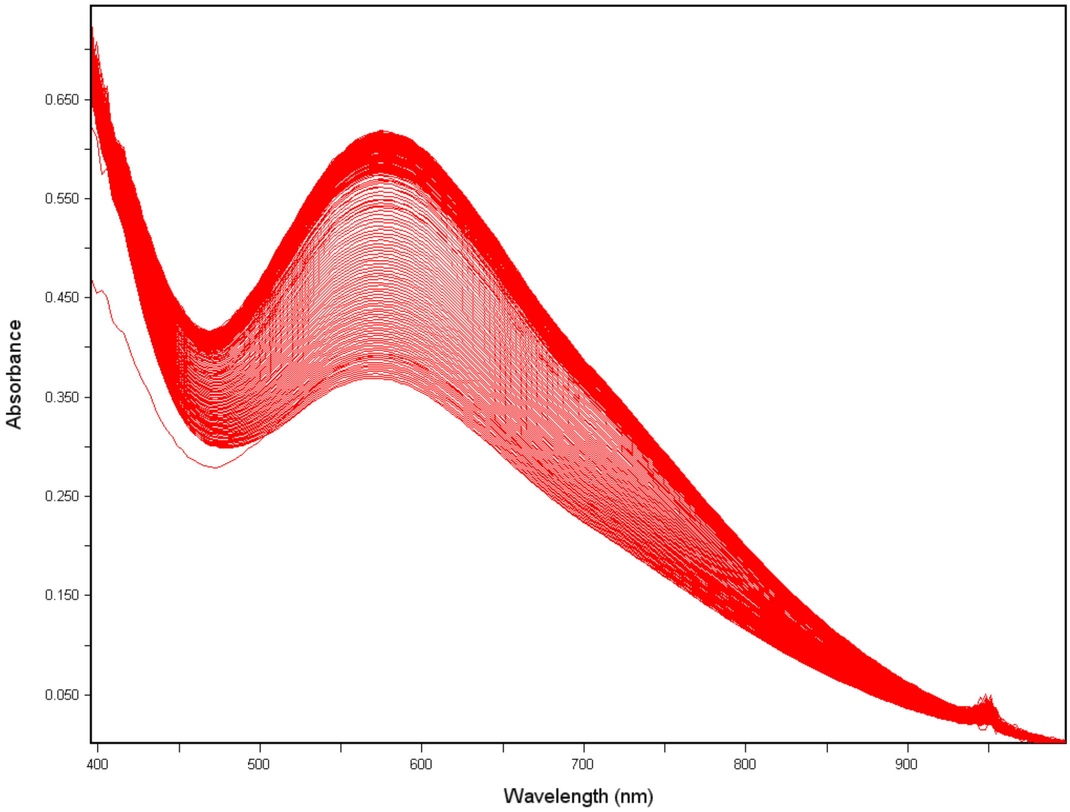

Figure II. 14 - 2D Spectral evolution of Fe^{2+} incorporation in E130A mutant. The assay was performed to a final concentration of 28 µM E130A and 62 Fe/protein at pH 7.6 in 200 mM Tris-HCl plus 200 mM NaCl.

Contrary to the observed in the wt protein, in the E130A mutant only the formation of a broad peak with maximum near 580 nm is observed. Like in Ftn, this feature is related to the formation of a peroxodiferric species, similar to the ones described for other diiron proteins[9, 13, 14]. The lack of the absorption band at 412 nm could also mean that, in this case, no tyrosyl radical is formed during the ferroxidatic process. This fact is consistent with the absence of paramagnetic species in the EPR spectra of parallel samples. Considering that experimental conditions were the same in both cases, it is also clear that in this case the peroxodiferric intermediate is again stabilized.

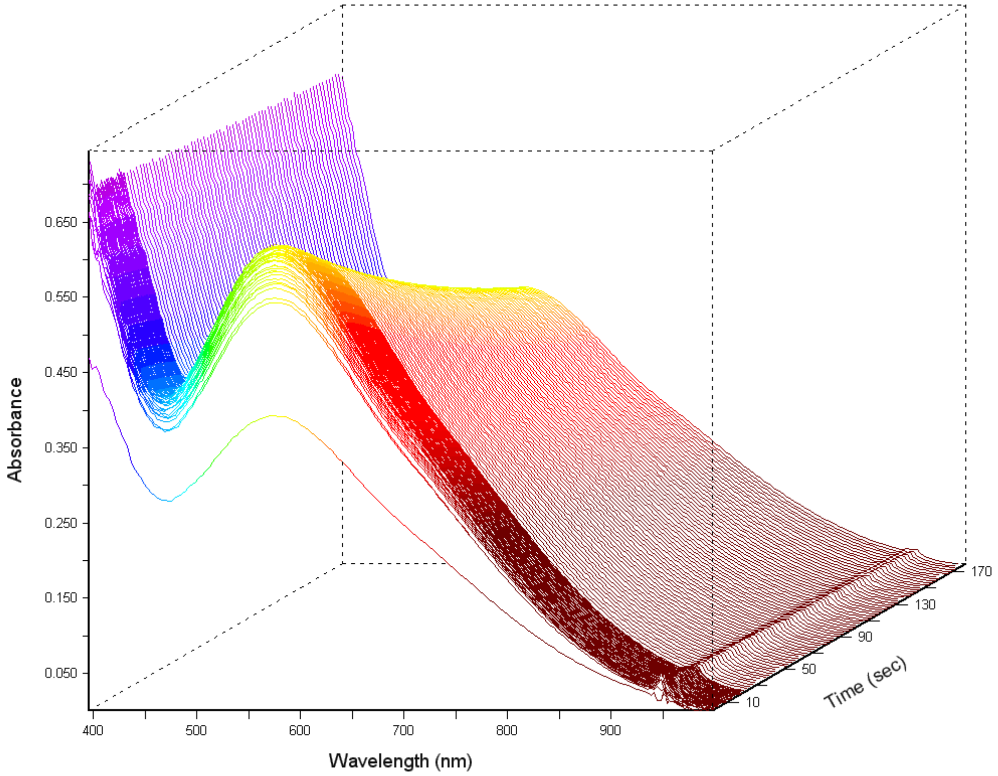

Figure II. 15 - 3D Spectral evolution of Fe^{2+} incorporation in E130A mutant. The assay was performed to a final concentration of 28 μM E130A and 62 Fe/protein at pH 7.6 in 200 mM Tris-HCl plus 200 mM NaCl.

Since there is no structural information about the influence of the mutation it is not possible to associate the observed differences to the lack of the third site. Nevertheless, by direct comparison with the wild type protein, this mutation clearly changes the enzymatic mechanism of this protein.

In accordance with the observable differences, the global analysis also raises another difference. In this case a different model was applied in order to get a good fit to the experimental data. Contrary to what was used for Ftn, a three consecutive exponential model was used to fit the experimental data of E130A mutant.

$$A \xrightarrow{k_1} B \xrightarrow{k_2} C \xrightarrow{k_3} D \qquad \text{Eq. II.2}$$

In this model, A corresponds to a species (with no visible spectrum) where the ferrous iron is possibly attached to the protein, B and C are very similar spectroscopically and probably correspond to two different peroxodiferric species and D is the iron core. The assumption of two different peroxodiferric species was based on the fact that they have different visible spectra (figure II.18) and the kinetic data cannot be fitted assuming only one peroxodiferric species. This difference is not observable in the Mössbauer spectroscopy data. Contrary to Ftn, it was possible to calculate all the kinetic rate constants. Thus, k_1, k_2 and k_3 were calculated and determined to be (180 ± 1) s^{-1}, (3.18 ± 0.02) s^{-1} and 0.004 s^{-1}, respectively.

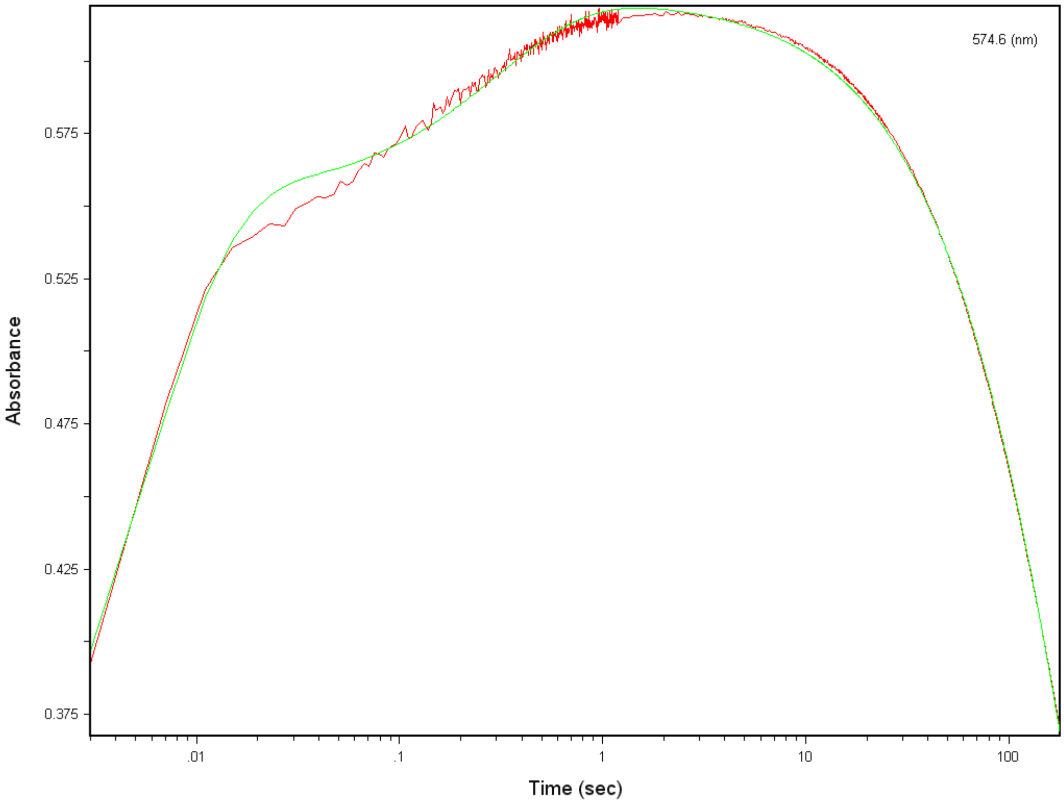

Figure II. 16 – Kinetic trace recorded at 575 nm of a 1:1 mixture (v/v) of 56 μM E130A mutant incubated anaerobically with $FeSO_4$ to a final ratio of 62 Fe/protein at pH 7.6 in 200 mM Tris-HCl plus 200 mM NaCl. The green line represents the values obtained from the fit of the theoretical model to the experimental data.

Figure II.16 illustrates the fit between the theoretical model and the experimental data. The following table resumes the values obtained for the kinetic rate constants.

Table II. 6 – Kinetic rate constants calculated from the fit of the stopped-flow data

Protein	k (s^{-1})			
	k_1	k_2	k_3	k_4
Ftn	n.d.	222 ± 2	20.6 ± 0.1	0.02 ± 0.00
E130A	180 ± 1	3.18 ± 0.02	0.004 ± 0.00	-

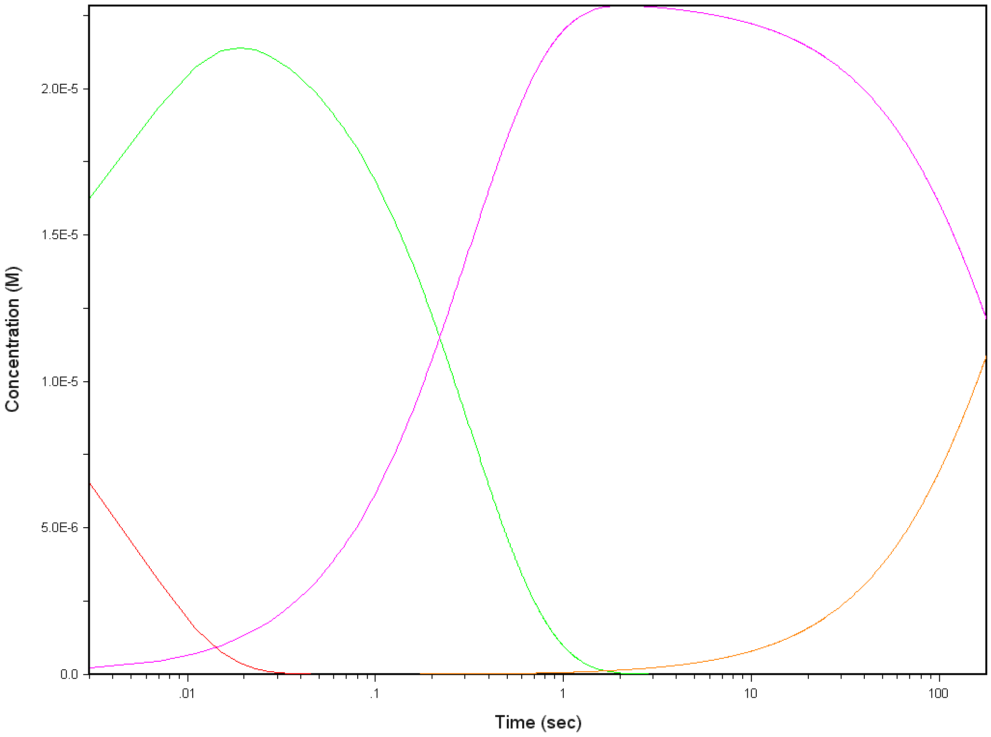

Figure II. 17 - Species evolution in time of a 1:1 mixture (v/v) of 56 μM E130A mutant incubated anaerobically with $FeSO_4$ to a final ratio of 62 Fe/protein at pH 7.6 in 200 mM Tris-HCl plus 200mM NaCl. Red line corresponds to A species, green line corresponds to B species (peroxodiferric), pink line corresponds to C species (peroxodiferric) and orange line corresponds to D species (young mineral core).

Figure II.17 shows that a peroxodiferric species is the first one to be formed and is followed by the formation of a second peroxodiferric species. They are both more stable than the equivalent species in the wt protein leading, in this case, to a slower reaction.

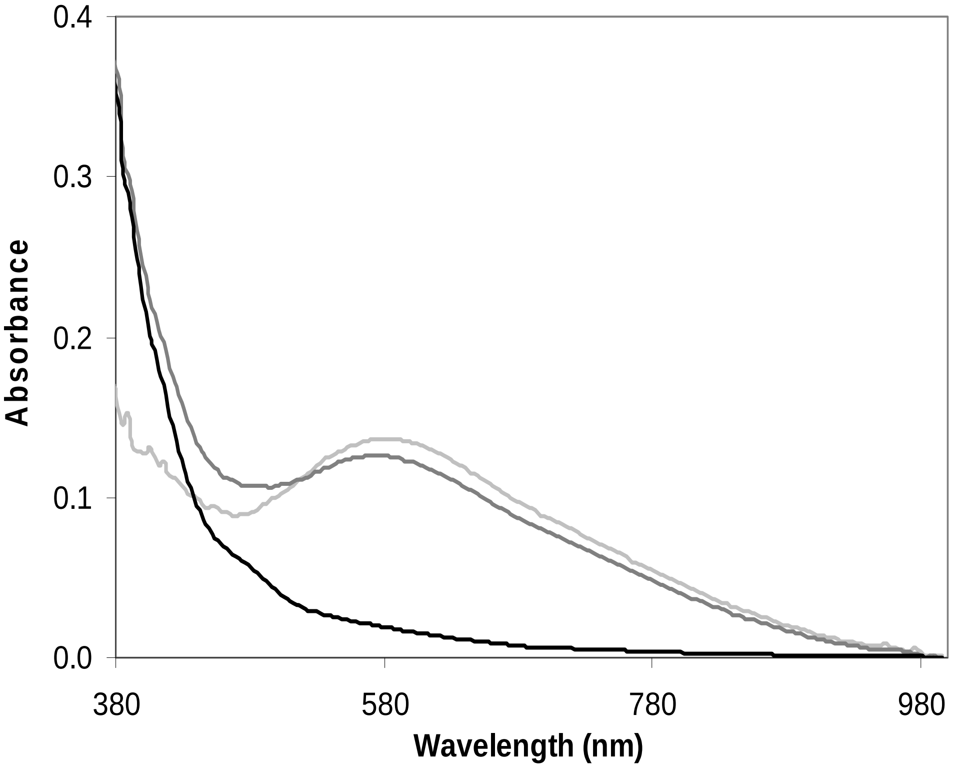

Figure II. 18 - Visible spectra obtained for each species isolated according the kinetic model applied. Light gray stands for the peroxodiferric species, gray for the second peroxodiferric species (B and C in the proposed mechanism, respectively), black for young mineral core (D in the proposed mechanism). These species were obtained from a 1:1 mixture (v/v) of 56 μM E130A incubated anaerobically with $FeSO_4$ to a final ratio of 62 Fe/protein at pH 7.6 in 200 mM Tris-HCl plus 200mM NaCl.

In Figure II.19 the kinetic trace recorded at 575 nm is superimposed with the percentages obtained from the Mössbauer spectra for the peroxodiferric species. This figure proves, as expected, that the formation and decay profiles are identical in both techniques. Using this information it was also possible to calculate the extinction coefficient for the peroxodiferric species in this protein. Thus, it was determined to be $\varepsilon_{575} \approx 1600\ M^{-1}.cm^{-1}$. A comparison between the extinction coefficients of some peroxodiferric species is presented in table II.7.

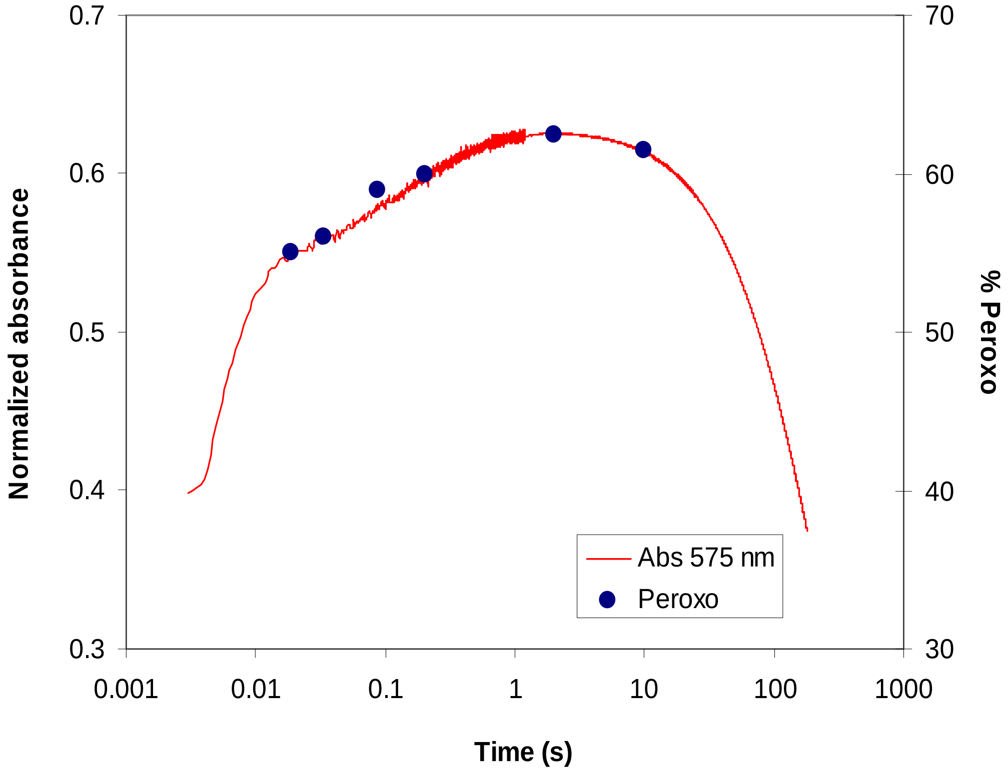

Figure II. 19 - Normalized absorbance at 575 nm superimposed with percentages obtained from the Mössbauer spectra for peroxodiferric species.

Table II. 7 – Extinction coefficient values published for different peroxodiferric species[18]. The values for E130A are the ones obtained in this work.

Protein	λ (nm)	ε ($M^{-1}.cm^{-1}$)
E130A	575	≈ 1600
Frog M ferritin	650	≈ 1000
Methylococcus capsulatus MMO	700	≈ 1800
RNR-R2 mutants	700	≈ 1500
Δ9 Desaturase	700	≈ 1200

II.3 – Discussion

Even though this is a complex and still ongoing project, it is possible to highlight some experimental evidence obtained in this work. One of the main goals was the characterization of the enzymatic mechanism of this protein, as well as the physiological relevance of the putative third iron site.

The experiments performed with the wt protein revealed some common features with other diiron proteins, such as the formation of a peroxodiferric species, a tyrosyl radical and mixed-valence intermediates [5, 6, 10-12, 18-20]. The absence of formation of both tyrosyl radical and mixed-valence species in the E130A mutant may indicate that the third iron site is directly involved in the catalytic mechanism, probably as a complementary electron pathway to the binuclear iron center. Like in ferritin A from *E. coli* (FtnA), this additional (third) iron site can confer a biological advantage to the cell since it may enable the complete reduction of oxygen to water, avoiding the formation of ROS like hydrogen peroxide[21].

Another observed difference between the two proteins was the rate of iron oxidation, corroborated by the distinct kinetic rate constants calculated for both proteins. The wt protein was shown to perform a faster iron oxidation. In accordance with this observation, the peroxodiferric intermediates formed in the E130A mutant are in some way stabilized, leading to a slower process.

From the direct observation of the data obtained by EPR spectroscopy it was possible to conclude that only the wt protein produces paramagnetic species. This species is spectroscopically similar to the tyrosyl radical species previously described for RNR-R2 [8, 11, 12, 15, 16]. The absence of a detectable mixed-valence species (identified by Mössbauer spectroscopy) can be explained with a possible light sensitivity of this species, meaning that, in this case, the energy received by the protein when exposed to light was enough to promote the decay of the mixed-valence species. On the other hand, the E130A mutant does not produce any EPR-active species, which is in accordance with the absence of mixed-valence species in the Mössbauer spectra and a tyrosyl radical in visible spectra.

The data collected from Mössbauer spectroscopy also revealed differences between the Ftn and E130A forms. The spectra collected for the E130A mutant only show one intermediate species (peroxodiferric), and the initial high-spin ferrous (S=2) and the final product, young mineral core. Besides these species, the Ftn Mössbauer spectra shows additional paramagnetic species, such as the mixed-valence, with parameters characteristic of a high-spin ferrous (S=2) coupled to a high-spin ferric (S=5/2), typical of a dinuclear iron cluster mixed-valence form.

The different behavior of these two protein forms is also demonstrated in the visible spectroscopy data obtained in the stopped-flow experiments. The kinetic models used for both wt and mutant proteins also provided information about the possible catalytic relevance of the third site. For the wt protein a four consecutive steps model was applied, meaning that the catalytic activity of this protein generates, at least, three intermediate species (with clear changes in the visible spectrum).

Furthermore, this model not only proved to be a good approach to the experimental data but also helped to isolate the visible spectrum of each species formed. The isolated spectra are in accordance with the previously published for other diiron proteins, meaning that the intermediate species formed in this case are spectroscopicaly similar [17].

The experimental data obtained for the E130A mutant can be fitted with a three consecutive step model, meaning that in this case only two intermediate species are observed. These intermediate species have similar visible spectra, resembling a peroxodiferric species, like the ones observed for the wt and for other diiron proteins. The formation of this peroxodiferric intermediate is, in this case, in good agreement with the percentages calculated based on the Mössbauer spectra for that species.

Thus, the absence (or simply the structural change promoted by the mutation) of the third iron site in this protein appears to be related to the observed mechanistic changes, including the absence of formation of some intermediate species such as the tyrosyl radical, mixed-valence and the stability of the peroxodiferric species.

This may also indicate that these intermediate species are formed between the third iron site and one of the others that form the usual binuclear iron site. Hence, even though we do not have information concerning the structural changes in E130A, it is possible to assume that the mutated amino acid acts like a bridge between the binuclear iron site and the third iron site, making possible their interaction as well as the formation reactive species such as the tyrosyl radical and the mixed-valence species.

Therefore, the existence of this third iron site can be relevant from the biological point of view if we consider that, since the protein has more iron sites, it can promote the incorporation of not only more iron ions but also more molecular oxygen per protein monomer, raising the efficiency of the enzyme when compared to others that only have two iron sites.

This is a very important fact considering that this protein is expressed in an anaerobe organism and therefore it can be useful both as an iron storage protein and an oxygen tolerance protein.

II.4 – References

[1] F. Bou-Abdallah, M.R. Woodhall, A. Velazquez-Campoy, S.C. Andrews, N.D. Chasteen, Thermodynamic analysis of ferrous ion binding to Escherichia coli ferritin EcFtnA, Biochemistry 44 (2005) 13837-13846.

[2] T.J. Stillman, P.D. Hempstead, P.J. Artymiuk, S.C. Andrews, A.J. Hudson, A. Treffry, J.R. Guest, P.M. Harrison, The high-resolution X-ray crystallographic structure of the ferritin (EcFtnA) of Escherichia coli; comparison with human H ferritin (HuHF) and the structures of the Fe(3+) and Zn(2+) derivatives, J Mol Biol 307 (2001) 587-603.

[3] A. Lewin, G.R. Moore, N.E. Le Brun, Formation of protein-coated iron minerals, Dalton Trans (2005) 3597-3610.

[4] A.G. Duarte, Biomineralização em bactérias Anaerobias. Caracterização de intermediários Catalíticos, Dep. Química, Universidade Nova de Lisboa, Lisboa, 2007.

[5] N. Ravi, J.M. Bollinger, B.H. Huynh, D.E. Edmondson, J. Stubbe, Mechanism of Assembly of the Tyrosyl Radical-Diiron(Iii) Cofactor of Escherichia-Coli Ribonucleotide Reductase .1. Mossbauer Characterization of the Diferric Radical Precursor, Journal of the American Chemical Society 116 (1994) 8007-8014.

[6] J.M. Bollinger, Jr., W.H. Tong, N. Ravi, B.H. Huynh, D.E. Edmondson, J.A. Stubbe, Use of rapid kinetics methods to study the assembly of the diferric-tyrosyl radical cofactor of E. coli ribonucleotide reductase, Methods Enzymol 258 (1995) 278-303.

[7] L.J. Murray, S.G. Naik, D.O. Ortillo, R. Garcia-Serres, J.K. Lee, B.H. Huynh, S.J. Lippard, Characterization of the arene-oxidizing intermediate in ToMOH as a diiron(III) species, Journal of the American Chemical Society 129 (2007) 14500-14510.

[8] D. Yun, R. Garcia-Serres, B.M. Chicalese, Y.H. An, B.H. Huynh, J.M. Bollinger, Jr., (Mu-1,2-peroxo)diiron(III/III) complex as a precursor to the diiron(III/IV)

intermediate X in the assembly of the iron-radical cofactor of ribonucleotide reductase from mouse, Biochemistry 46 (2007) 1925-1932.

[9] A.S. Pereira, W. Small, C. Krebs, P. Tavares, D.E. Edmondson, E.C. Theil, B.H. Huynh, Direct spectroscopic and kinetic evidence for the involvement of a peroxodiferric intermediate during the ferroxidase reaction in fast ferritin mineralization, Biochemistry 37 (1998) 9871-9876.

[10] J.M. Bollinger, Jr., D.E. Edmondson, B.H. Huynh, J. Filley, J.R. Norton, J. Stubbe, Mechanism of assembly of the tyrosyl radical-dinuclear iron cluster cofactor of ribonucleotide reductase, Science 253 (1991) 292-298.

[11] J.M. Bollinger, W.H. Tong, N. Ravi, B.H. Huynh, D.E. Edmondson, J. Stubbe, Mechanism of Assembly of the Tyrosyl Radical-Diiron(Iii) Cofactor of Escherichia-Coli Ribonucleotide Reductase .2. Kinetics of the Excess Fe2+ Reaction by Optical, Epr, and Mossbauer Spectroscopies, Journal of the American Chemical Society 116 (1994) 8015-8023.

[12] J.M. Bollinger, W.H. Tong, N. Ravi, B.H. Huynh, D.E. Edmondson, J. Stubbe, Mechanism of Assembly of the Tyrosyl Radical-Diiron(Iii) Cofactor of Escherichia-Coli Ribonucleotide Reductase .3. Kinetics of the Limiting Fe2+ Reaction by Optical, Epr, and Mossbauer Spectroscopies, Journal of the American Chemical Society 116 (1994) 8024-8032.

[13] F. Bou-Abdallah, G.C. Papaefthymiou, D.M. Scheswohl, S.D. Stanga, P. Arosio, N.D. Chasteen, mu-1,2-Peroxobridged di-iron(III) dimer formation in human H-chain ferritin, Biochem J 364 (2002) 57-63.

[14] P. Moenne-Loccoz, C. Krebs, K. Herlihy, D.E. Edmondson, E.C. Theil, B.H. Huynh, T.M. Loehr, The ferroxidase reaction of ferritin reveals a diferric mu-1,2 bridging peroxide intermediate in common with other O2-activating non-heme diiron proteins, Biochemistry 38 (1999) 5290-5295.

[15] D. Yun, C. Krebs, G.P. Gupta, D.F. Iwig, B.H. Huynh, J.M. Bollinger, Jr., Facile electron transfer during formation of cluster X and kinetic competence of X for tyrosyl

radical production in protein R2 of ribonucleotide reductase from mouse, Biochemistry 41 (2002) 981-990.

[16] D. Yun, L. Saleh, R. Garcia-Serres, B.M. Chicalese, Y.H. An, B.H. Huynh, J.M. Bollinger, Jr., Addition of oxygen to the diiron(II/II) cluster is the slowest step in formation of the tyrosyl radical in the W103Y variant of ribonucleotide reductase protein R2 from mouse, Biochemistry 46 (2007) 13067-13073.

[17] F. Bou-Abdallah, G. Zhao, H.R. Mayne, P. Arosio, N.D. Chasteen, Origin of the unusual kinetics of iron deposition in human H-chain ferritin, J Am Chem Soc 127 (2005) 3885-3893.

[18] J. Hwang, C. Krebs, B.H. Huynh, D.E. Edmondson, E.C. Theil, J.E. Penner-Hahn, A short Fe-Fe distance in peroxodiferric ferritin: control of Fe substrate versus cofactor decay?, Science 287 (2000) 122-125.

[19] Y. Kim, X. Feng, S.J. Lippard, Synthesis, structure, and properties of a mixed-valent triiron complex of tetramethyl reductic acid, an ascorbic acid analogue, and its relationship to a functional non-heme iron oxidation catalyst system, Inorg Chem 46 (2007) 6099-6107.

[20] L. Xie, S. Liu, C. Gao, R. Cao, J. Cao, C. Sun, Z. Su, Mixed-valence iron(II, III) trimesates with open frameworks modulated by solvents, Inorg Chem 46 (2007) 7782-7788.

[21] A. Treffry, Z. Zhao, M.A. Quail, J.R. Guest, P.M. Harrison, How the presence of three iron binding sites affects the iron storage function of the ferritin (EcFtnA) of Escherichia coli, FEBS Lett 432 (1998) 213-218.

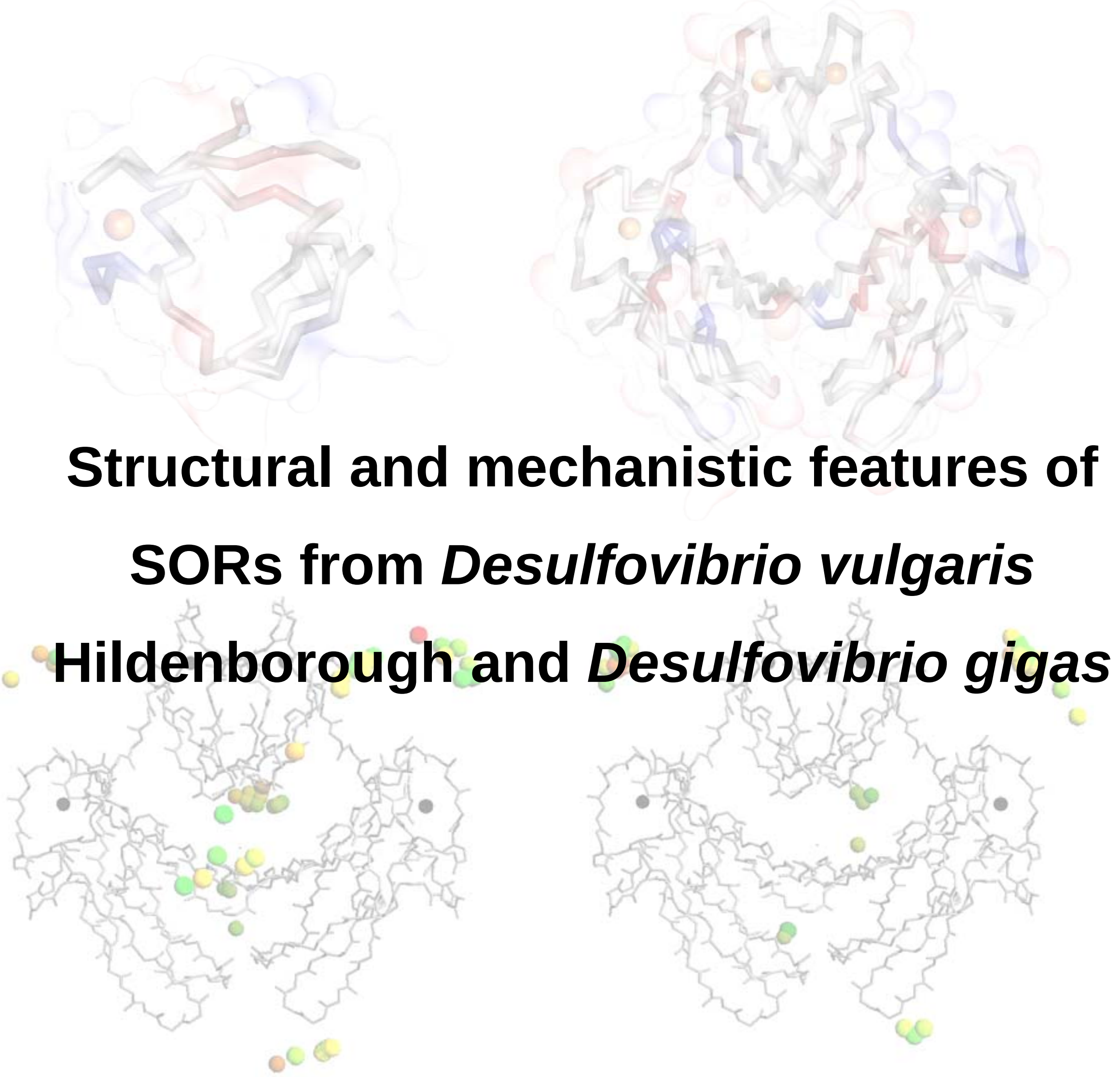

Structural and mechanistic features of SORs from *Desulfovibrio vulgaris* Hildenborough and *Desulfovibrio gigas*

Index

Chapter III

Structural and mechanistic features of SORs from *Desulfovibrio vulgaris* Hildenborough and *Desulfovibrio gigas*

III.1 – Overview

As mentioned in Chapter I, the SOR proteins play an essential role in cellular detoxification, making it possible for anaerobic organisms to survive exposure to small amounts of oxygen[1].

This chapter will focus on several aspects concerning not only the isolation of the different forms of this protein, but also its biochemical and spectroscopic properties.

The interaction with its proposed physiological electron donor, rubredoxin was also investigated and relevant results will be discussed in this chapter, focusing mainly on the design of a possible catalytic mechanism.

III.2 - Experimental

III.2.1 – *Dv* SOR, overexpression and isolation

Commercial competent *E. coli* cells (strain BL21(DE3), Invitrogen®) were transformed with the correspondent plasmid for the desired recombinant protein[2]. All the transformation procedures were carried out according to the manufacturer's recommendations (Appendix A). After the transformation process, the cells were plated in LB-Agar medium containing 0.1 mg/mL ampicillin and left to grow overnight at 37 ºC. Resulting colonies were used to start the overexpression of the desired proteins.

The overexpression procedure was as described in the literature with minor changes[2, 3]. Two steps of pre-cultures were performed prior to the main overexpression growth. The first step consisted in a 5 mL pre-culture in LB media containing 0.1 mg/mL ampicillin, that was grown overnight (from 10 to 12 hours) at 37 ºC at 225 rpm. The second step consisted in the addition of 1 mL of this grown medium to 100 mL LB media containing 0.1mg/mL ampicillin. This medium was left overnight (from 14 to 16 hours) at 37 ºC at 225 rpm. Finally, 5 mL of this culture were inoculated into 500mL (usually 4 L total, 8 x 500 mL) of LB media containing 0.1 mg/mL ampicillin and 0.1 mM $FeCl_2$. The cells were allowed to grow at 37 ºC at

230 rpm until its O.D. was near 0.8 at 600 nm. At this time 1 mM IPTG and 0.1 mM $FeCl_2$ were added and the culture was able to grow for approximately 14 hours at room temperature (between 20 and 25 ºC) at 230 rpm. All these growth procedures were performed aerobically.

After growth, cells were harvested by centrifugation at 10,000 x g for 8 min at 4 ºC. The supernatant was discarded and the cells were suspended in 50 mM Tris-HCl pH 7.6 buffer. A combination of freeze-thaw cycles (for 3 times, with liquid nitrogen and tepid water) and a French Press® (28,000 Psi) apparatus were used for cell disruption. During this process, a small amount of DNAse (purchased from Sigma) was added to ensure DNA degradation and, consequently, a cleaner sample. Cell disruption was followed by ultracentrifugation at 138,000 x g at 4 ºC for 1 h 30 min, in order to separate the fraction containing the desired protein from the rest.

After obtaining the fraction containing the recombinant SOR, three chromatographic steps were applied in order to isolate the protein. All purification steps were carried out at 4 ºC and at pH 7.6.

The first step consisted in loading the fraction into a XK26/40 column (2.6 x 40 cm, GE HealthCare®) filled with a DEAE-Sepharose FF® medium (GE HealthCare®), previously equilibrated with 50 mM Tris-HCl pH 7.6 buffer. After loading the column it was washed with two volumes of the equilibrating buffer in order to remove all the proteins that did not adsorbed to the matrix. An 800 mL gradient was applied (50 – 500 mM Tris-HCl pH 7.6) and the protein was collected between 250 – 300 mM.

After this chromatographic step three fractions were made according to the purity, as verified by UV-Visible spectra and SDS-PAGE electrophoresis (described in Appendix A). Two fractions contained the pink form of the protein and another contained a new “blue” form, which presented UV-Visible features resembling classes II and III SORs. All the three fractions were concentrated using a Diaflo® apparatus with an YM10 membrane.

In the second chromatographic step, the samples were loaded independently into a XK26/70 column packed with Superdex75® (Amersham Biosciences®), previously equilibrated with 300 mM Tris-HCl pH 7.6. Judging by the UV-Visible spectra and SDS-PAGE electrophoresis, it was clear that this second chromatographic step was not helpful to enhance the protein purification. The fractions were then concentrated as described before and the buffer was exchanged to 50 mM Tris-HCl pH 7.6 by successive addition.

A third chromatographic step was applied using another ionic exchange resin, Q-Sepharose FF® (GE HealthCare®) packed in a XK26/40 (2.6 x 40 cm). The procedure was similar to the one used in the first step, with the column being equilibrated with 50 mM Tris-HCl pH 7.6, washed with the same buffer and then applying a gradient from 50 – 1000 mM Tris-HCl pH 7.6 to remove the adsorbed proteins. As in the previous steps, the collected fractions were analyzed by UV-Visible and SDS-PAGE and divided according to their purity.

With this procedure it was possible to collect a final fraction containing the pure pink form of the SOR with a purity ratio of 6.2 (Abs_{280}/Abs_{490}), and another fraction containing the new “blue” form with a purity ratio of 21 (Abs_{280}/Abs_{644}).

The UV-Visible features of the blue protein raised a few questions about metal center composition, redox potential and catalytic activity. To characterize this new form and assess its functionality a series of biochemical and spectroscopic assays were devised.

III.2.2 – Biochemical and spectroscopic characterization of the new “blue” form of *Dv* SOR

As mentioned before, the UV-Visible features presented by this protein are very similar to those already known for class II and III SORs. The figure below represents a UV-Vis spectrum of the new “blue” form of *Dv* SOR.

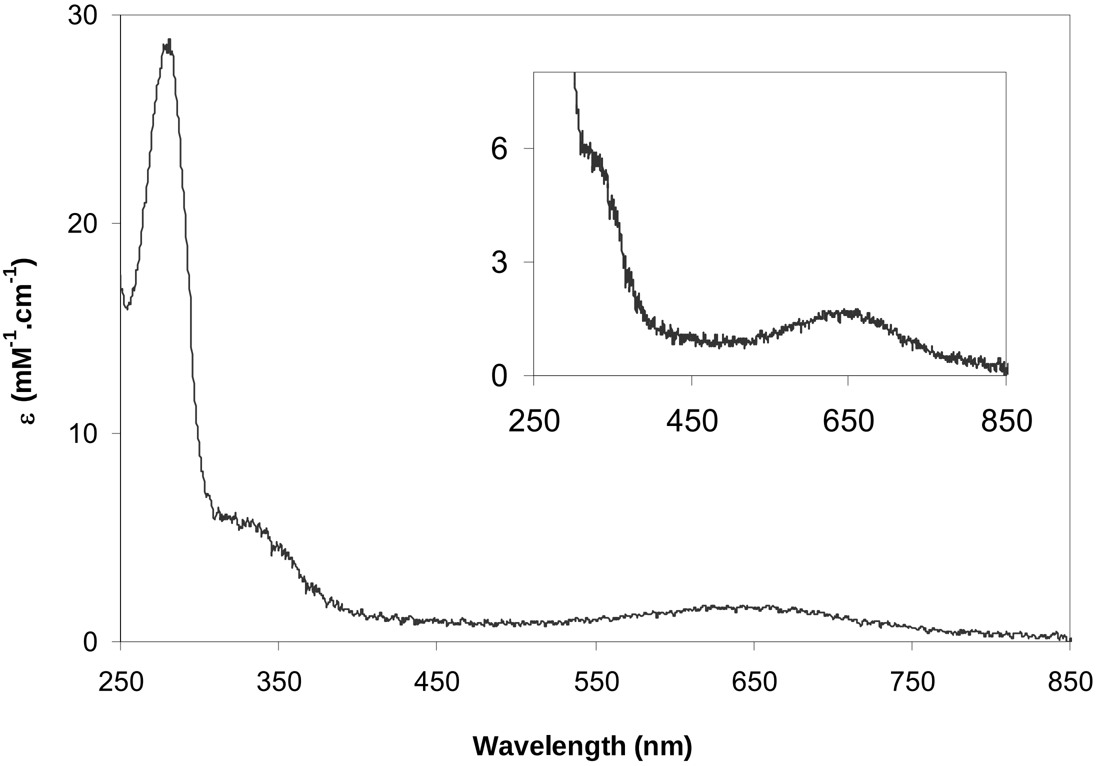

Figure III. 1 – Absorbance spectrum of the oxidized form of the new “blue” form of *Dv* SOR.

The absorption spectrum has three main features, at 280 nm (ε_{280} = 28650 M^{-1}.cm^{-1}), 314 nm (ε_{314} = 6089 M^{-1}.cm^{-1}) and 644 nm (ε_{644} = 1746 M^{-1}.cm^{-1}). The maximum at 644 nm is in accordance with the previously presented for the difference spectrum between the gray and the pink forms of *Dv* SOR and also for the DfxC (a modified *Dv* SOR which has the center II only)[2, 4, 5]. The shoulder around 314 nm should correspond to the cysteine-iron charge transfer band, also present in other proteins with similar iron centers like rubredoxin[2, 4-7].

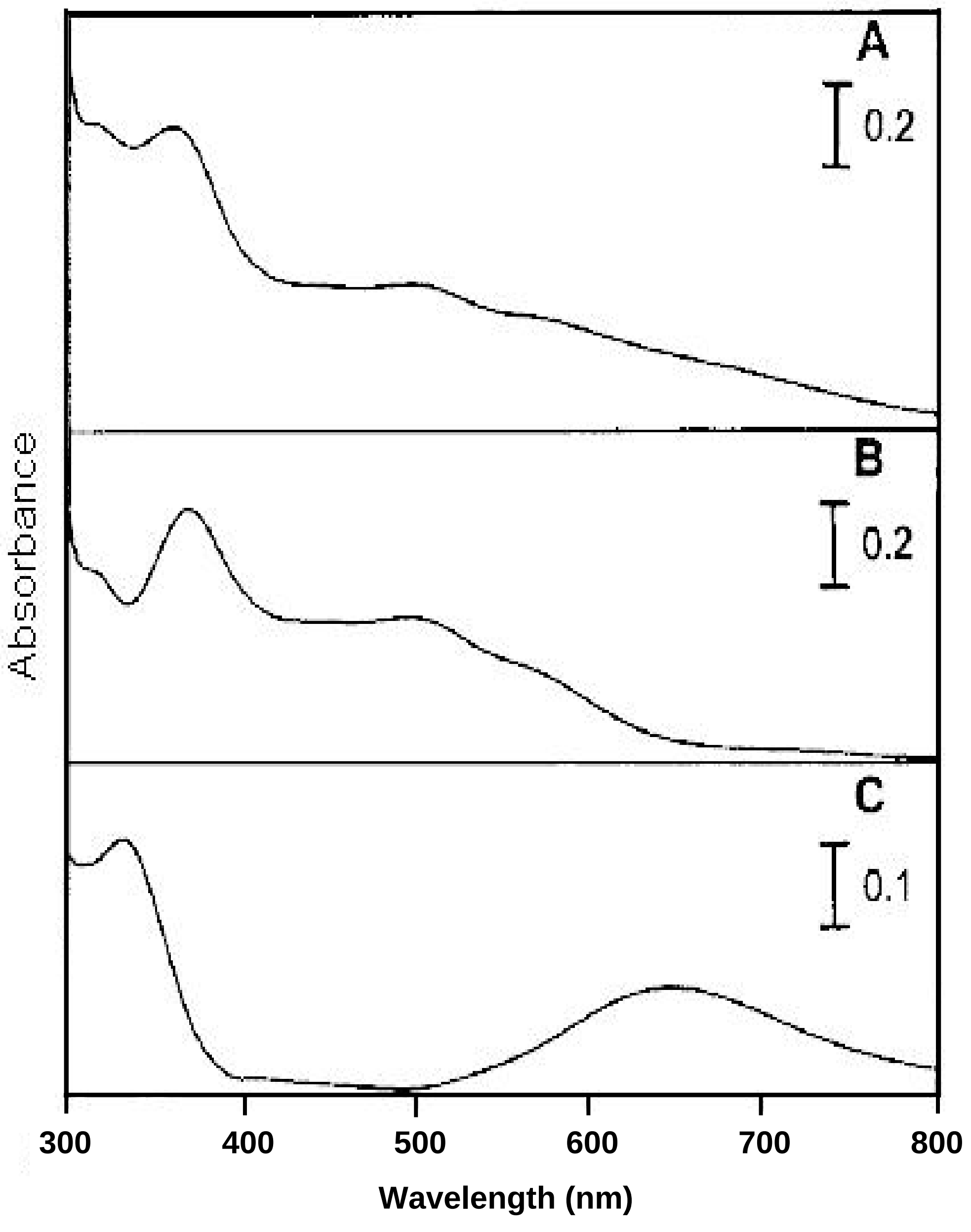

Figure III. 2 – UV-Vis spectra of both gray form (A) and pink form (B) of *Dv* SOR and a difference spectrum (C) between A and B showing the isolated center II. Adapted from Tavares and coworkers[4].

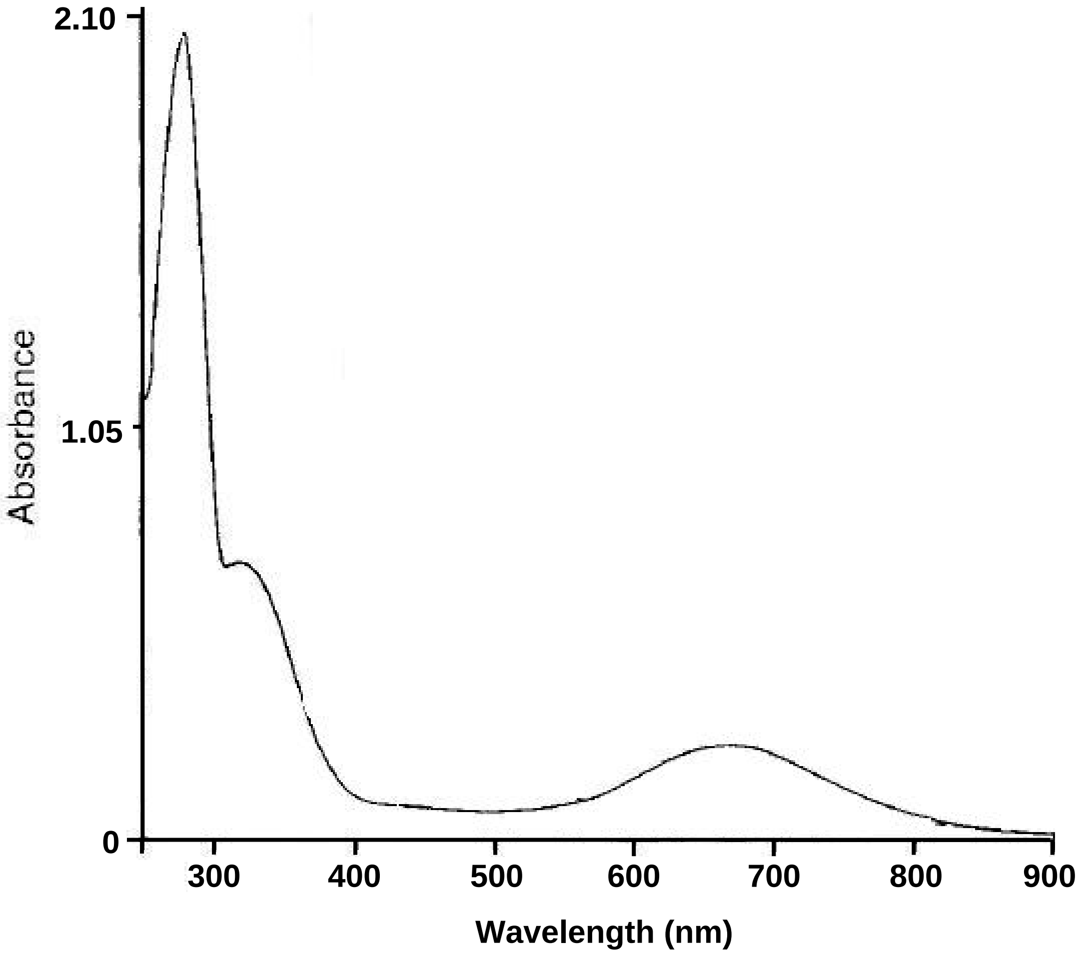

Figure III. 3 – UV-Vis spectrum of the oxidized form of *Desulfovibrio gigas* SOR. The protein concentration was 40 μM. Adapted from Chen and coworkers[8].

The protein was then subjected to sequential Edman degradation on an automatic protein sequencer (Applied Biosystem model LC491) and the NH_2-terminal sequence of the first 21 amino acid residues was determined. This analysis was made to ensure that the recombinant protein did not suffer an unexpected mutation/deletion that would remove some, or all, of the center I amino acid ligands. If this were to be the case, the UV-Visible spectrum could be explained by the absence of a metal ion in the center I.

The analysis indicated that the first 21 amino acids had 100% identity when compared to the sequence predicted by the gene analysis as shown below.

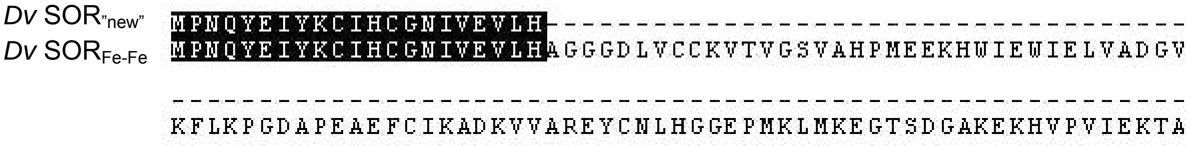

```
Dv SOR"new"   MPNQYEIYKCIHCGNIVEVLH------------------------------------
Dv SORFe-Fe   MPNQYEIYKCIHCGNIVEVLHAGGGDLVCCKVTVGSVAHPMEEKHWIEWIELVADGV

              ---------------------------------------------------------
              KFLKPGDAPEAEFCIKADKVVAREYCNLHGGEPMKLMKEGTSDGAKEKHVPVIEKTA
```

Figure III. 4 – Comparison between the NH_2-terminal sequence of the new "blue" form of Dv SOR and the deduced amino acid sequence predicted from the *Dv* SOR encoding gene.

The amount of iron per protein, as well as the screening of other metals in the protein, became essential to understand the spectroscopic behavior. To quantify the total amount of metal ions a sample was analyzed by induction-coupled plasma emission (Lab. de Análises, Dept. Química, CQFB/REQUIMTE, FCT/UNL) and the results are presented in table 1. The metal analysis performed doesn't reveal the presence of metal ions other than iron and zinc.

Table III. 1 – Plasma emission results obtained for the protein analysis

Sample	Metal (ppm)	
	Iron	Zinc
Protein	0.5793	2.1288
Control	-	0.7663

The obtained results show an iron concentration of 1.04 x 10^{-5} M and a zinc concentration of 2.08 x 10^{-5} M, which may indicate that the sample has a mixture of Zn-Fe and Zn-Zn forms. According to the theoretical ratio this mixture should have 66% of Zn/Fe and 33% of Zn-Zn. However, with the modifications applied to the overexpression method it was possible to obtain a pure Zn-Fe sample (see section III.2.3).

The metal analysis results, in conjunction with the obtained UV-Visible spectrum, point to the fact that the new "blue" form of the recombinant protein is an heterometallic form with a zinc replacing a iron ion in center I and a ferric ion in center II. In accordance, this form will be designated by $SOR_{Zn\text{-}Fe}$ from now on.

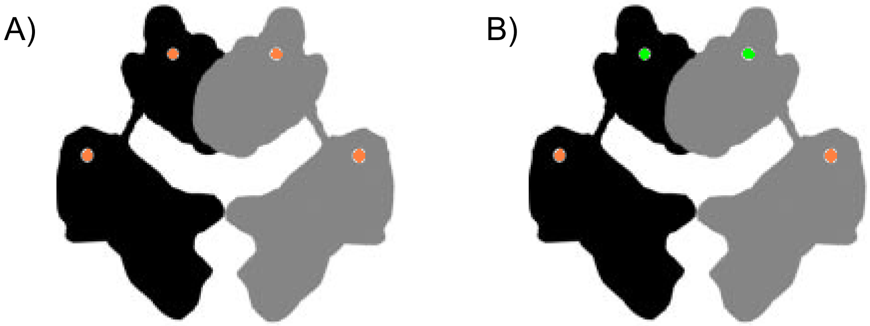

Figure III. 5 – Schematic representation of class I SOR. A) $SOR_{Fe\text{-}Fe}$, where the orange dots represent the iron atoms in both centers. B) $SOR_{Zn\text{-}Fe}$, where the green dots represent the zinc atoms in center I and orange dots represent the iron atoms in center II.

Further spectroscopic studies consisted in the characterization of $SOR_{Zn\text{-}Fe}$ by EPR in order to compare with the signals obtained for the iron only form, $SOR_{Fe\text{-}Fe}$. The next figure presents a plot of the obtained spectra.

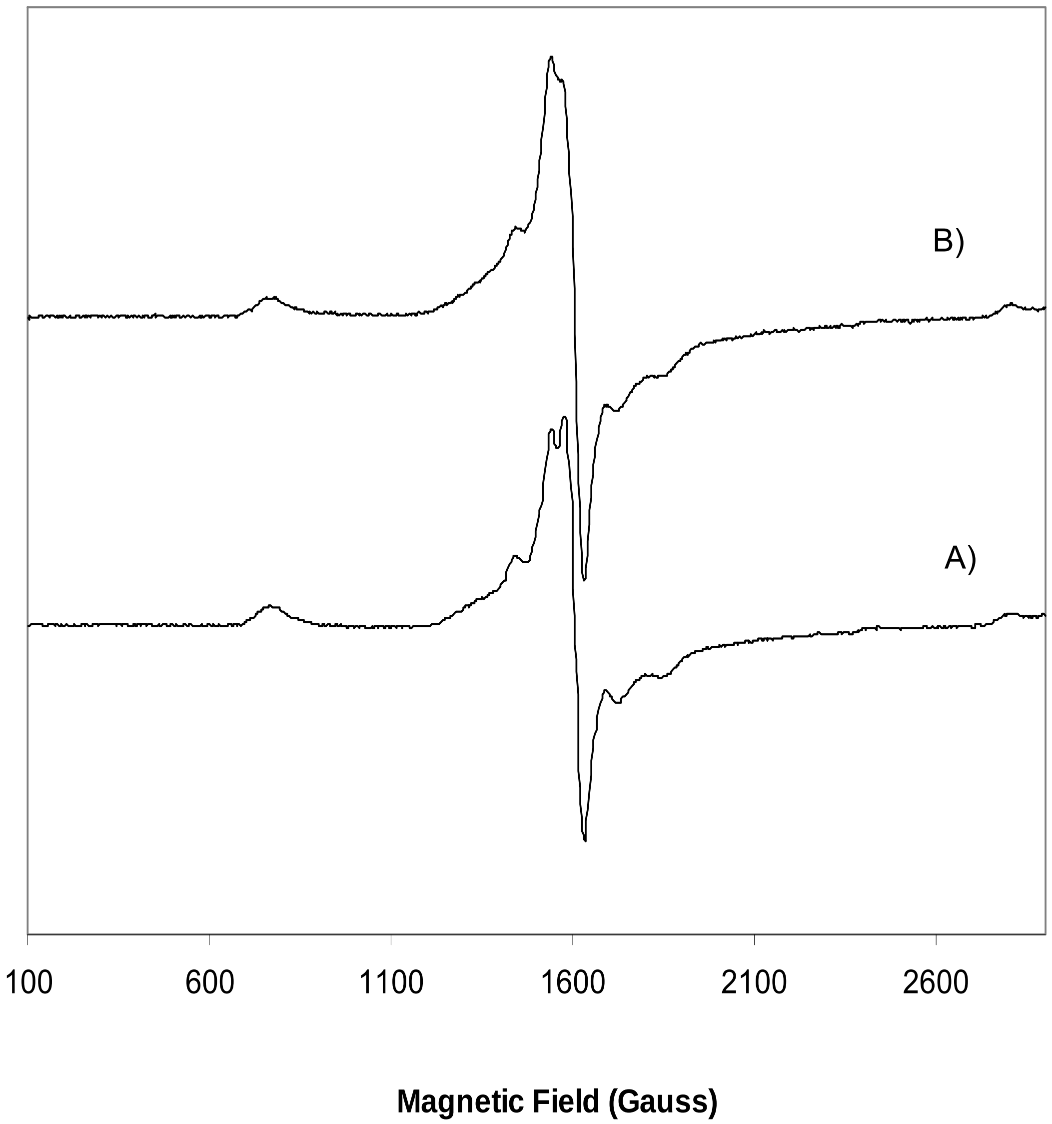

Figure III. 6 – EPR spectra of A) as purified $SOR_{Zn\text{-}Fe}$ and B) Oxidized $SOR_{Zn\text{-}Fe}$ (by incubation with sodium hexachloroiridate (IV)). The experimental conditions used were: temperature 4.1 K; microwave frequency 9.653 GHz; microwave power 2.002 mW; modulation amplitude 1 mT; receiver gain 1.26 x 10^5.

The EPR spectra of this $SOR_{Zn\text{-}Fe}$ revealed resonances at g = 8.93, g = 4.76 and g = 4.30, similar to the presented for the center II of $SOR_{Fe\text{-}Fe}$, which is indicative that the iron center should be structurally in the same environment[4, 6, 8].

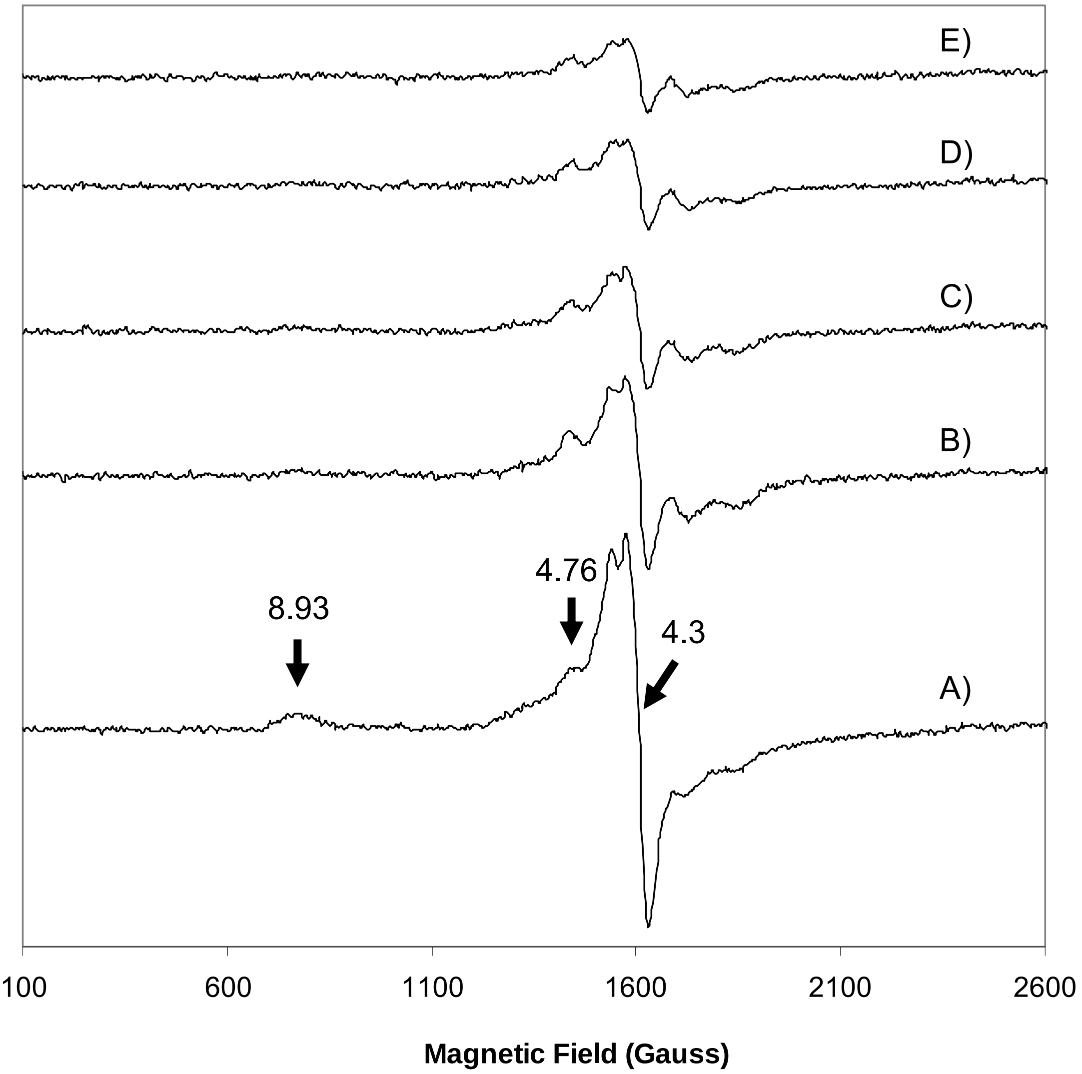

Figure III. 7 – Temperature dependence of EPR spectra of as-purified $SOR_{Zn\text{-}Fe}$. A) T = 4.2 K; B) T = 10 K; C) T = 15 K; D) T = 20 K; E) T = 25 K. Other conditions used were: microwave frequency 9.653 GHz; microwave power 2.002 mW; modulation amplitude 1 mT; receiver gain 1.26 x 10^5.

With all the spectroscopic and biochemical data pointing to a similar structure between $SOR_{Zn\text{-}Fe}$ and $SOR_{Fe\text{-}Fe}$, it seemed interesting to characterize not only the enzymatic function of this new form, but also its interaction with the proposed physiological electron donor, rubredoxin. However, for that kind of studies, a large amount of protein would be needed. To overcome that problem it became fundamental to improve the overexpression system in order to obtain a higher yield of recombinant $SOR_{Zn\text{-}Fe}$ protein. The next section will describe the approach used to accomplish this purpose.

III.2.3 – Overexpression of *Dv* $SOR_{Zn\text{-}Fe}$

One of the causes pointed for the appearance of $SOR_{Zn\text{-}Fe}$ form was the large amount of different metals in LB medium. Therefore, the production of more protein should not depend on a random distribution of metals in the overexpressed protein. The first approach to increase expression of the heterometallic form consisted in changing the growth medium to another that would allow the control of not only the relative concentrations but also the type of metal ions of interest. The chosen medium was M9 (described in Appendix A). It allowed the determination of the exact amount of metal desired for the correct overexpression of $SOR_{Zn\text{-}Fe}$.

The overall process was based in an already described method for the LB medium growth, with minor changes that proved to be more efficient during the several attempts to improve the process[2]. The overexpression procedure was exactly the same until the first pre-culture. The second pre-culture was done in M9 medium and consisted in the addition of 1 mL of the first pre-culture, made in LB medium, to 100 mL M9 medium containing 0.1 mg/mL ampicillin. The culture was left overnight at 37 ºC at 225 rpm. Then, 10 mL of this culture were inoculated into 1000 mL (usually 5L total, 5 x 1000 mL) of M9 medium containing 0.1 mg/mL ampicillin and 0.1 mM $FeCl_2$. The cells were allowed to grow at 37 ºC at 250 rpm until the culture O.D. was near 0.8 at 600 nm. At this time, 1 mM IPTG and 0.1 mM $FeCl_2$ and 0.1 mM $ZnCl_2$ were added and the culture was able to grow for approximately 14 hours at room temperature (between 20 and 25 ºC) at 250 rpm. Just like for LB medium, all these growth procedures were made aerobically.

From this point on, the isolation procedures were the same as described before, with the exception that in this case the second purification step (the molecular exclusion with Superdex75®, Amersham Biosciences®), was removed from the procedure and only two ionic exchange steps were performed.

This improved overexpression and isolation procedure was also applied for the expression of the $SOR_{Fe\text{-}Fe}$ form of the protein. With this process the initial batch, after the ultracentrifugation step, was much cleaner, with fewer amounts of other undesired proteins.

III.2.4 – Direct electron transfer between recombinant SOR forms and rubredoxin from *Desulfovibrio vulgaris* Hildenborough

The first chapter of this thesis pointed out some unanswered questions regarding the enzymatic activity of SORs and their mechanism. One of the questions is based on SOR ability to receive electrons from its proposed physiological partner, rubredoxin. Until now several studies presented kinetic information for the direct electron transfer[3, 9-12].

However, all the approaches took into account only the electron transfer but the relevance of the presence, or not, of center I remained always unclear[3, 9, 11]. Even when Kurtz and coworkers modified the *D. vulgaris* SOR obtaining a mutant protein, C13S SOR, in which one ligand residue of the [Fe(SCys)4] site, cysteine 13, was changed to serine, it was not possible to clearly state what would be the function of center I[12].

The isolation of $SOR_{Zn\text{-}Fe}$ represents a step forward to answer these questions. In this protein both centers are present but center I possesses a "silent", i.e. non-redox active, zinc ion. No mutations are present and the structure of the entire protein should be exactly the same as the $SOR_{Fe\text{-}Fe}$. All these features were fundamental for the validation of the results and make a difference when compared to the other similar works.

In this work, several pairs of electron donor/acceptor were studied in order to build up a complete scheme for electron transfer and catalysis. The final purpose is to assign the physiological relevance of both center I and II.

To evaluate the direct electron transfer rate constant a stopped-flow experiment was designed. The objective was to follow not only the oxidation of rubredoxin but also the reduction of center II, for the case of gray form of $SOR_{Fe\text{-}Fe}$ and $SOR_{Zn\text{-}Fe}$. These experiments were performed in anaerobic conditions, inside a glove box (UniLab from mBraun, less than 1 ppm of oxygen), and should describe directly the electron transfer between the two proteins. All the assays were performed in 50 mM Phosphate buffer at pH 7.6 with 0.1 mM EDTA.

The main experiment consisted in a 1:1 mixture between reduced rubredoxin and oxidized SOR. As they had the same initial concentration, a second order kinetic law was applied to obtain a second order constant, correspondent to the electron transfer. A second experiment consisted in mixing different concentrations of SOR with the same amount of rubredoxin. The main objective was to relate the amount of oxidized rubredoxin with SOR added. With this experiment it was also possible to establish the reaction stoichiometry.

To perform the experiments both rubredoxin and SOR were degassed in a Schlenk line before being introduced inside the glove box. Rubredoxin was then reduced with a slight excess of sodium dithionite and SOR was prepared according to the desired protein form. The pink form was obtained by incubating SOR with a slight excess of ascorbic acid. The gray and “Zn-Fe” forms were prepared with an excess of sodium hexachloroiridate (IV) (purchased from Aldrich®) in order to obtain the fully oxidized form. All the samples were desalted, prior to use, in a 5 mL Hitrap™ desalting column (GE Healthcare®).

The obtained data was best fitted with a second order rate constant (Eq. III.1), with $[Rd]_0 = [SOR]_0$ and where $[Rd_{ox}]$ is the amount of oxidized rubredoxin, $[Rd]_0$ and $[SOR]_0$ are the initial concentrations of reduced rubredoxin and oxidized SOR respectively and $k' = k \times [Rd_{red}]_0$, where *k* is the second order rate constant.[9, 13]

$$[Rd_{ox}] = [Rd_{red}]_0 - \frac{[Rd_{red}]_0}{1 + \kappa' \times t} \qquad \text{Eq.III.1}$$

The rate constant calculations were performed based on, at least, three replicates of each assay.

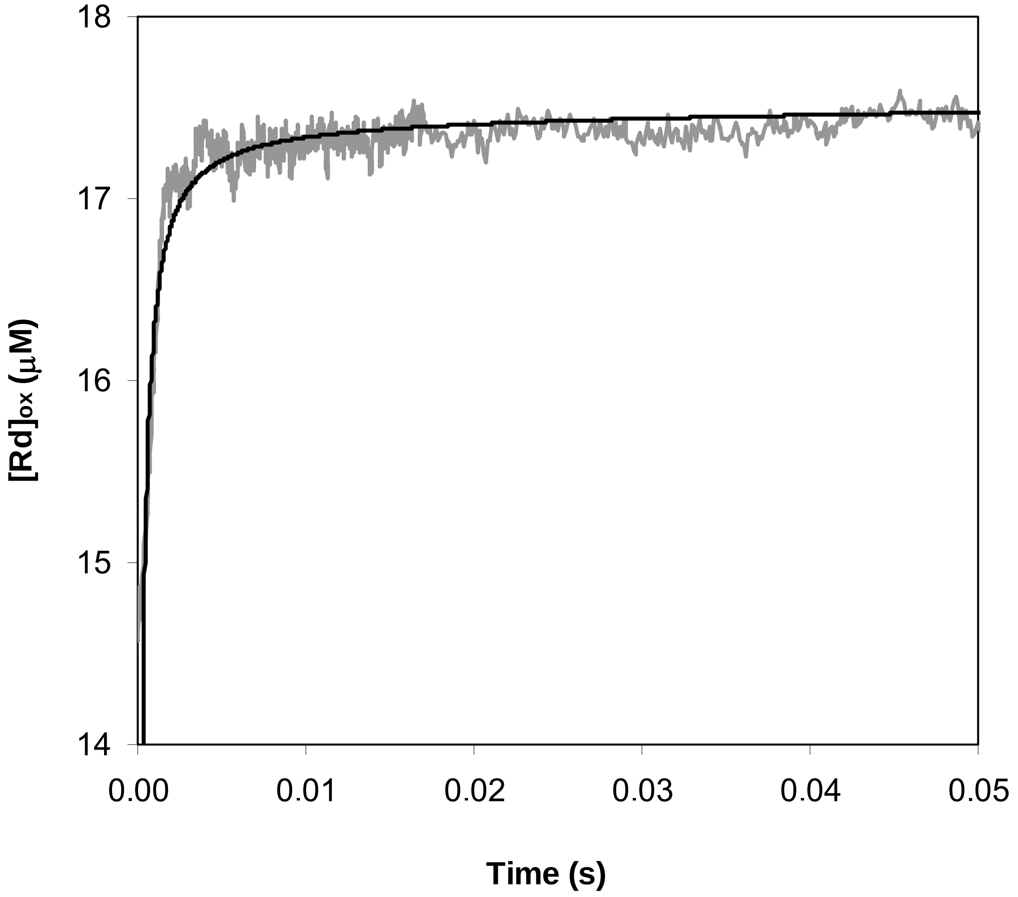

Figure III. 8 - Stopped-flow kinetics of the oxidation of reduced rubredoxin by the pink form of $SOR_{Fe\text{-}Fe}$. The variation was measured by the absorbance changes at 500 nm and converted to concentration. The gray line represents the experimental data and the black line represents the theoretical fit. Solutions of 50 μM reduced rubredoxin were mixed (1:1) (v/v) with 50 μM oxidized SOR at 10 ºC.

The data analysis for all the replicates of the pink form of SOR_{Fe-Fe} revealed a second order rate constant of (2.8 ± 0.4) x 10^7 $M^{-1}.s^{-1}$, which corresponds to the electron transfer rate from rubredoxin to the center I.

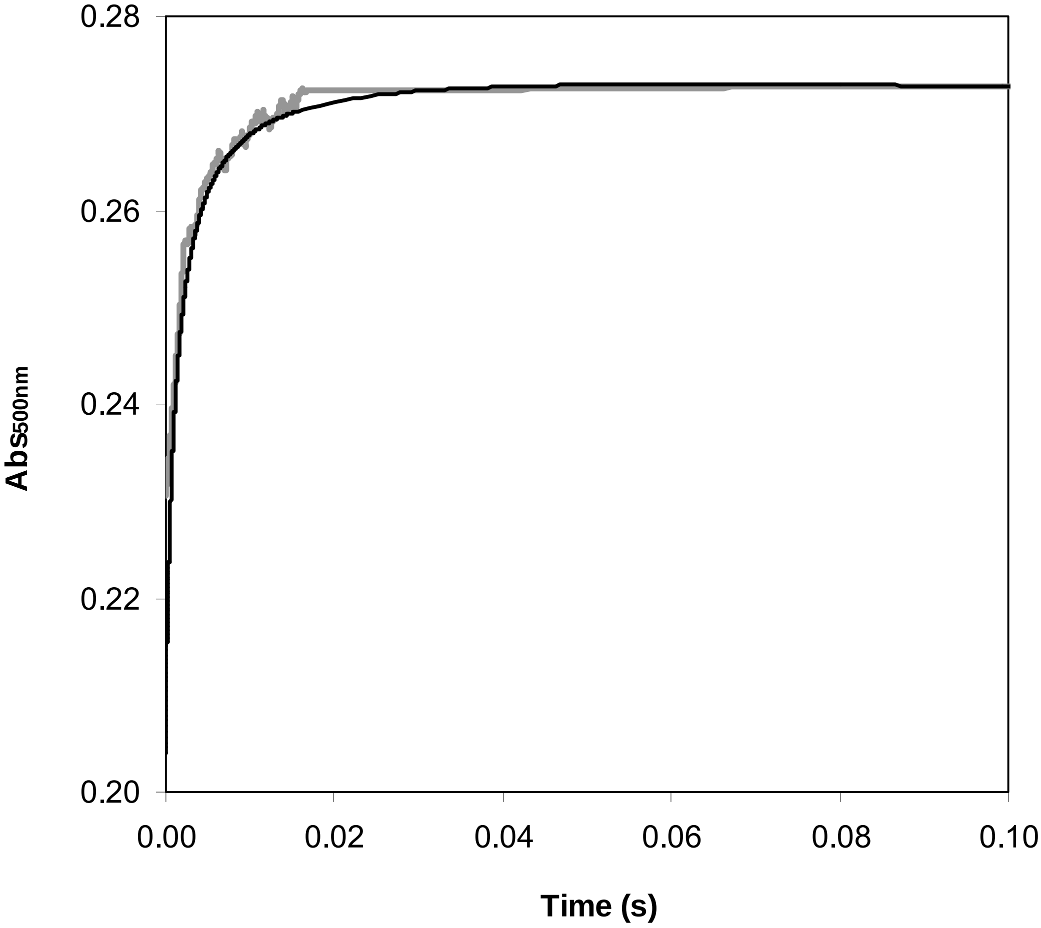

Figure III. 9 - Stopped-flow kinetics of the oxidation of reduced rubredoxin by the gray form of SOR_{Fe-Fe}. The variation was measured by the absorbance changes at 500 nm. The gray line represents the experimental data and the black line represents the theoretical fit. Solutions of 50 μM reduced rubredoxin were mixed (1:1) (v/v) with 50 μM oxidized SOR at 10 ºC.

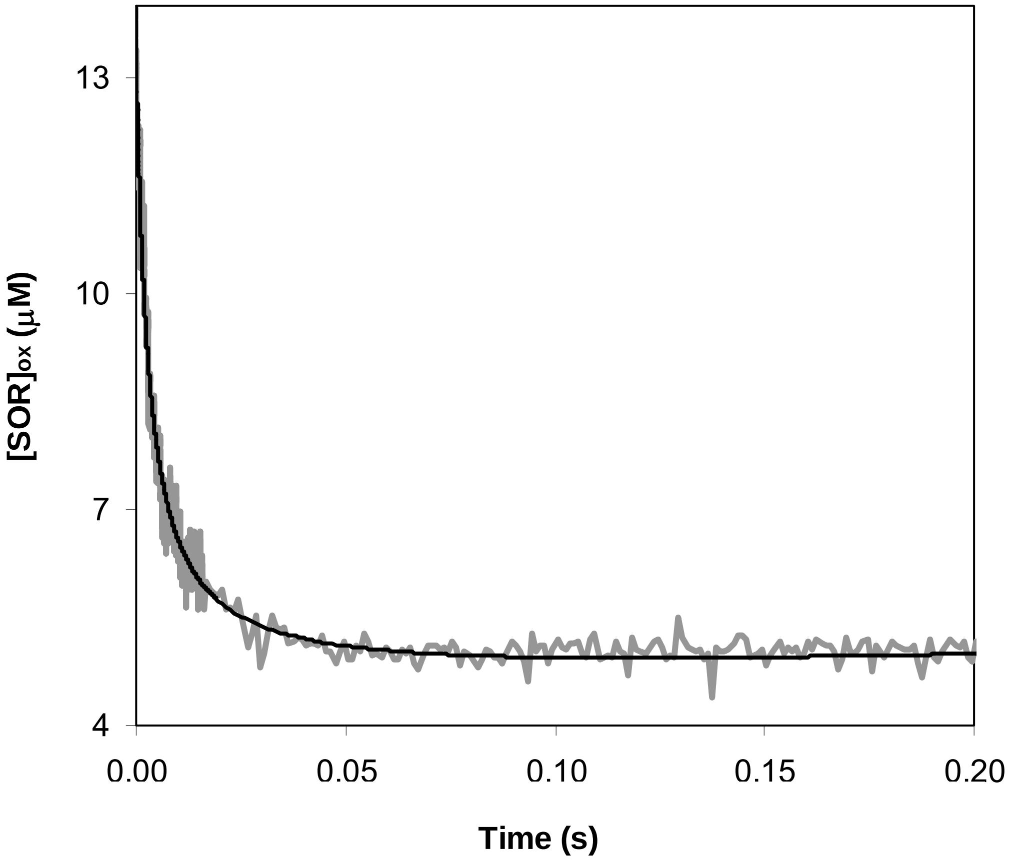

Figure III. 10 - Stopped-flow kinetics of the reduction of gray form $SOR_{Fe\text{-}Fe}$ by reduced rubredoxin. The variation was measured by the absorbance changes at 650 nm and converted to concentration. The gray line represents the experimental data and the black line represents the theoretical fit. Solutions of 50 μM of reduced rubredoxin were mixed (1:1) (v/v) with 50 μM of oxidized SOR at 10ºC.

The electron transfer to the gray form, analyzed at both 500 nm and 650 nm, near the maxima of rubredoxin and $SOR_{Fe\text{-}Fe}$ center II, respectively, should give some information about the pathway of the electron transfer between the two proteins. The values obtained for both wavelengths were $(4.3 \pm 1.9) \times 10^{6}$ $M^{-1}.s^{-1}$ and 1.9×10^{6} $M^{-1}.s^{-1}$, for 500 nm and 650 nm respectively. These values are considered identical within the experimental error.

From the presented data it becomes clear that the observed absorbance value at 500 nm does not correspond to the total oxidized rubredoxin, but to a sum of total amount of oxidized rubredoxin and the pink form of SOR_{Fe-Fe}. This observation raised the question about the exact location where electron transfer occurs or even if there is some sort of intramolecular electron transfer. To further understand the electron transfer process, a similar experiment was performed but with a 2:1 proportion between the two proteins.

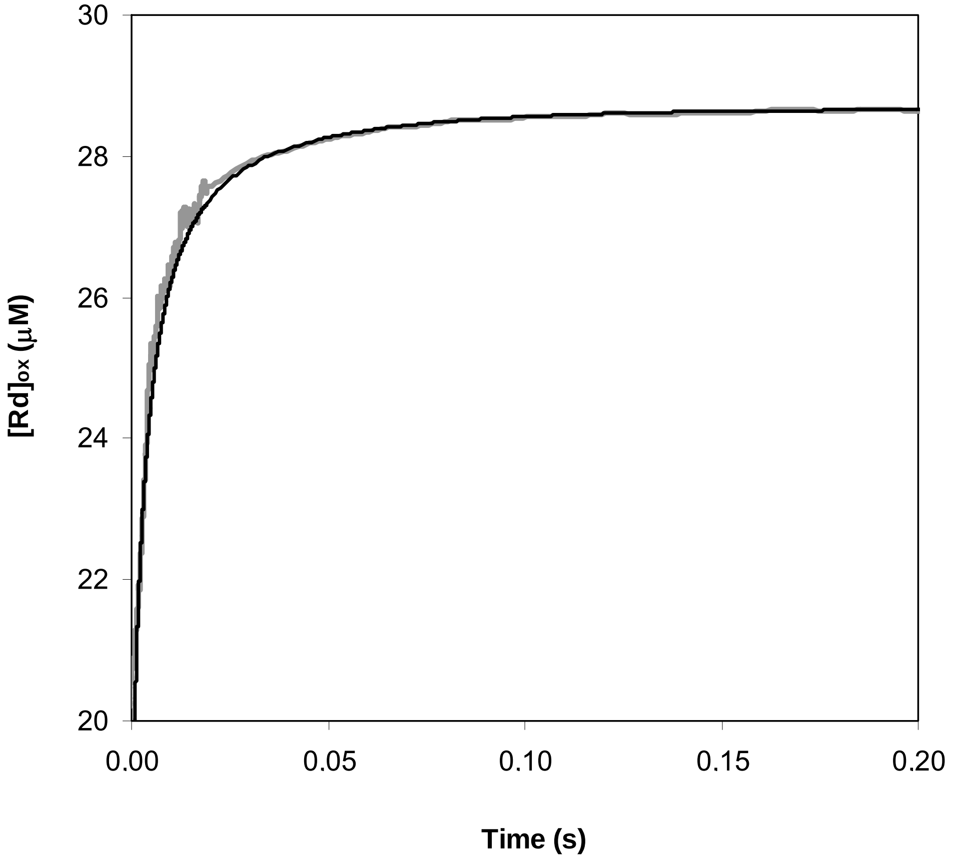

Figure III. 11 - Stopped-flow kinetics of the reduction of gray form SOR_{Fe-Fe} by reduced rubredoxin. The variation was measured by the absorbance changes at 500 nm and converted to concentration. The gray line represents the experimental data and the black line represents the theoretical fit. Solutions of 50 μM reduced rubredoxin were mixed (2:1) (v/v) with 50 μM oxidized SOR at 10 ºC.

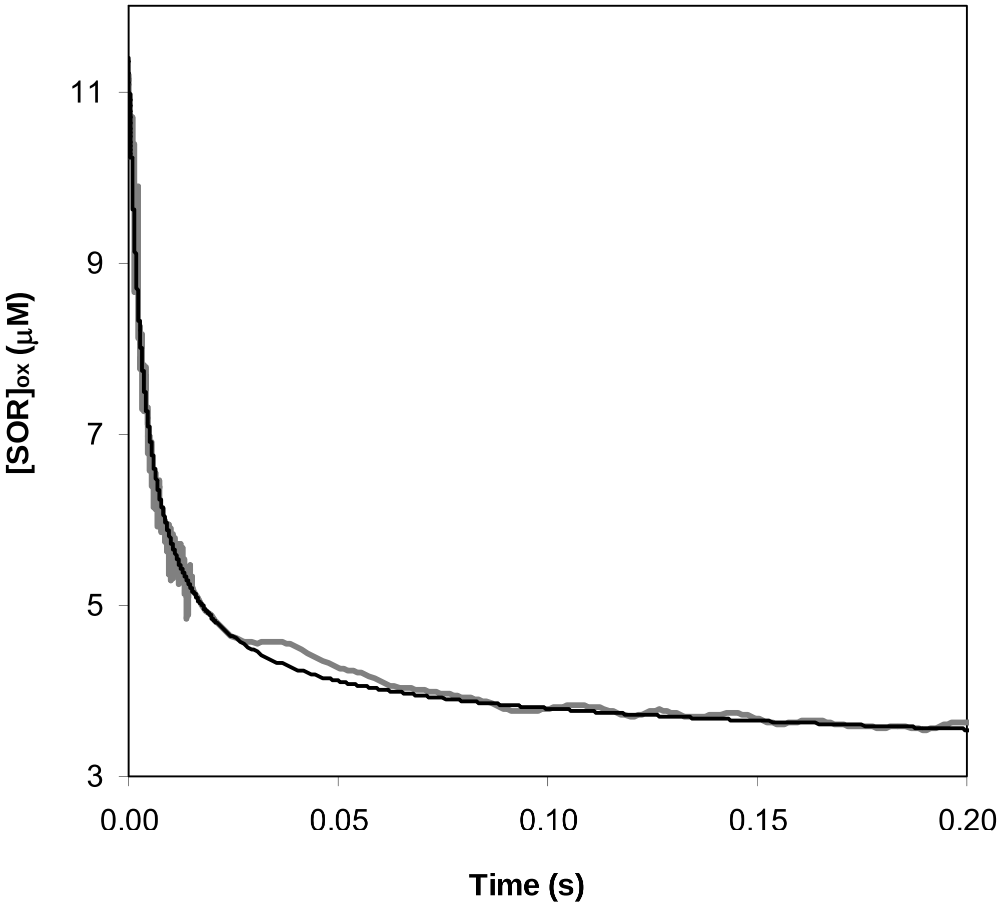

Figure III. 12 - Stopped-flow kinetics of the reduction of gray form $SOR_{Fe\text{-}Fe}$ by reduced rubredoxin. The variation was measured by the absorbance changes at 650 nm and converted to concentration. The gray line represents the experimental data and the black line represents the theoretical fit. Solutions of 50 μM reduced rubredoxin were mixed (2:1) (v/v) with 50 μM oxidized SOR at 10 ºC.

From the collected data the calculated values for both wavelengths were (1.3 ± 0.2) x 10^6 $M^{-1}.s^{-}1$ and (1.7 ± 0.3) x 10^6 $M^{-1}.s^{-1}$, for 500 nm and 650 nm respectively. Once again, these values are considered identical within the experimental error.

In this case, the values obtained for the amount of oxidized rubredoxin are in agreement with the expected, meaning that all the rubredoxin was oxidized and all the SOR was converted to the reduced form. The significance of the obtained values will be discussed later on.

Finally, the experiments were repeated with the oxidized SOR_{Zn-Fe} in order to try to find differences between this form and the SOR_{Fe-Fe}.

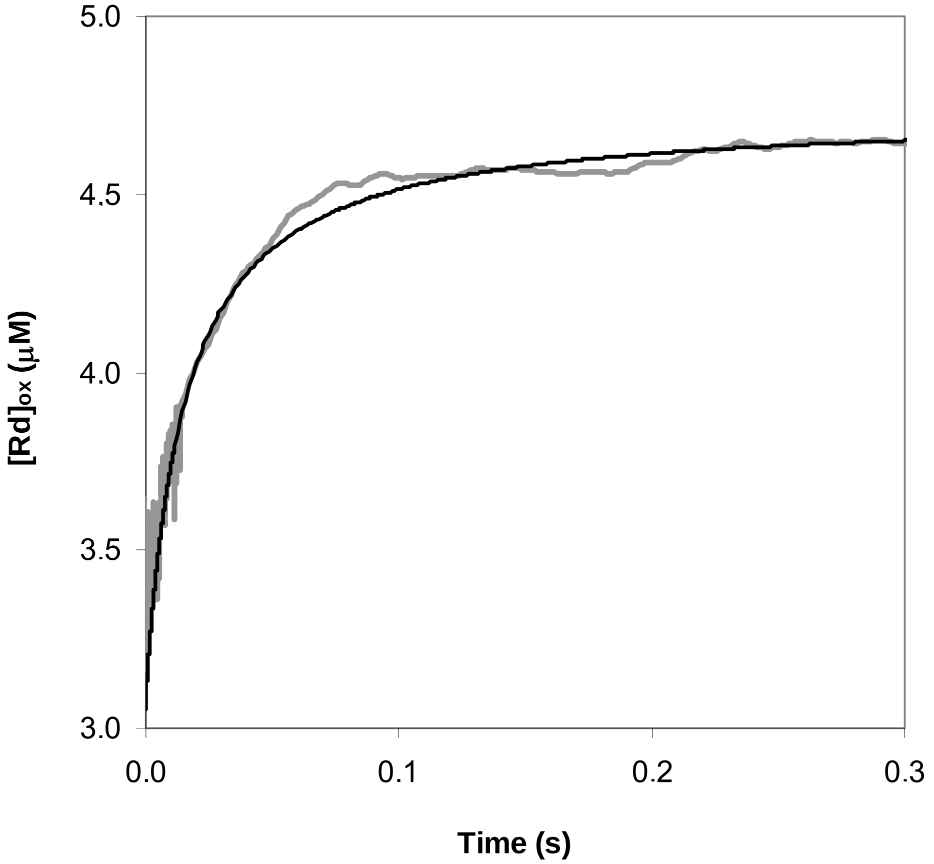

Figure III. 13 – Stopped-flow kinetics of the oxidation of reduced rubredoxin by oxidized SOR_{Zn-Fe}. The variation was measured by the absorbance changes at 500 nm and converted to concentration. The gray line represents the experimental data and the black line represents the theoretical fit. Solutions of 12 μM reduced rubredoxin were mixed (1:1) (v/v) with 12 μM oxidized SOR at 10ºC.

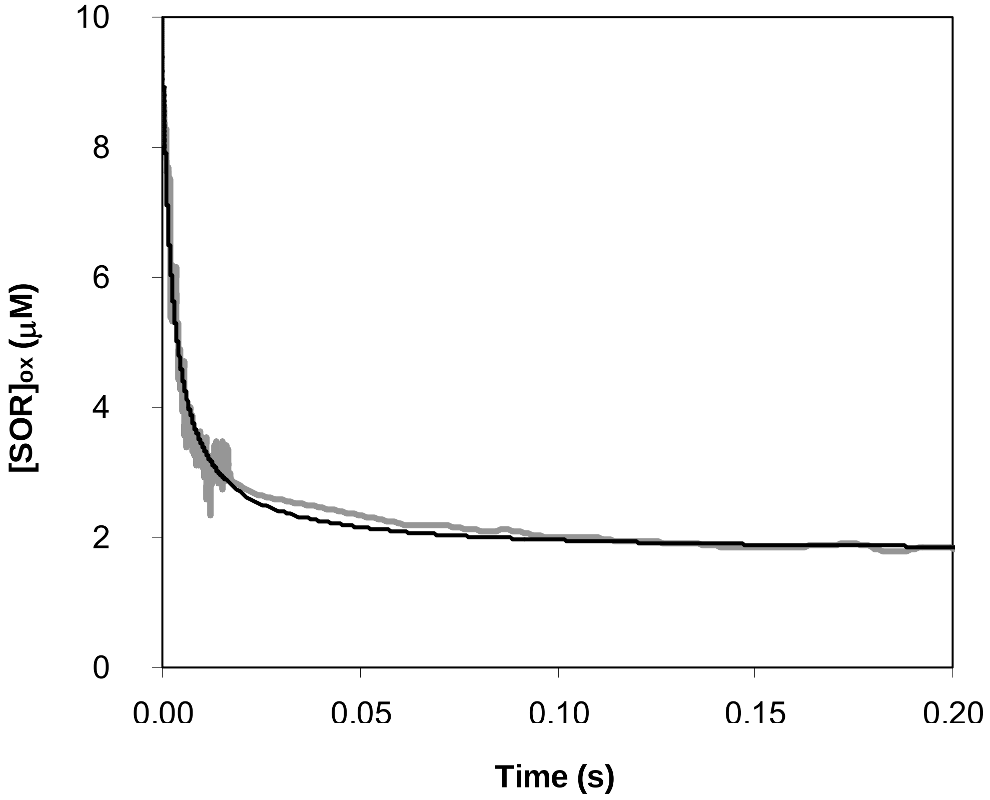

Figure III. 14 - Stopped-flow kinetics of the reduction of oxidized $SOR_{Zn\text{-}Fe}$ by reduced rubredoxin. The variation was measured by the absorbance changes at 650 nm and converted to concentration. The gray line represents the experimental data and the black line represents the theoretical fit. Solutions of 25 μM reduced rubredoxin were mixed (1:1) (v/v) with 25 μM oxidized SOR at 10ºC.

In this case, the calculated values for both wavelengths were (3.2 ± 1.5) x 10^6 $M^{-1}.s^{-}1$ and (2.9 ± 0.4) x 10^6 $M^{-1}.s^{-1}$, for 500 nm and 650 nm respectively. Again, these values can be considered similar within the experimental error. They are also similar to the ones obtained for the gray form of the SOR. To demonstrate this similarity, the comparison between oxidized $SOR_{Zn\text{-}Fe}$ and gray SOR reactions is presented in figure III.15.

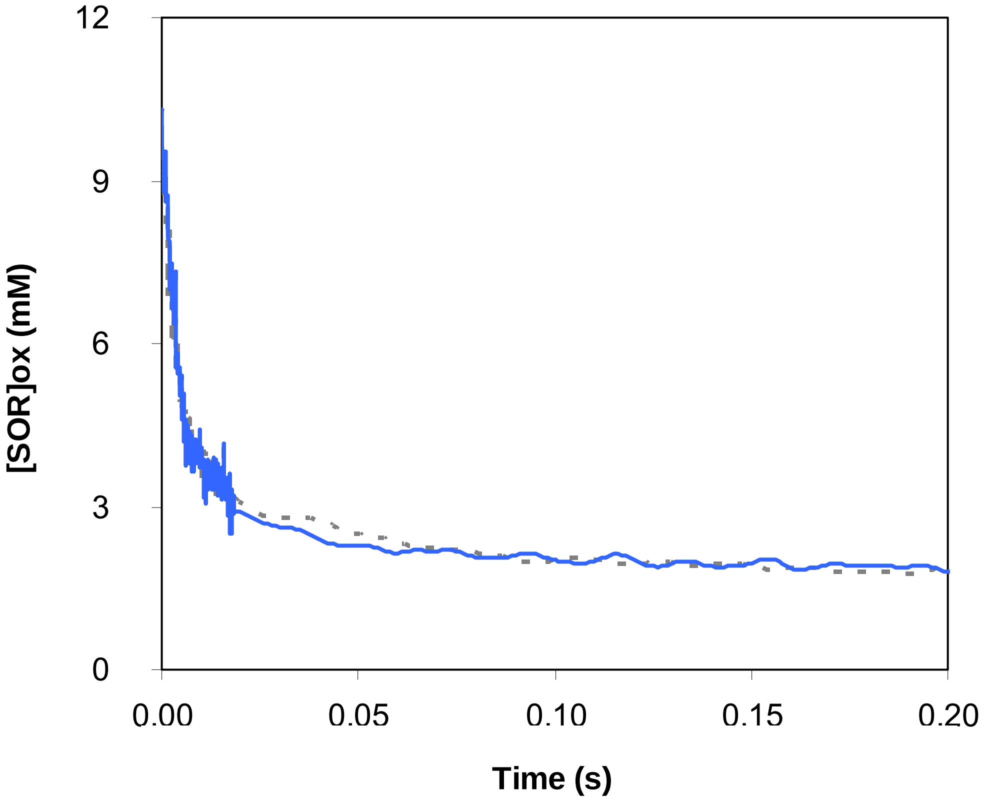

Figure III. 15 - Comparison of stopped-flow kinetics of the reduction of oxidized $SOR_{Zn\text{-}Fe}$ by reduced rubredoxin (A) and oxidized gray form of $SOR_{Fe\text{-}Fe}$ by reduced rubredoxin (B). The variation was measured by the absorbance changes at 650 nm and converted to concentration.

As expected, rubredoxin was able to reduce all the SOR forms. However, the electron transfer rate constants are different for the different forms. In the table below, a summary of all the obtained values are presented.

Table III. 2 – Second order rate constants of electron transfer between reduced rubredoxin and SORs

Wavelength (nm)	Second order rate constant ($M^{-1}.s^{-1}$)			
	Pink	Gray (1:1)	Gray (2:1)	SOR_{Zn-Fe}
500	(2.8±0.4) x 10^7	(4.3±1.9) x 10^6	(1.3±0.2) x 10^6	(3.2±1.5) x 10^6
650	-	1.9 x 10^6	(1.7±0.3) x 10^6	(2.9±0.4) x 10^6

The values presented in table III.2 clearly show that the electron transfer is much faster (by one order of magnitude) to the pink form of SOR_{Fe-Fe} than to the other forms. Previous studies always pointed for the existence of an electron transfer to all previously known forms, even for the *Dv* C13S mutant, but none had reported such a difference in the calculated rate constants[9, 12, 13].

This difference itself could be related not only to the mechanism of the enzyme itself but also to some possible structure modification between the pink and gray forms.

Another interesting feature was seen in the second set of experiments, when different SOR concentrations were mixed with a fixed amount of reduced rubredoxin. This data not only raises the interest for the biological need of the center I, but also points to new questions regarding the existence of different oxidation states of SOR in the cell. This experiment showed, as expected, that the amount of oxidized rubredoxin was SOR dependent[10]. From the slope of each trend line in figure III.16 it is possible to calculate the stoichiometry of this electron transfer. Table III.3 summarizes the obtained values.

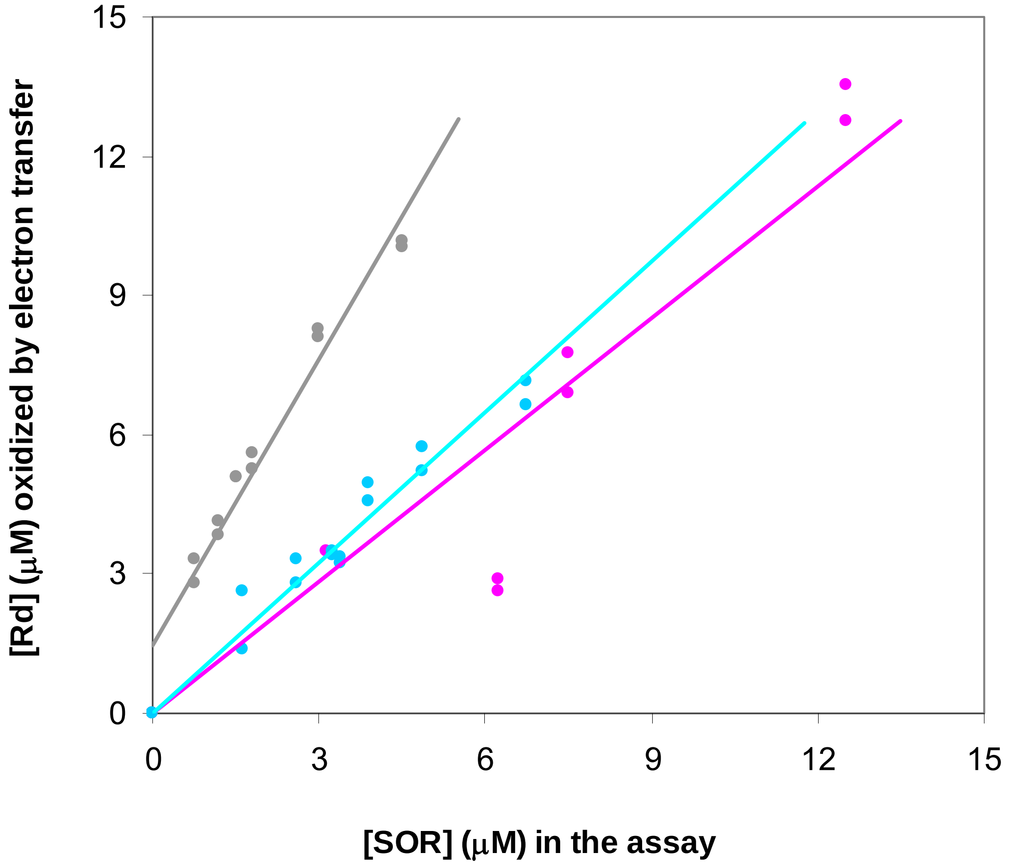

Figure III. 16 – Rubredoxin oxidized by direct electron transfer to different amounts of SOR. The experimental data are represented in gray dots for the gray form of $SOR_{Fe\text{-}Fe}$; in pink for the pink form of $SOR_{Fe\text{-}Fe}$ and in blue for the oxidized form of $SOR_{Zn\text{-}Fe}$; the trend lines are the best fits for the experimental data.

Table III. 3 – Calculated stoichiometry for each rubredoxin/SOR pair

	SOR protein		
	Pink	Gray	$SOR_{Zn\text{-}Fe}$
Stoichiometry	0.94 ± 0.13	2.06 ± 0.09	1.08 ± 0.06

The stoichiometry obtained for both pink and Zn-Fe forms of SOR corresponds to the theoretical prediction since it means that for every oxidized rubredoxin molecule there is one reduced SOR molecule. The same theory is applied for the gray form, but since in this case SOR has two oxidized iron centers, the stoichiometry obtained was two. However, the values obtained for this form are higher than the expected. This could be due to the contribution of the pink form (due to one-electron reduction of gray form) which has absorption maxima similar to rubredoxin, leading to a deconvolution error that results in the over estimation of the oxidized rubredoxin concentration. Such a fact is in accordance with the stopped-flow results, where it could be seen that a mixture of pink form and oxidized rubredoxin is achieved for 1:1 protein ratios.

III.2.5 – Superoxide Reductase Activity

The previous experiments proved that the electron transfer between rubredoxin and $SOR_{Zn\text{-}Fe}$ is possible. However, there is still a need to evaluate the ability to catalyze superoxide anion reduction and compare it with the $SOR_{Fe\text{-}Fe}$ form.

In order to calculate the superoxide reductase activity, an experimental procedure was established based on a previously reported assay[3]. It consisted in the reduction of superoxide anion by catalytic amounts of SOR. Reduced rubredoxin is used as electron donor, and its oxidation is also used to calculate the reaction rate. The next figure illustrates one typical assay.

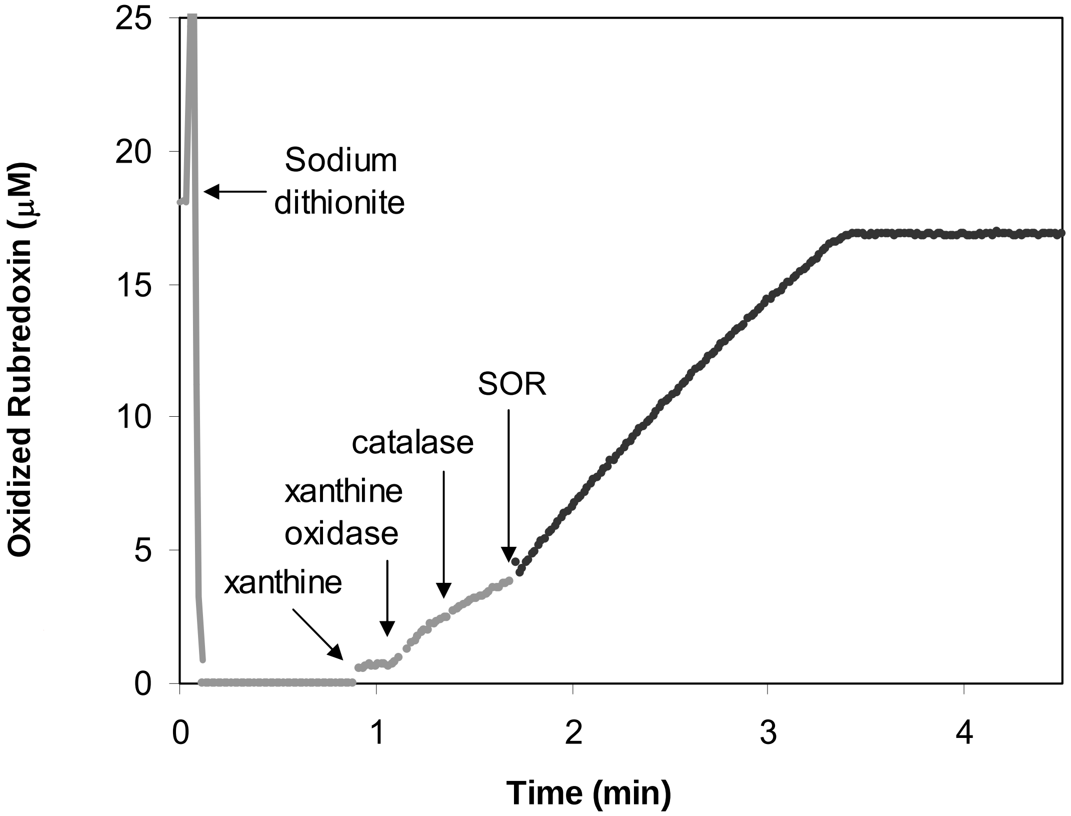

Figure III. 17 – Illustration of superoxide-mediated electron transfer assay. Rubredoxin concentration was 15 μM and the SOR concentration ranged from 10 nM to 1 μM. All the assays were performed in 50 mM phosphate buffer pH 7.6 with 0.1 mM EDTA at 23 ºC. Sodium dithionite was used to perform the initial stoichiometric reduction of rubredoxin.

The reagents were always added in the same order and within the same time scale in order to keep the same experimental conditions. The rubredoxin was added to the assay in the oxidized form and reduced with sodium dithionite. The amount of sodium dithionite added was calibrated to ensure that there was no excess and at the same time, all the rubredoxin was reduced and ready to react. The amounts of xanthine (1.5 mM) and xanthine oxidase (0.058 U/mL) were such as to ensure a constant flux of superoxide during the reaction (ca. 14 $\mu M.min^{-1}$). The use of catalase (150 U/mL) was necessary to remove the hydrogen peroxide formed by spontaneous superoxide dismutation, xanthine/xanthine oxidase system (also a reaction product) and superoxide reduction (with SOR), in order to prevent any inhibition by product[14-16].

All the data was fitted assuming that the reaction rate was proportional to the concentration of the reagents and a kinetic constant k. In order to facilitate the calculation, the concentration of both rubredoxin and superoxide used were significantly bigger than SOR and so, considered constant at t = 0. The obtained equation was as follows:

$$v = k' [SOR] \qquad \text{Eq. III.2}$$

Were k' is

$$k' = k [Rd] [O_2^{\cdot-}] \qquad \text{Eq. III.3}$$

The value for v_0 was obtained directly from the experimental data and plotted against the correspondent amount of SOR. The results are presented in the following figures.

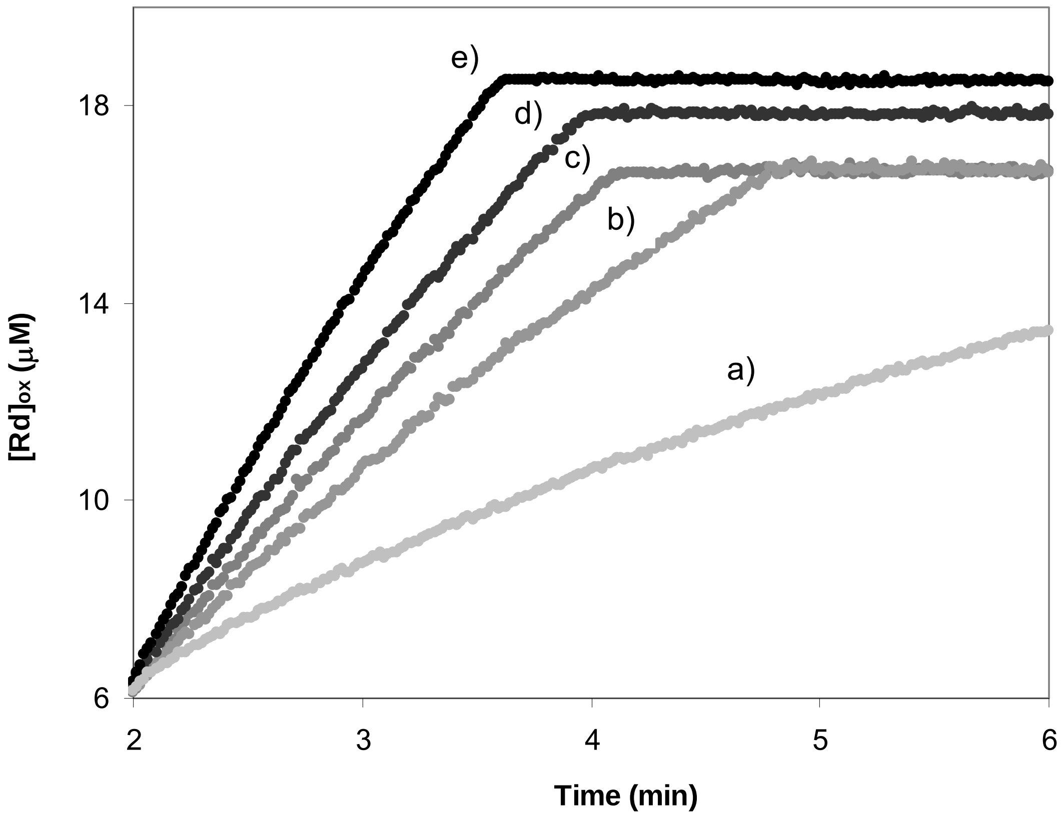

Figure III. 18 – Kinetic traces of superoxide-mediated electron transfer between rubredoxin and the pink form of SOR_{Fe-Fe}. The different traces represent different amounts of SOR added, a) 0 μM; b) 0.04 μM; c) 0.08 μM; d) 0.2 μM and e) 0.4 μM. The assays were performed in 50 mM phosphate buffer pH 7.6 with 0.1 mM EDTA at 23 ºC.

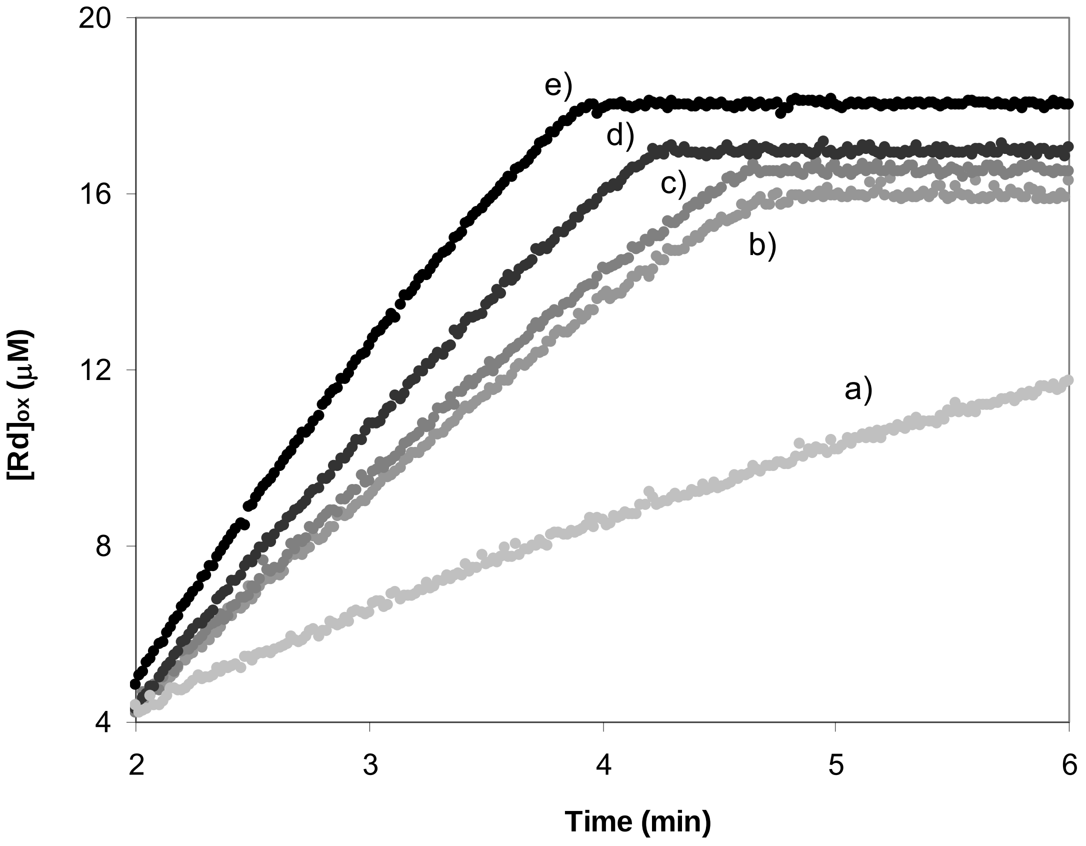

Figure III. 19 - Kinetic traces of superoxide-mediated electron transfer between rubredoxin and the gray form of $SOR_{Fe\text{-}Fe}$. The different traces represent different amounts of SOR added, a) 0 μM; b) 0.08 μM; c) 0.2 μM; d) 0.4 μM and e) 1 μM. The assays were performed in 50 mM phosphate buffer pH 7.6 with 0.1 mM EDTA at 23 ºC.

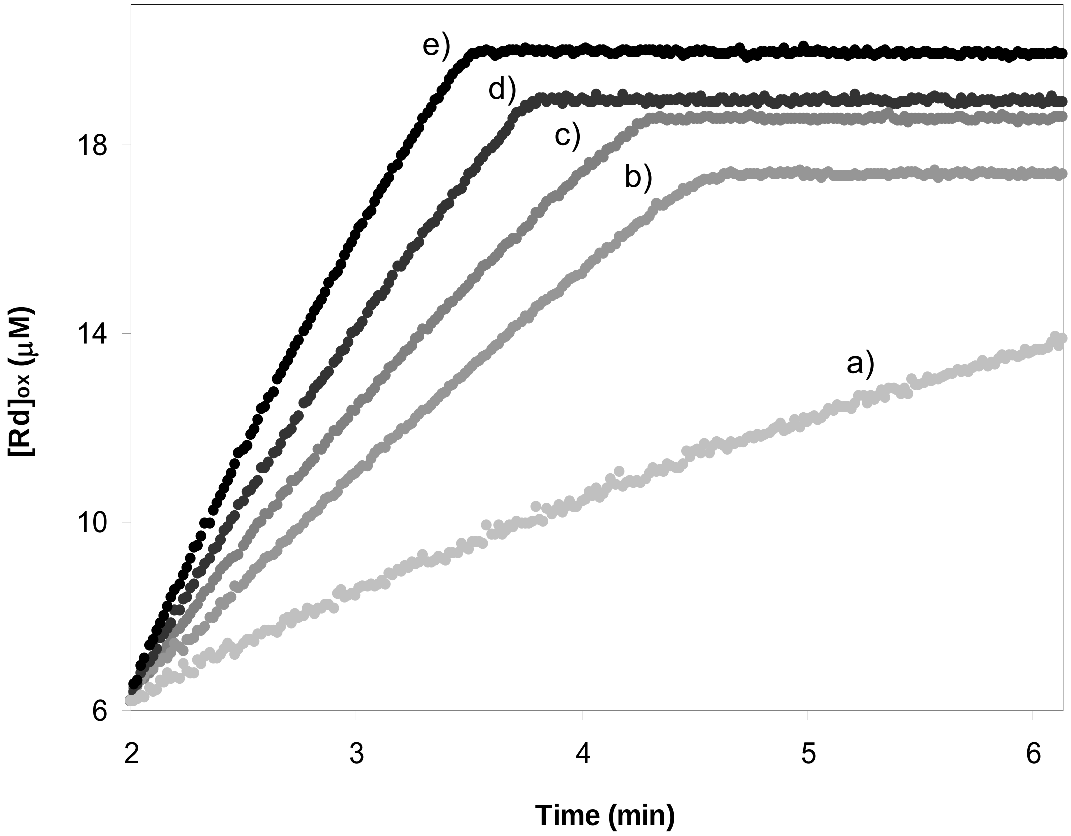

Figure III. 20 - Kinetic traces of superoxide-mediated electron transfer between rubredoxin and the oxidized form of $SOR_{Zn\text{-}Fe}$. The different traces represent different amounts of SOR added, a) 0 μM; b) 0.02 μM; c) 0,2 μM; d) 0.6 μM and e) 1 μM. The assays were performed in 50 mM phosphate buffer pH 7.6 with 0.1 mM EDTA at 23 ºC.

The initial rubredoxin oxidation rate values were plotted against the initial concentration of SOR. The slopes indicate the k' of the three SOR types in study. The following figure and table summarize all the data obtained.

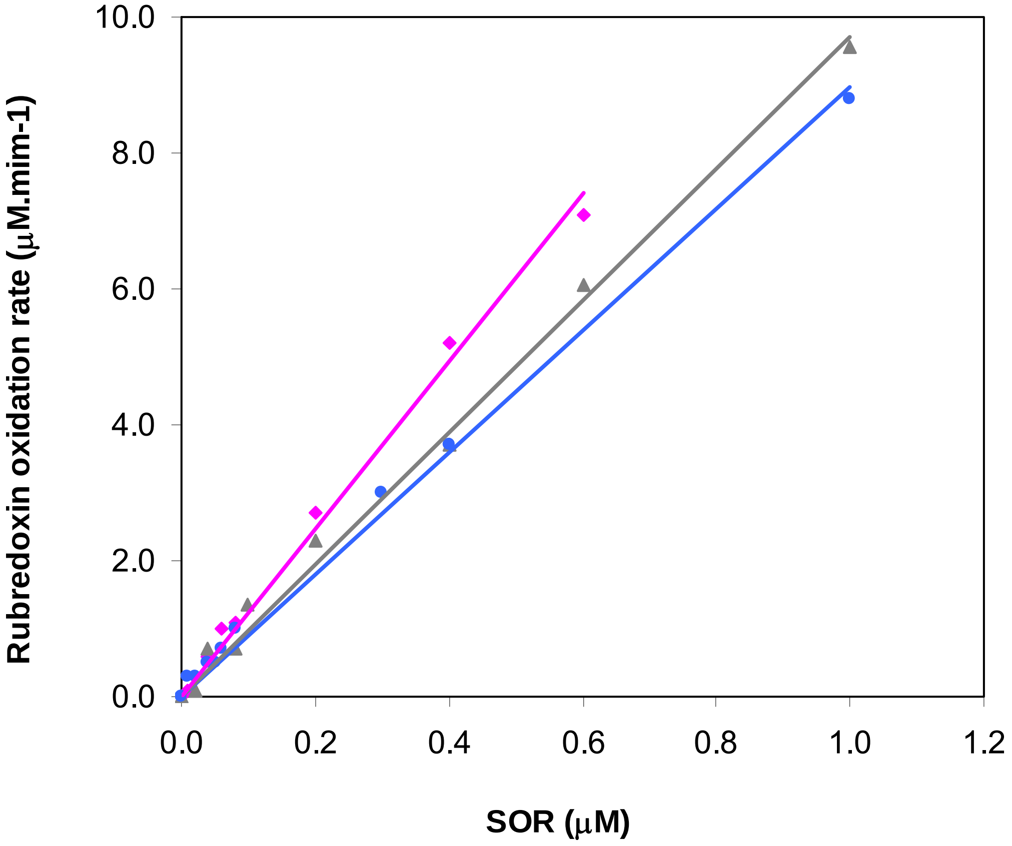

Figure III. 21 – Representation of rubredoxin oxidation rate by superoxide-mediated electron transfer. The pink squares stand for the pink form of $SOR_{Fe\text{-}Fe}$, gray triangles for the gray form of $SOR_{Fe\text{-}Fe}$ and blue dots for the oxidized form of $SOR_{Zn\text{-}Fe}$.

Table III. 4 – k' values calculated for the superoxide-mediated electron transfer between rubredoxin and the three SOR forms in study

k' (min^{-1})		
Pink	Gray	$SOR_{Zn\text{-}Fe}$
12.34 ± 0.08	9.72 ± 0.06	8.98 ± 0.04

As for the direct electron transfer, it was verified that in a superoxide-mediated reaction the rubredoxin oxidation rate was higher with the pink form than for the other forms. This fact could be due to the presence of an already reduced center II, where the catalysis takes part. To test this hypothesis a new experiment was performed, where both forms $SOR_{Fe\text{-}Fe}$ and $SOR_{Zn\text{-}Fe}$ were fully reduced at the beginning of the experiment. Since initial reaction rate is the only data used for the rate constant calculations, the result of this experiment, whether there is difference or not between them, should answer the question. The results are shown in the next figure.

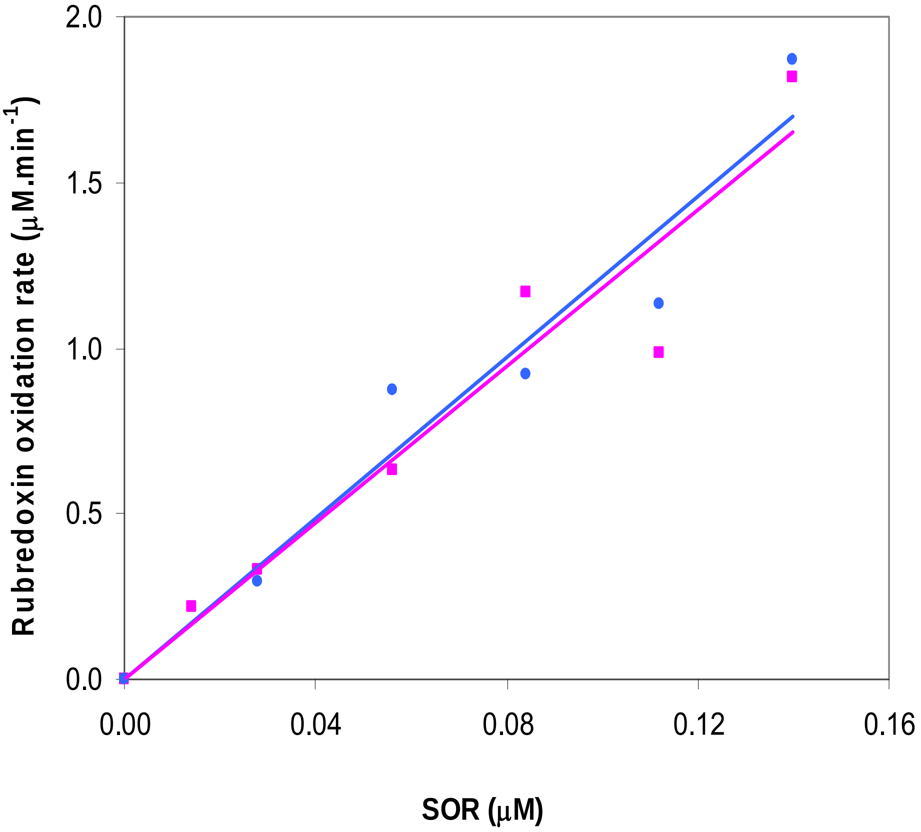

Figure III. 22 - Representation of rubredoxin oxidation rate by superoxide-mediated electron transfer. The pink squares stand for the reduced $SOR_{Fe\text{-}Fe}$, and blue dots for the reduced $SOR_{Zn\text{-}Fe}$.

Table III. 5 – k' values calculated for the superoxide-mediated electron transfer between rubredoxin and all SOR forms in study

k' (min^{-1})				
Pink	Gray	SOR_{Zn-Fe}	Red. SOR_{Fe-Fe}	Red. SOR_{Zn-Fe}
12.34 ± 0.08	9.72 ± 0.06	8.98 ± 0.04	11.79 ± 0.86	12.12 ± 0.73

This last experiment revealed that, within the experimental error, similar initial oxidation rates were verified for both reduced forms of SOR and for the pink form of SOR_{Fe-Fe}. This may indicate that when the center II is reduced at the beginning of the reaction, the presence of center I is not relevant for catalysis. The smaller reaction rate constants observed in the gray and oxidized SOR_{Zn-Fe} forms are in accordance with this fact, since in both of these cases center II has to be reduced prior to the reaction with superoxide radical, leading to a slower reaction rate.

III.2.6 – *Desulfovibrio gigas* SOR, Mössbauer studies

To complete the spectroscopic studies of SOR proteins, the *Desulfovibrio gigas* SOR (originally denominated neelaredoxin) was studied by Mössbauer spectroscopy. As was mentioned in chapter I, this protein is a class II SORs and has only the center II in it constitution. Spectroscopicaly, the Mössbauer spectra should be similar to those found for the gray form of *Desulfovibrio desulfuricans* ATCC 27774 SOR[4, 6].

In order to obtain these data, several studies were preformed where a ^{57}Fe enriched protein was used. These experiments consisted in studying both as-purified and reduced states of the enzyme.

Two Mössbauer spectra of the as-purified form of neelaredoxin were recorded at 4.5 K in the presence of an applied weak magnetic field. The spectra were acquired with a 600 G field applied either parallel or perpendicular to the γ radiation beam. Both spectra are similar, presenting two major components corresponding to a quadrupole doublet (47%) with the following parameters, ΔE_Q = 3.00 mm/s and δ = 1.07 mm/s. These parameters are assigned to high-spin (S=2) ferrous iron coordinated by oxygen or nitrogen ligands.

The second component, accounting for 53%, revealed, as expected, characteristic parameters of a high-spin (S=5/2) ferric iron, very similar to those found for the gray forms of *Dd* SOR. All the parameters are listed in table III.6.

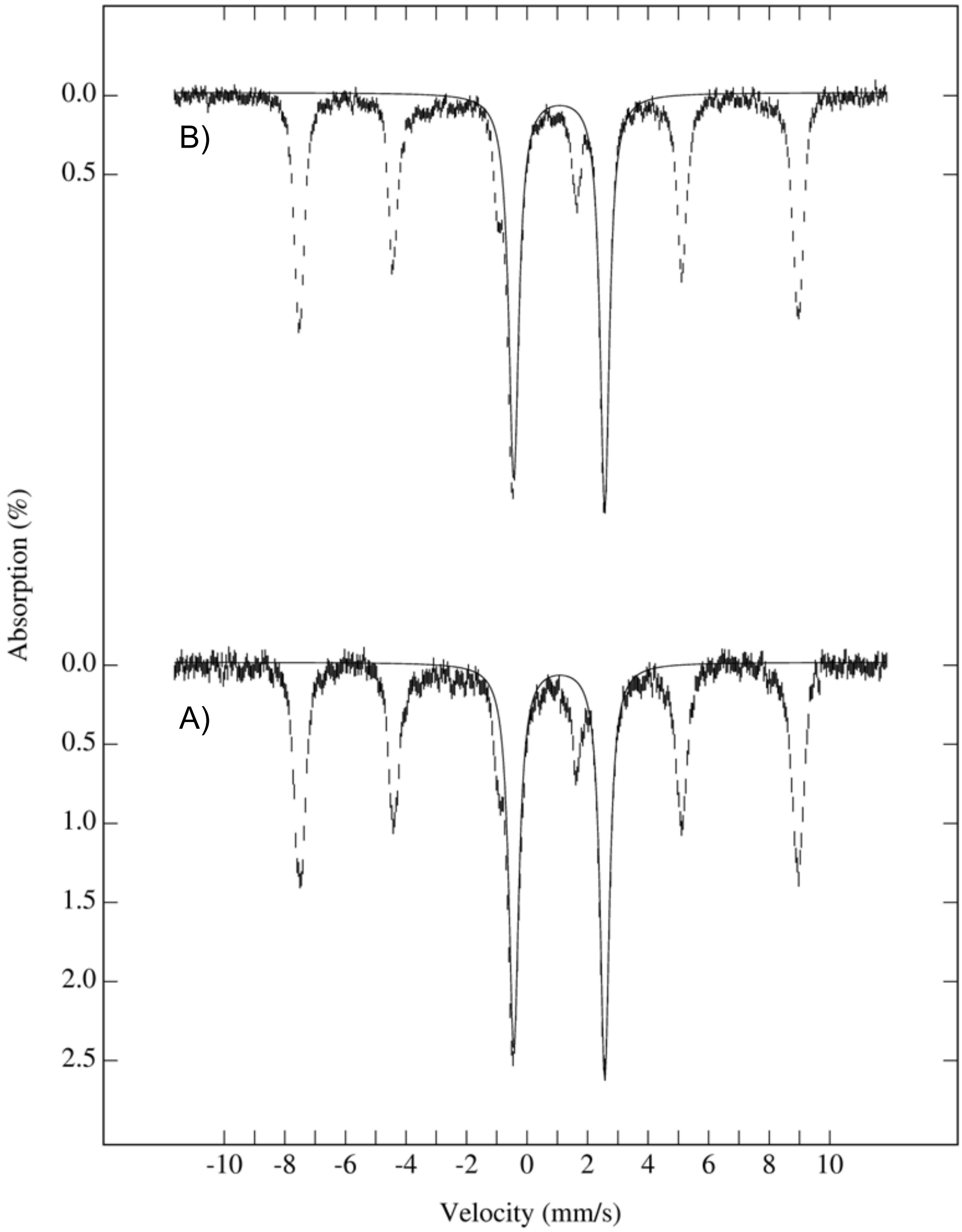

Figure III. 23 – A) Mössbauer spectrum of the as-purified neelaredoxin recorded at 4.5 K in the presence of a weak magnetic field of 600G parallel to the γ radiation beam. B) Mössbauer spectrum of the as-purified neelaredoxin recorded at 4.5 K in the presence of a weak magnetic field of 600 G perpendicular to the γ radiation beam. The solid lines represent the theoretical fits for the 47% of the reduced component of neelaredoxin.

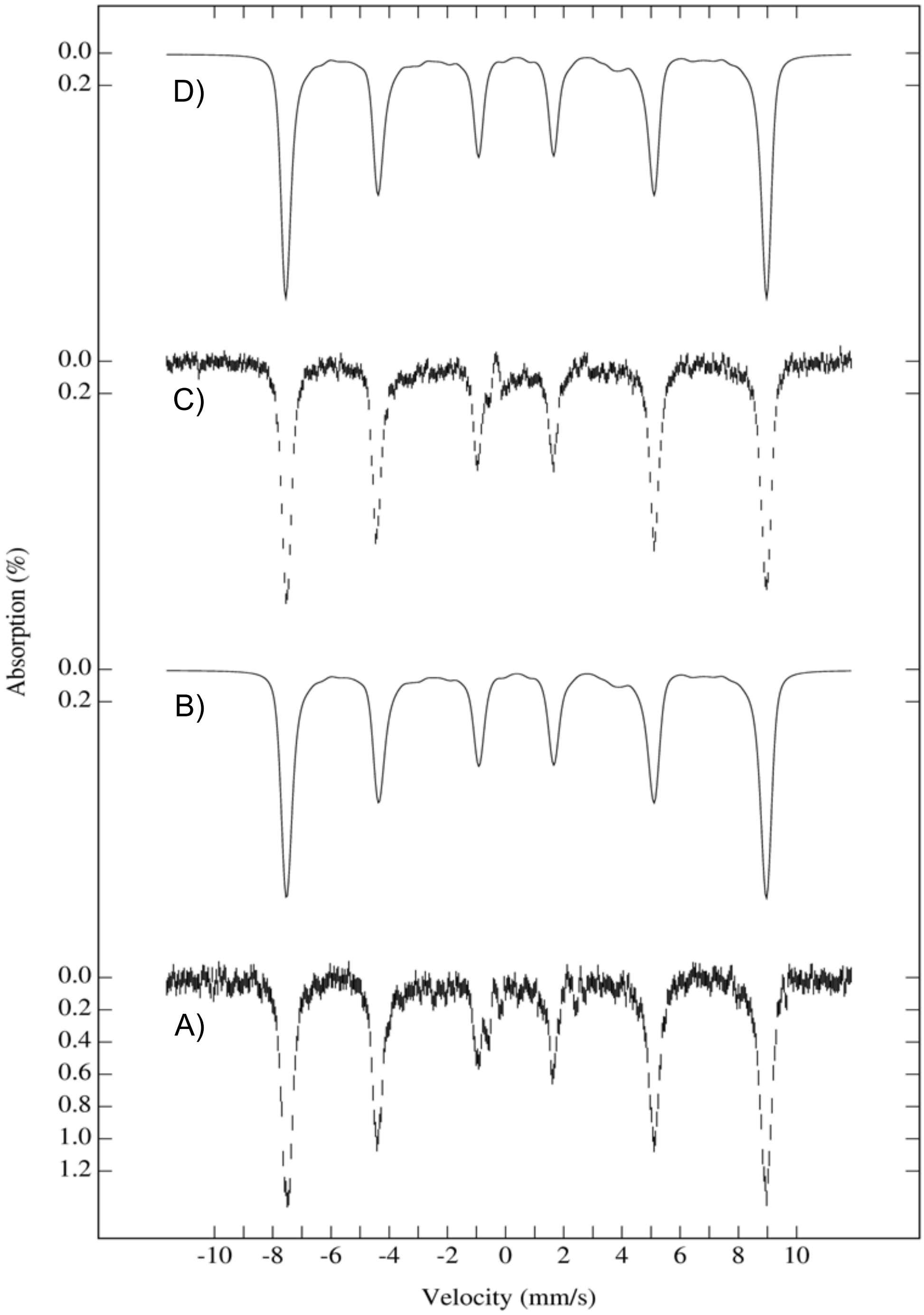

Figure III. 24 – A) Mössbauer spectrum of the 53% oxidized component of neelaredoxin recorded at 4.5 K in the presence of a weak magnetic field of 600 G parallel to the γ radiation beam. C) Mössbauer spectrum of the 53% oxidized component of neelaredoxin recorded at 4.5K in the presence of a weak magnetic field of 600 G perpendicular to the γ radiation beam. The solid lines B) and D) represent the theoretical fits for the oxidized component of neelaredoxin.

Table III. 6 – Parameters used to fit both components of Mössbauer spectra of as-purified neelaredoxin

Parameter	Component A	Component B
D (cm^{-1})	0	< -5
E/D	0	0.31 ± 0.02
ΔE_Q (mm/s)	3.00 ± 0.01	0.56 ± 0.02
δ (mm/s)	1.07 ± 0.02	0.55 ± 0.01
A_{xx}, A_{yy}, A_{zz} (kG)	0	-200 ± 5, -200 ± 5, -213 ± 1
η	0	-2.20± 0.02
Γ	0.37	0.32

The Mössbauer spectrum recorded at high temperature (200 K with no applied magnetic field) shows that at this temperature, the oxidized component of as-purified neelaredoxin is still not totally collapsed, contributing to the broad shape of the quadrupole doublet correspondent to the reduced component. For that reason it was also not possible to calculate Mössbauer parameters for the ferric species.

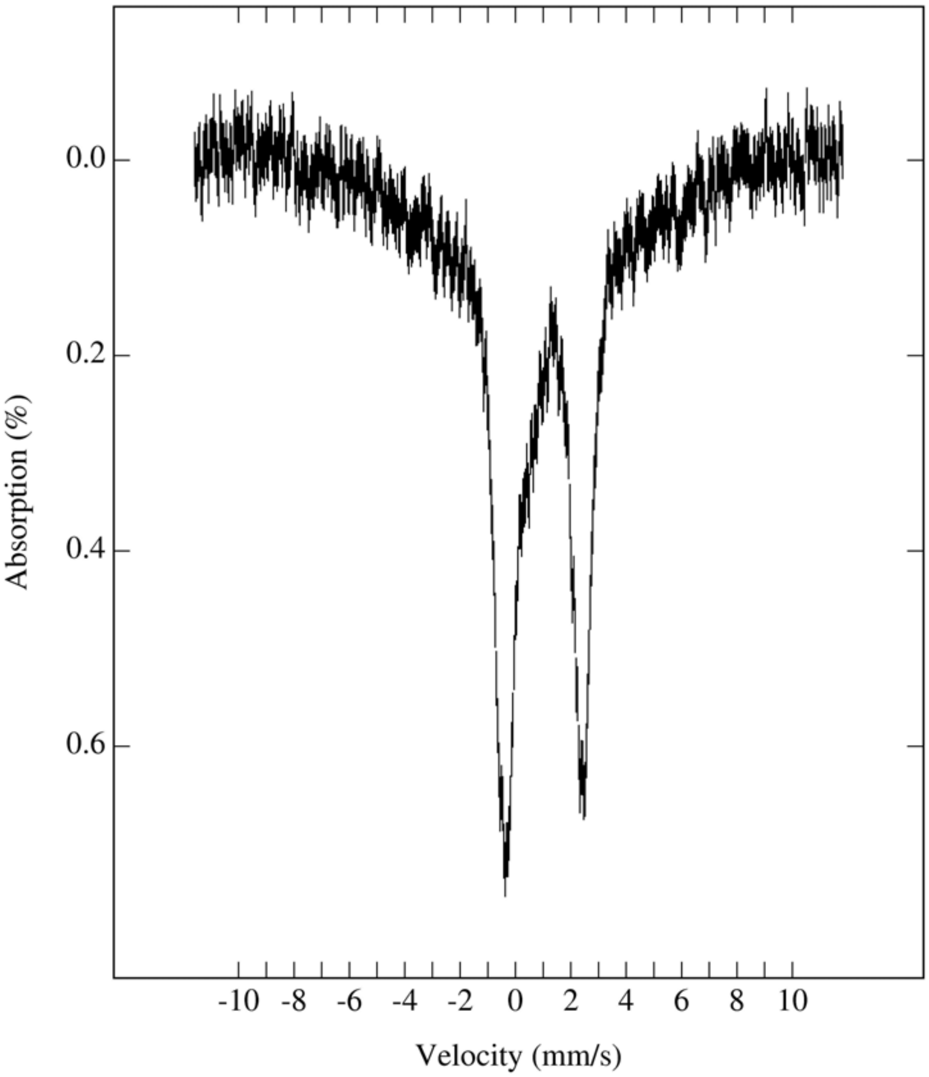

Figure III. 25 - Mössbauer spectrum of the as-purified neelaredoxin recorded at 200 K with no applied magnetic field.

Upon dithionite reduction of the as-isolated sample, the 4.5K spectrum consists of a single quadrupole doublet with ΔE_Q = 3.01 mm/s and δ = 1.03 mm/s, consistent with the conversion of the ferric into the ferrous species. Such observation indicates the presence of a single iron site that, due to the formal redox potential ($E^{0\prime}$= 190 mV), is in the as-purified state in a mixture of redox states[8].

Finally, a temperature dependence study was performed. The Mössbauer spectra of dithionite reduced neelaredoxin were recorded with no applied magnetic field, between 4.5 K and 200 K. All the spectra were fitted with a single quadrupole doublet corresponding to the high-spin (S=2) ferrous iron coordinated by either oxygen or nitrogen ligands.

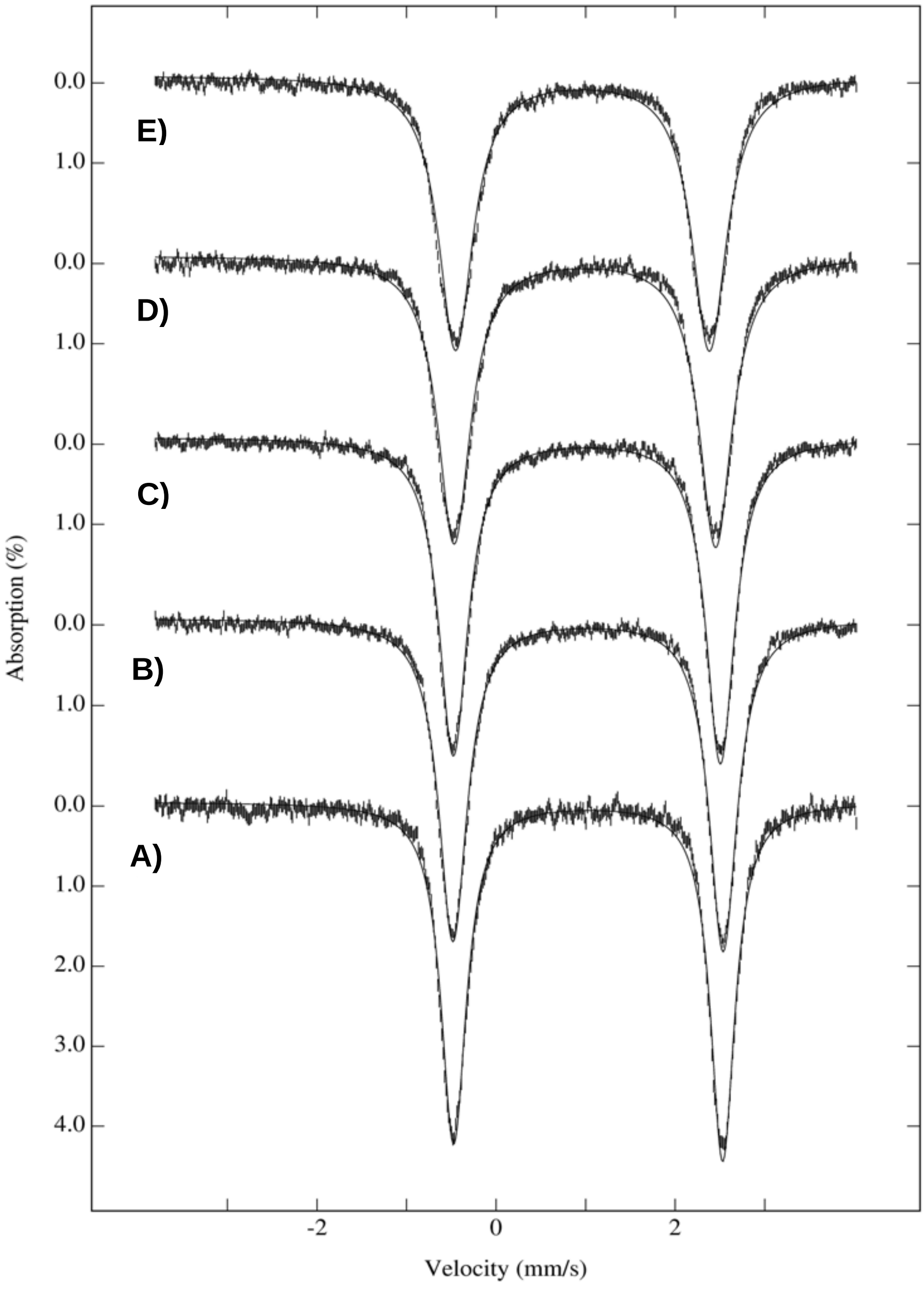

Figure III. 26 – Mössbauer spectra of temperature dependence performed for the dithionite reduced form of neelaredoxin. A) 4.5 K; B) 50 K; C) 100 K; D) 150 K; E) 200 K. The solid lines are fits of a single quadrupole doublet o the experimental data obtained for each temperature.

Figure III.27 represents dependence of ΔE_Q and δ the temperature.

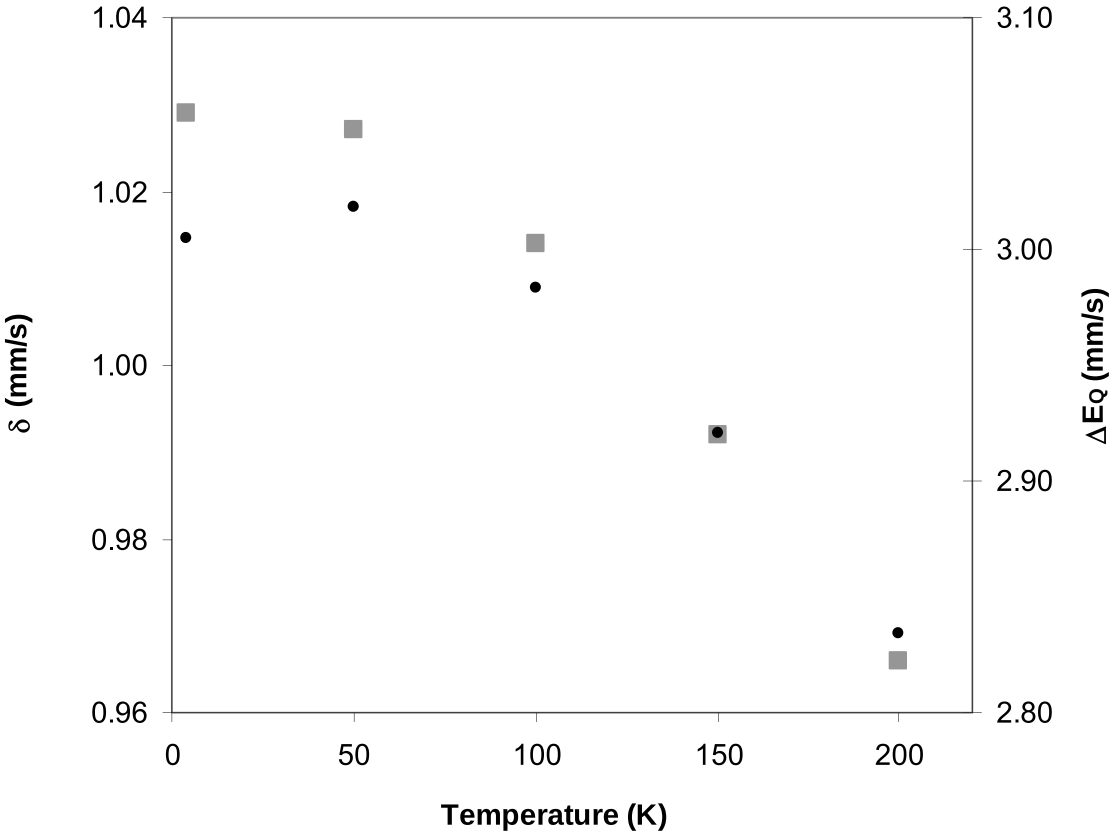

Figure III. 27 – Temperature dependence obtained for δ (gray squares) and ΔE_Q (black dots). The spectra of the dithionite reduced form of neelaredoxin were recorded between 4.5 K and 200 K, with no applied magnetic field.

III.3 – Discussion

At the beginning of this chapter it was proposed to try to understand both the interaction between *Dv* SOR and rubredoxin as well as the possible advantage of having two iron centers for catalysis (instead of one iron center, such as in class II and class III SORs). The overexpression of modified SOR containing zinc in center I instead of iron improved the chances of obtaining more and better data.

This new form revealed some spectroscopic features similar to class II and III SORs, such as the UV-Vis and EPR spectra. On the other hand, the a. a. sequence analysis proved that this protein was identical to the original *Dv* SOR (predicted by gene analysis). With these data and without any further structural information, it was possible to assume a structurally intact but chemically different SOR.

The first experiments performed focused on the direct electron transfer between rubredoxin (the proposed physiological electron donor) and the three different forms of SOR (pink, gray and Zn-Fe). The experiments revealed the existence of electron transfer between rubredoxin and all the three forms of SOR in study. The kinetic rate constants calculated for both gray and Zn-Fe forms were comparable to previously published data, but a 10 fold increase was observed in the pink form, suggesting an easier reduction of center I [9, 11, 17, 18]. In a first approach, this could mean that the preferential electron transfer pathway from rubredoxin to SOR is through center I.

Nevertheless, the kinetic evidences obtained in this work could also point to a direct electron transfer to center II. This was supported by the similarity of the rate constants found in the gray form for 500 nm (oxidation of rubredoxin) and 650 nm (reduction of center II), which were themselves similar to the calculated for the Zn-Fe form (where center I is not available). So, what could explain the faster direct electron transfer to center I of the protein when it is in the pink form?

Because the reduced center II is the catalytic active site and center I is, according to the stopped-flow data, reduced faster by ferrous rubredoxin (when in the pink form), probably there is some sort of intramolecular electron transfer that maintains not only the center II always in a reduced state, ready for catalysis but also the protein in the pink form, the most favorable to receive electrons and to continue the catalytic cycle.

Besides, the faster electron transfer to center I could be also promoted by a conformational change in the protein when center II is in the reduced state (pink form). This type of long range (22 Å) intramolecular electron transfer, coupled to conformational change is not unique in Nature, being found in other examples like cytochrome *c* Oxidase (CcO), described in chapter I of this thesis[19, 20]. If this was the case, the pink form "conformation" would not only increase the protein's ability to receive electrons (at center I), but also promote an effective reduction of the oxidized center II (via center I due to the intramolecular electron transfer) during catalytic cycle. All this together would maintain the protein in the most favorable form.

Probably, this behavior has a biological significance, since even for the superoxide-mediated electron transfer assay, the pink form is again the most effective. This could mean that inside a living cell, the pink form would be an "always ready" form, that not only is the most catalytically effective but also the easiest to reduce, contributing to an efficient degradation of superoxide anion and, consequently, less damage to the cell[1].

Confer these functions to center I could also explain the experimental observations when completely reduced forms of both Fe-Fe and Zn-Fe were used to the superoxide-mediated electron transfer. In this case, no difference in the k' was observed which means that the catalysis itself does not depend directly on center I but is favored by its presence (proved by the pink form assay).

Therefore, the existence of center I can be seen as a structural advantage to the enzyme, enabling it to be more efficient in the metabolic pathway and helping the cell to keep a pool of "ready" enzyme for catalysis.

Computational studies performed using the protein crystallographic structures (from *Dv* rubredoxin and *Dd* SOR), didn't provide conclusive answers with respect to the docking site between these two proteins. However they also don't exclude the previous postulated hypothesis. Figure III.28 illustrates the results obtained.

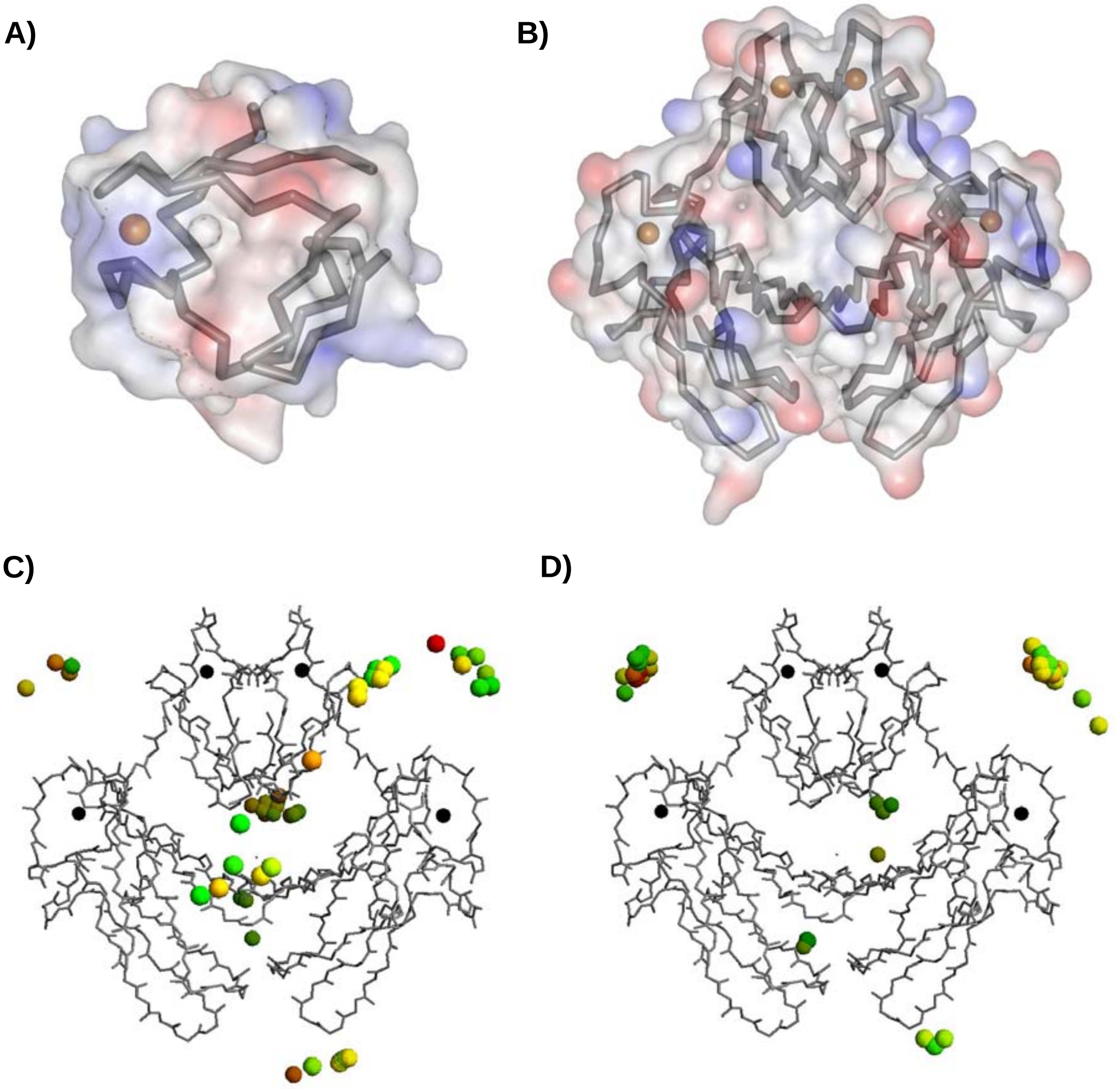

Figure III. 28 – A) Superficial charge of *Dv* rubredoxin calculated by Poisson-Boltzmann. B) Superficial charge of *Dd* SOR calculated by Poisson-Boltzmann. The blue color stands for positive charges and the negative charges are represented by the red color. The calculations were performed using WebLab ViewerPro 3.7, molecular Simulations Inc. C) Top 50 docking solutions calculated for the interaction between rubredoxin and SOR, ranked according to the minimization of electrostatic repulsion energy upon formation of the complex. D) Top 50 docking solutions calculated for the interaction between rubredoxin and SOR, ranked according to the best side chain interaction upon formation of the complex. The rubredoxin molecules are represented by their geometric center only for clarification purposes. The calculations were performed using the Chemera 3.0 software (http://www.cqfb.fct.unl.pt/bioin/chemera/Chemera/Intro.html).

The Mössbauer studies of neelaredoxin revealed, as expected, similar characteristics to the previously reported for the center II of class I SOR[4, 6]. The parameters obtained correspond to a high spin iron center, S=2 for the reduced form and S=5/2 for the oxidized form, coordinated with either oxygen or nitrogen. From the Mössbauer study it was also possible to conclude that the as-purified form is in redox equilibrium between the ferric and ferrous state (53% of ferric iron and 47% of ferrous iron).

III.4 – References

[1] A.S. Pereira, P. Tavares, F. Folgosa, R.M. Almeida, I. Moura, J.J.G. Moura, Superoxide reductases, European Journal of Inorganic Chemistry (2007) 2569-2581.

[2] C. Ascenso, F. Rusnak, I. Cabrito, M.J. Lima, S. Naylor, I. Moura, J.J. Moura, Desulfoferrodoxin: a modular protein, J Biol Inorg Chem 5 (2000) 720-729.

[3] F. Auchere, S.R. Pauleta, P. Tavares, I. Moura, J.J. Moura, Kinetics studies of the superoxide-mediated electron transfer reactions between rubredoxin-type proteins and superoxide reductases, J Biol Inorg Chem 11 (2006) 433-444.

[4] P. Tavares, N. Ravi, J.J. Moura, J. LeGall, Y.H. Huang, B.R. Crouse, M.K. Johnson, B.H. Huynh, I. Moura, Spectroscopic properties of desulfoferrodoxin from Desulfovibrio desulfuricans (ATCC 27774), J Biol Chem 269 (1994) 10504-10510.

[5] M.F. Verhagen, W.G. Voorhorst, J.A. Kolkman, R.B. Wolbert, W.R. Hagen, On the two iron centers of desulfoferrodoxin, FEBS Lett 336 (1993) 13-18.

[6] I. Moura, P. Tavares, J.J. Moura, N. Ravi, B.H. Huynh, M.Y. Liu, J. LeGall, Purification and characterization of desulfoferrodoxin. A novel protein from Desulfovibrio desulfuricans (ATCC 27774) and from Desulfovibrio vulgaris (strain Hildenborough) that contains a distorted rubredoxin center and a mononuclear ferrous center, J Biol Chem 265 (1990) 21596-21602.

[7] M.J. Winter, d-Block chemistry, Oxford University Press, 1994.

[8] L. Chen, P. Sharma, J. Le Gall, A.M. Mariano, M. Teixeira, A.V. Xavier, A blue non-heme iron protein from Desulfovibrio gigas, Eur J Biochem 226 (1994) 613-618.

[9] J.V. Rodrigues, I.A. Abreu, L.M. Saraiva, M. Teixeira, Rubredoxin acts as an electron donor for neelaredoxin in Archaeoglobus fulgidus, Biochem Biophys Res Commun 329 (2005) 1300-1305.

[10] F. Auchere, R. Sikkink, C. Cordas, P. Raleiras, P. Tavares, I. Moura, J.J. Moura, Overexpression and purification of Treponema pallidum rubredoxin; kinetic evidence

for a superoxide-mediated electron transfer with the superoxide reductase neelaredoxin, J Biol Inorg Chem 9 (2004) 839-849.

[11] J.P. Emerson, E.D. Coulter, R.S. Phillips, D.M. Kurtz, Jr., Kinetics of the superoxide reductase catalytic cycle, J Biol Chem 278 (2003) 39662-39668.

[12] J.P. Emerson, D.E. Cabelli, D.M. Kurtz, Jr., An engineered two-iron superoxide reductase lacking the [Fe(SCys)4] site retains its catalytic properties in vitro and in vivo, Proc Natl Acad Sci U S A 100 (2003) 3802-3807.

[13] J.V. Rodrigues, L.M. Saraiva, I.A. Abreu, M. Teixeira, D.E. Cabelli, Superoxide reduction by Archaeoglobus fulgidus desulfoferrodoxin: comparison with neelaredoxin, J Biol Inorg Chem 12 (2007) 248-256.

[14] E.M. Link, P.A. Riley, Role of hydrogen peroxide in the cytotoxicity of the xanthine/xanthine oxidase system, Biochem J 249 (1988) 391-399.

[15] E.W. Kellogg, 3rd, I. Fridovich, Superoxide, hydrogen peroxide, and singlet oxygen in lipid peroxidation by a xanthine oxidase system, J Biol Chem 250 (1975) 8812-8817.

[16] I. Fridovich, Superoxide dismutases, Annu Rev Biochem 44 (1975) 147-159.

[17] J.V. Rodrigues, I.A. Abreu, D. Cabelli, M. Teixeira, Superoxide reduction mechanism of Archaeoglobus fulgidus one-iron superoxide reductase, Biochemistry 45 (2006) 9266-9278.

[18] E.D. Coulter, D.M. Kurtz, Jr., A role for rubredoxin in oxidative stress protection in Desulfovibrio vulgaris: catalytic electron transfer to rubrerythrin and two-iron superoxide reductase, Arch Biochem Biophys 394 (2001) 76-86.

[19] T.L. Poulos, H. Li, C.S. Raman, Heme-mediated oxygen activation in biology: cytochrome c oxidase and nitric oxide synthase, Curr Opin Chem Biol 3 (1999) 131-137.

[20] C.C. Page, C.C. Moser, X. Chen, P.L. Dutton, Natural engineering principles of electron tunnelling in biological oxidation-reduction, Nature 402 (1999) 47-52.

Structural and mechanistic studies of metal incorporation in rubredoxin from *Desulfovibrio gigas*

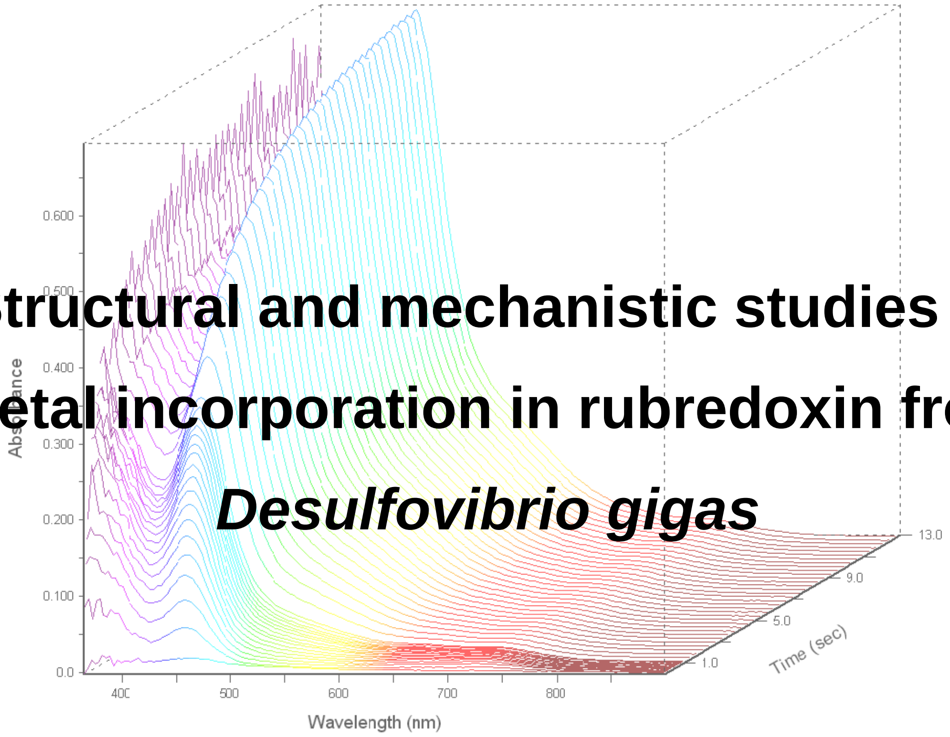

Index

Chapter IV

Structural and mechanistic studies of metal incorporation in rubredoxin from *Desulfovibrio gigas*

IV.1 – Overview

As described before, *D. gigas* rubredoxin (Rd) is a small monomeric protein, containing only one iron atom and also a single tryptophan. From the physiological point of view, rubredoxins have been characterized as electron donors of several enzymatic systems[1-3]. But, more than a good electron donor, rubredoxin is also an excellent model for structural studies in metalloproteins.

Since the 90's, several authors reported procedures for metal incorporation in different proteins[4]. Rubredoxin is one of the proteins mentioned in this type of studies, and is able to receive several other metals besides iron. This fact is relevant if we consider that for some spectroscopic studies, such as Nuclear Magnetic Resonance, it is important to have "silent" metals, like the diamagnetic Zn^{2+}, in order to obtain data that would be impossible to obtain if the "original" metal, in this case iron, was present.

However, little is known about the mechanism involved in the metal incorporation. Does metal bind in a single step? Is the oxidation state of the metal important for the incorporation? Do all the metals get incorporated by the same mechanism?

This chapter aims to answer those questions by studying the incorporation of different metals in an apoprotein form of rubredoxin. For these studies, UV-visible stopped-flow techniques will be used. For the iron incorporation, Mössbauer spectroscopy, coupled with anaerobic rapid-freeze quench techniques, was also chosen.

IV.2 - Experimental

IV.2.1 – Overexpression and purification of recombinant *D. gigas* rubredoxin

Commercial competent *E. coli* cells (strain BL21(DE3), Invitrogen®) were transformed with the correspondent plasmid in order to obtain desired recombinant protein. All the transformation procedures were carried out according to the manufacturer’s recommendations (Appendix A). After the transformation process, the cells were plated in LB-Agar medium containing 0.1 mg/mL ampicillin and left to grow overnight at 37 ºC. Resulting colonies were used to start the overexpression of the desired proteins.

The overexpression procedure was as described in the literature with minor changes[5]. Two steps of pre-cultures were performed prior to the main overexpression growth. The first step consisted in a 5 mL pre-inoculum in LB media containing 0.1 mg/mL ampicillin, that was grown overnight (from 10 to 12 hours) at 37 ºC at 225 rpm. The second step consisted in the addition of 1 mL of this pre-culture to 100 mL LB media containing 0.1 mg/mL ampicillin. This culture was left to grow overnight at 37 ºC at 225 rpm. Finally, 10 mL of this culture were inoculated into 1000 mL (usually 6 L total, 6 x 1000 mL) of LB media containing 0.1 mg/mL ampicillin and 0.1 mM $FeCl_2$. The cells were allowed to grow at 37 ºC at 230 rpm until its O.D. was near 0.8 at 600 nm. At this time 1 mM IPTG and 0.1 mM $FeCl_2$ were added and the culture was able to grow for approximately 14 hours at room temperature (between 20 and 25 ºC) at 230 rpm. All the growth procedures were made aerobically.

After growth, the cells were harvested by centrifugation at 10,000 x *g* for 8 min at 4 ºC. After centrifugation the supernatant was discarded and the cells were suspended in 50 mM Tris-HCl pH 7.8 buffer. A combination of three freeze-thaw cycles (using liquid nitrogen and tepid water) and a French Press® (28000 Psi) apparatus were used for cell disruption. During this process a small amount of DNAse (purchased from Sigma) was added to ensure DNA degradation and, consequently, a cleaner sample. Cell disruption was followed by ultracentrifugation, 138,000 x *g* at 4ºC for 1h 30 min, in order to separate the fraction containing the desired protein from other cellular components.

The resulting supernatant was then purified to homogeneity by an anionic exchange chromatography followed by a gel filtration chromatography. All purification steps were carried out at 4 ºC and at pH 7.8.

The first step consisted in loading the fraction into a column XK26/40 (2.6 x 30cm) (GE HealthCare®) filled with a DEAE-Sepharose FF® resin (GE HealthCare®), previously equilibrated with 50 mM Tris-HCl pH 7.8 buffer. After loading, the column was washed with two volumes of the equilibrating buffer in order to remove all the proteins that did not adsorb to the matrix. An 800 mL gradient was applied (50 – 1000 mM Tris-HCl pH 7.8) and the protein was collected between 250 – 350 mM.

After this chromatographic step two fractions were made according to the purity verified by UV-Visible spectra and SDS-PAGE electrophoresis (see Appendix A). Both fractions containing rubredoxin were concentrated using a Diaflo® apparatus with an YM3 membrane.

In the second chromatographic step, the samples were loaded into a XK26/100 column packed with Superdex75® (Amersham Biosciences®), previously equilibrated with 300mM Tris-HCl pH 7.8. Judging by the UV-Visible spectra and SDS-PAGE electrophoresis, it was clear that this second chromatographic step was very effective for complete protein isolation. Thus, a fraction containing pure *Dg* rubredoxin (purity ratio of $Abs_{280}/Abs_{490} = 2.2$) was then concentrated as described before and the buffer was exchanged to 50 mM Tris-HCl pH 7.8 by successive buffer addition.

IV.2.2 – Production of apoprotein of *D. gigas* rubredoxin

As mentioned before, it is important to have the protein in an apoprotein form to be used for metal incorporation experiments. The procedures described by Moura and coworkers were followed with some modifications[4].

Depending on the experiment, an initial concentration of recombinant rubredoxin (containing iron, Rd_{Fe}) was calculated in order to achieve the desired final concentration of apoprotein. Production of clean, reduced apoprotein was accomplished in four steps.

The first step consisted of incubation with 0.5M Dithiothreitol (DTT) and 5% (w/v) Trichloroacetic Acid (TCA) at 45 ºC for about 30 minutes. After this time, a white pellet (precipitated protein) was formed. The second step consisted in the separation of the apoprotein by centrifugation at 7700 x *g* at 8 ºC for 30 minutes. After this step, the supernatant was discarded and the pellet was dissolved in a 2mL solution of 0.5M Tris-Base and 60mM DTT. This solution was degassed in a Schlenk line with argon/vacuum cycles and, finally, desalted anaerobically with 50 mM MES buffer pH 6.25, using a 5mL HiTrap™ column (GEHealthcare) inside a glove box. All the metal incorporation assays, as well as the rapid freeze-quench experiments, were performed anaerobicaly in 50 mM MES buffer pH 6.25.

After each procedure, the condition of the apoprotein produced was evaluated spectrophotometricaly in anaerobic conditions. The spectrum shown below provides an example of the typically obtained spectra.

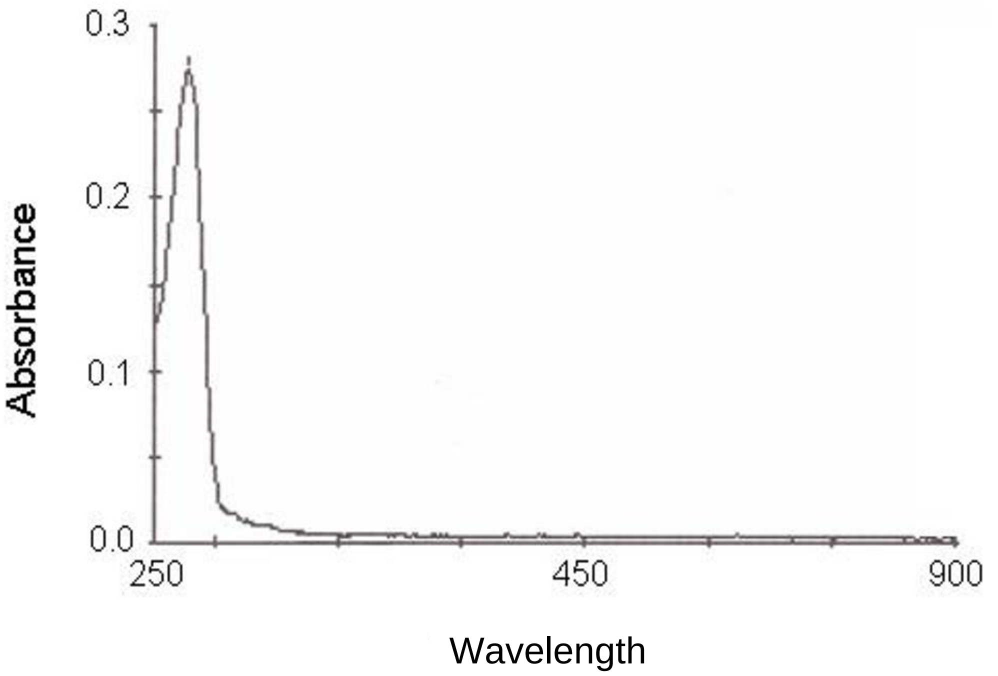

Figure IV. 1 – UV-Vis spectrum of *Dg* rubredoxin apoprotein.

The UV-Visible spectrum does not show any features usually observed when iron is present in rubredoxin. The cysteine-metal charge transfer band, around 320nm, is also not present indicating that the cysteines are reduced and ready to interact with the metal ion[6].

IV.2.3 – Co, Ni, Zn and Fe incorporation in apo rubredoxin. Stopped-flow approach

It is well known from the literature that the UV-Visible features of rubredoxin change according to the metal present in its center[4]. So, a good approach to study this process and its possible intermediates is to follow the spectral changes in time. For that purpose, a stopped-flow experiment was designed in order to obtain the spectral evolution until the final form of the protein.

These experiments consisted in mixing a certain amount of apoprotein with the desired metal and measuring the spectral evolution using a diode array spectrophotometer. Since the purpose was to characterize the possible reaction intermediates and their rates of formation and decay, several kinetic approaches were used. For these studies a second order reaction was assumed with the following equation,

$$v = k\,[Rd_{apo}]\,[M] \qquad \text{Eq. IV. 1}$$

where k is the second order rate constant ($M^{-1}.s^{-1}$), $[Rd_{apo}]$ is the concentration of apoprotein form of rubredoxin and [M] is a generic symbol for concentration of the different metals used. In order to simplify the calculations, pseudo first order conditions were applied assuming,

$$k' = k\,[M] \qquad \text{Eq. IV. 2}$$

where k' is an apparent first order rate constant (s^{-1}) and the [M] value is so large compared to $[Rd_{apo}]$ that it is considered constant during the experiment.

In order to calculate k, several assays were performed with different metal concentrations. The following figures illustrate the results obtained for the assays with Ni^{2+} and Co^{2+}, in the previously described conditions.

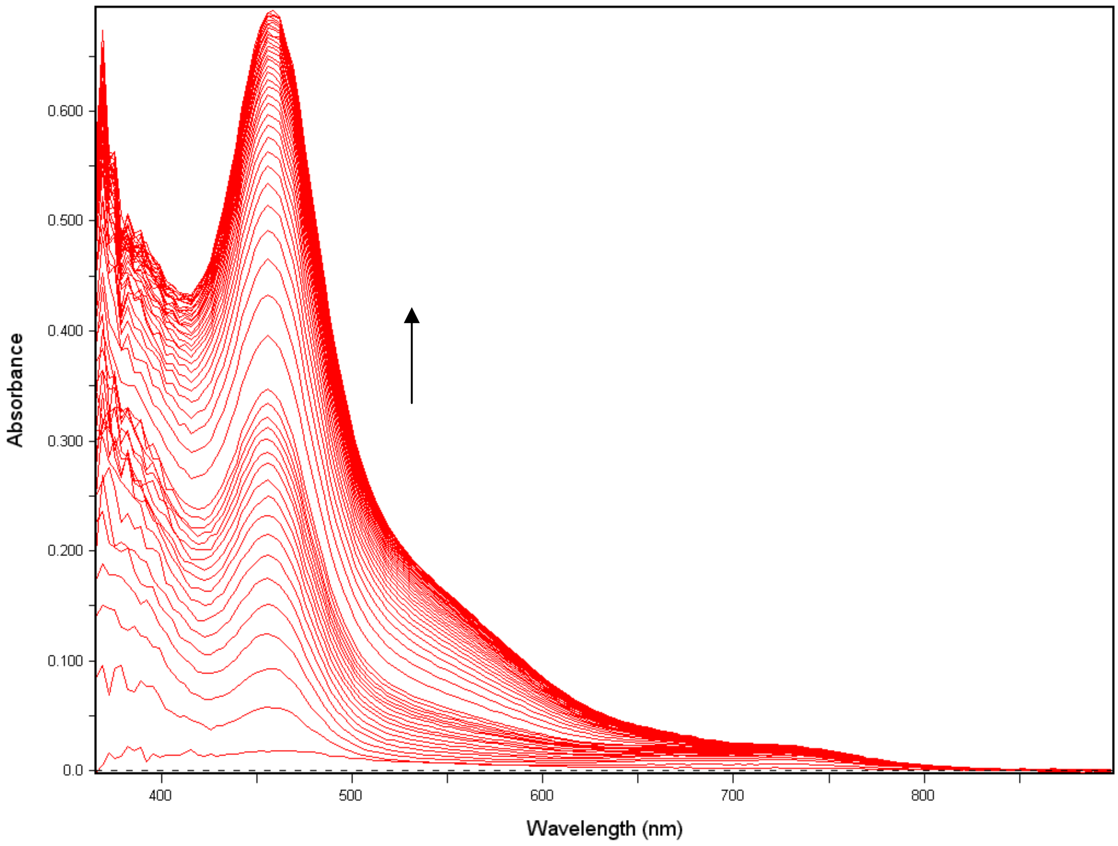

Figure IV. 2 – 2D Spectral evolution of a 1:1 mixture (v/v) of 30 μM ApoRd with 840 μM $NiCl_2$, in 50 mM MES buffer pH 6.25. The arrow points the evolution of the spectra with time.

From figure IV.2 it is possible to observe the formation of a broad peak around 460 nm. The final spectra is similar to the previously described spectra by Moura and coworkers for a nickel substituted rubredoxin[4].

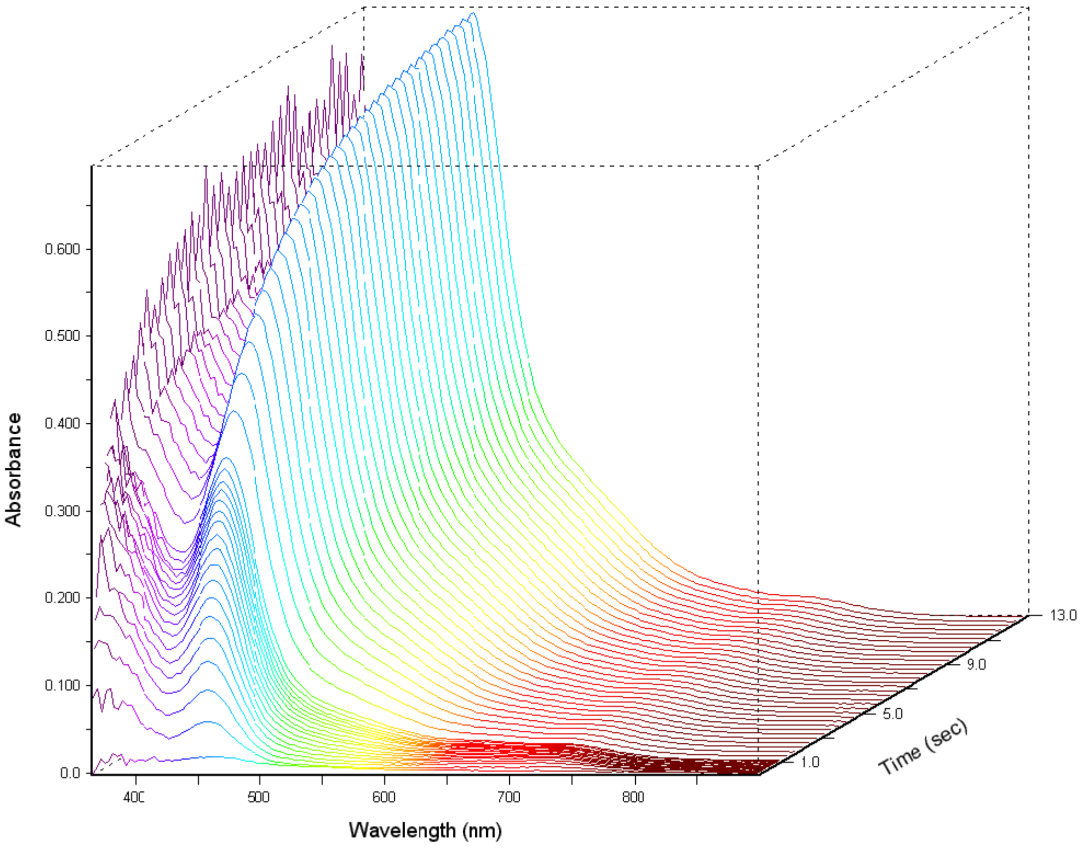

Figure IV. 3 - 3D Spectral evolution of a 1:1 mixture (v/v) of 30 μM ApoRd with 840 μM $NiCl_2$, in 50 mM MES buffer pH 6.25.

Since the incorporation of nickel contains features all over the visible region of the spectrum, the data was analyzed in 3D. Similar to the ferritin experiments presented in chapter 2, SPECFIT© (from Spectrum Software Associates), was also used for data analysis.

From the global analysis it was then possible to determine that this reaction could only be fitted with four consecutive first order rate constants. These data show that the reaction forms three intermediate species before the formation of the final product.

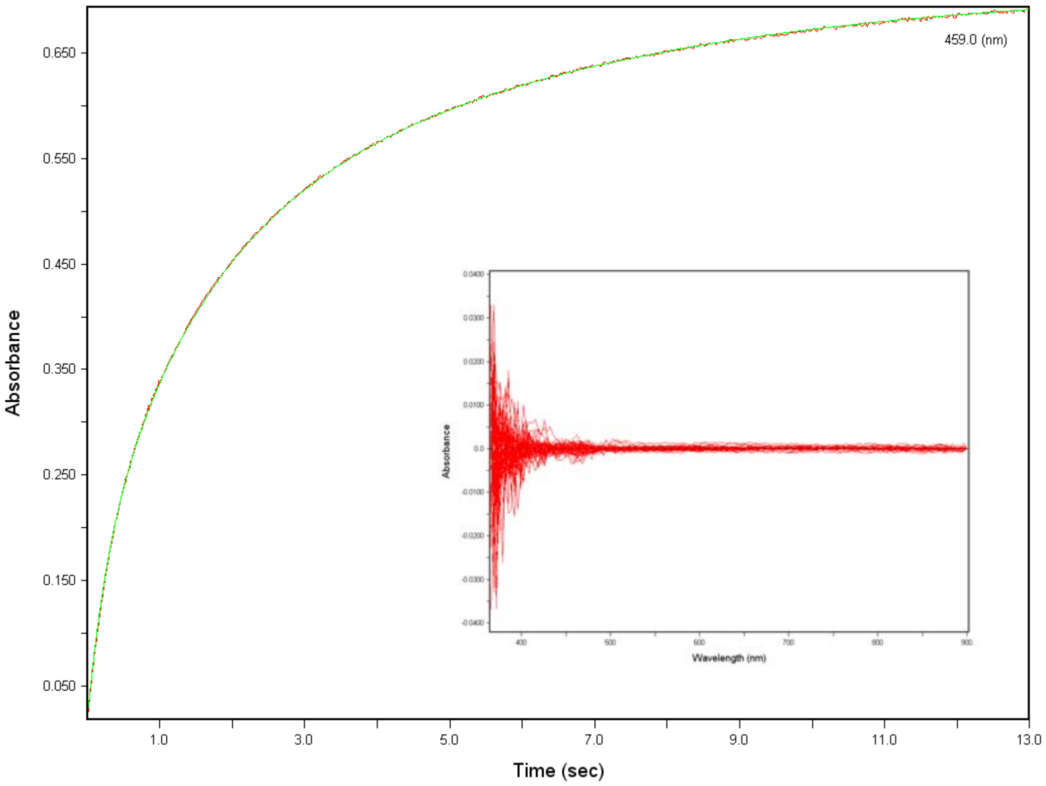

Figure IV. 4 – Kinetic trace of a 1:1 mixture (v/v) of 30 μM ApoRd with 840μM $NiCl_2$, in 50 mM MES buffer pH 6.25. The green line represents the theoretical values obtained at this wavelength (459 nm). The inset represents the residuals for the fit of the overall data.

As was mentioned before, the experimental procedure was designed for a pseudo-first order experiment. So, the obtained values for the first rate constant are the k' shown in equations IV.1 and IV.2. In order to obtain the second order rate constant, these values were plotted against the nickel concentration in each assay. The results are presented in the following figure.

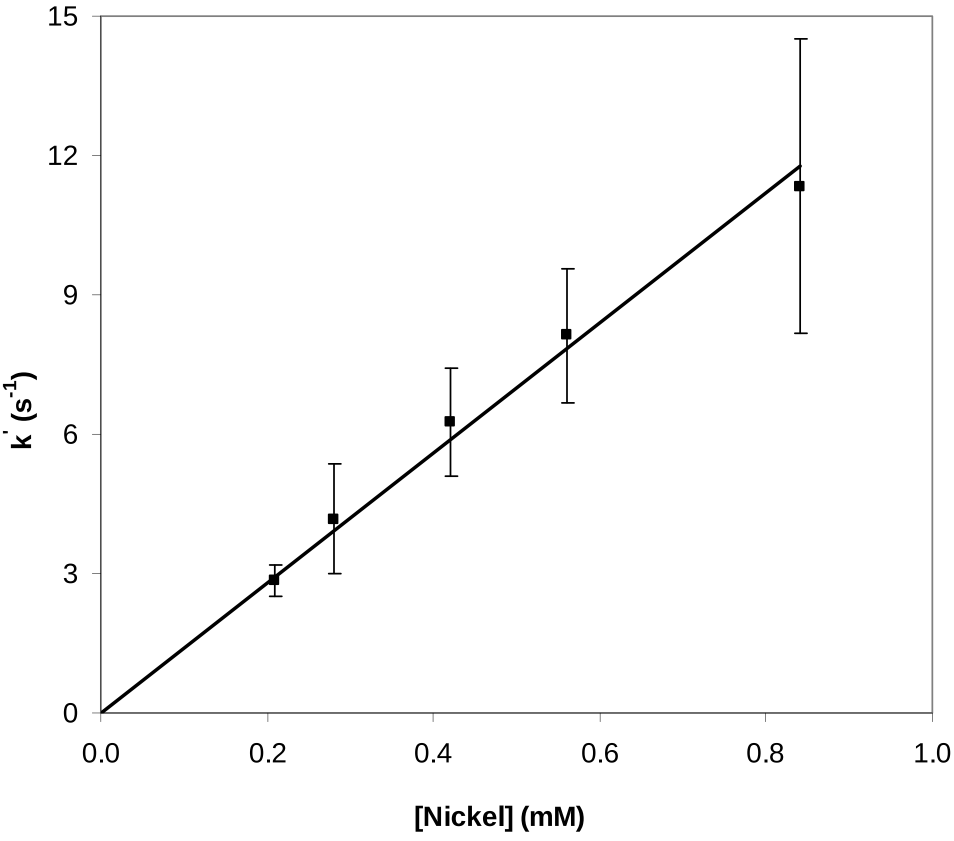

Figure IV. 5 – Metal concentration dependence for the calculated k'. The slope of the trend line indicates the second order rate constant for the first step.

From this plot the calculated second order rate constant for the first step of the reaction was determined to be (1.40 ± 0.02) x 10^4 $M^{-1}.s^{-1}$. All the other rate constants are independent from the metal concentration and were determined as (1.1 ± 0.9) s^{-1}, (0.7 ± 0.3) s^{-1} and (0.1 ± 0.04) s^{-1}, for k_2, k_3 and k_4, respectively. The evolution with time of each intermediate is showed in the next figure (figure IV.6).

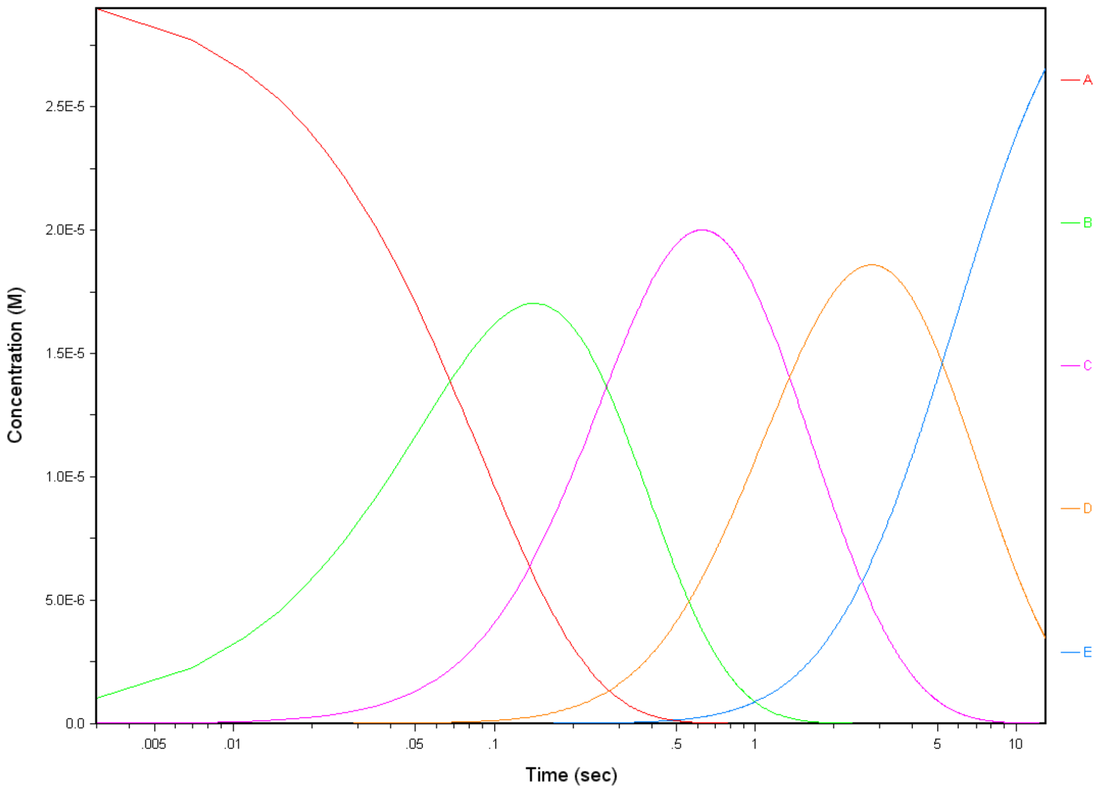

Figure IV. 6 – Species evolution with time of a 1:1 mixture (v/v) of 30 μM ApoRd with 840 μM $NiCl_2$, in 50 mM MES buffer pH 6.25. The concentration of the species was determined using the calculated rate constants for this assay.

The same studies were then performed with cobalt. Just like for the assays with nickel, with cobalt it was also possible to observe bands in the visible part of the spectrum. These bands were again similar to the previously described in the literature (figure IV.7)[4].

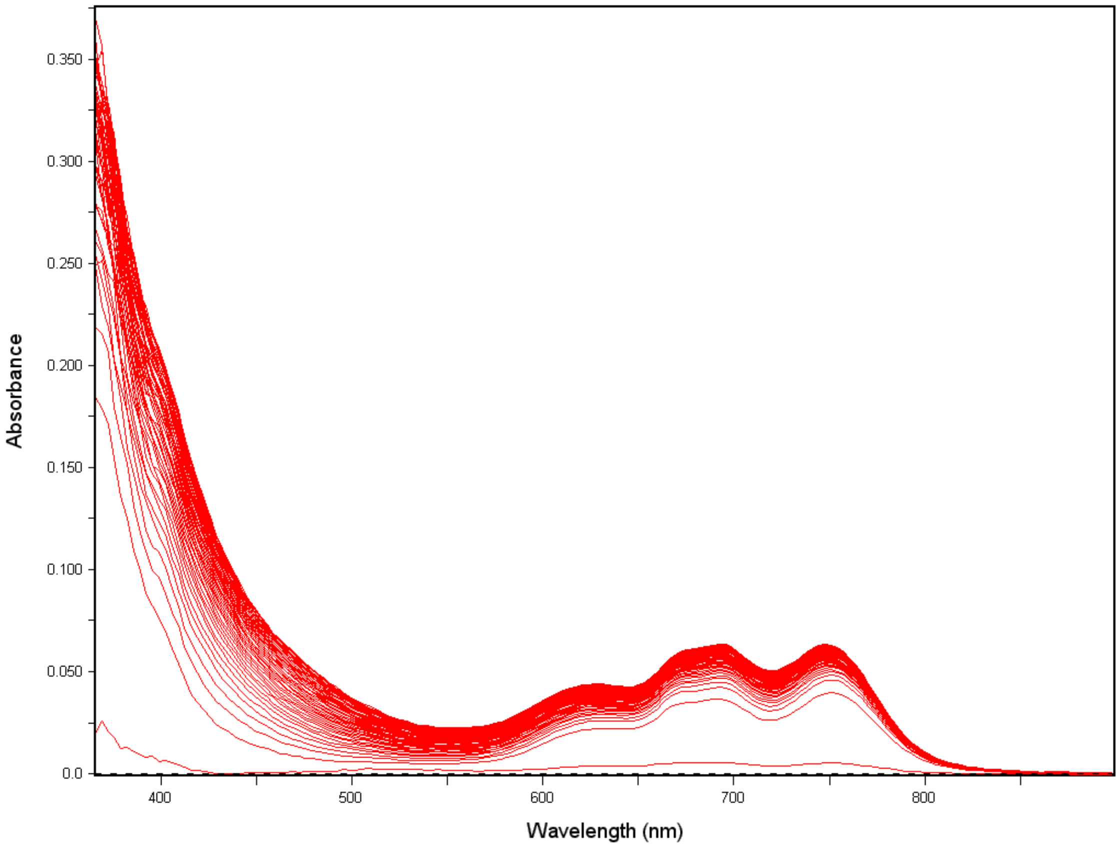

Figure IV. 7 - 2D Spectral evolution of a 1:1 mixture (v/v) of 30 μM ApoRd with 840 μM $CoCl_2$, in 50 mM MES buffer pH 6.25.

A 3D analysis was also performed in order to obtain a kinetic mechanism to fit the experimental data. The next figure (figure IV.8) represents a 3D image of one of the assays.

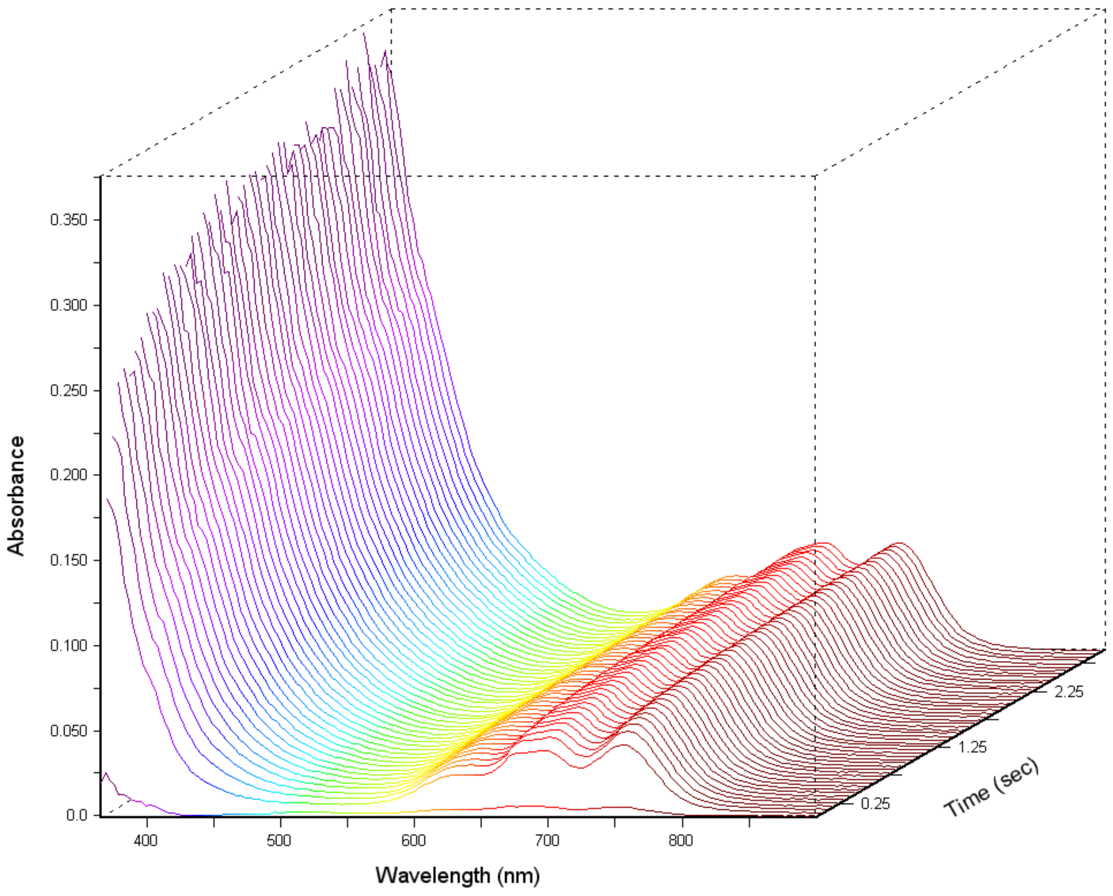

Figure IV. 8 - 3D Spectral evolution of a 1:1 mixture (v/v) of 30 μM ApoRd with 840 μM $CoCl_2$, in 50 mM MES buffer pH 6.25.

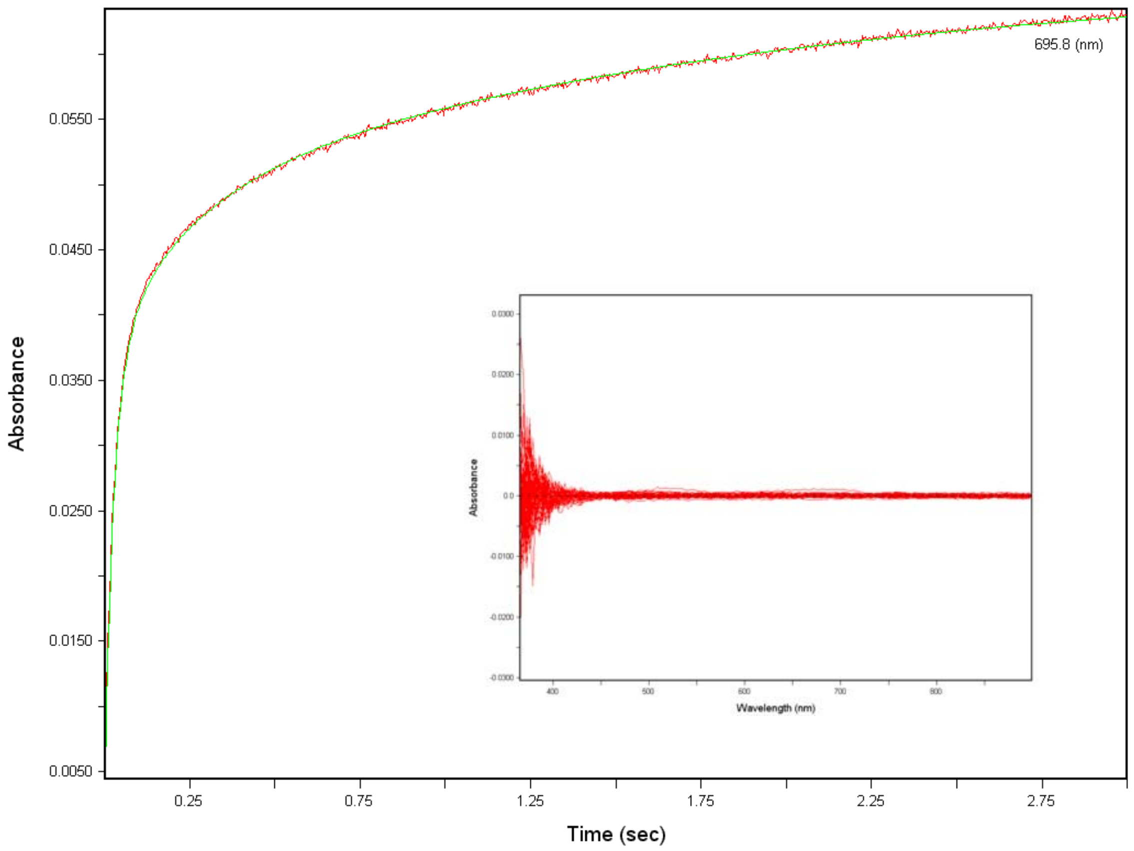

Figure IV. 9 - Kinetic trace of a 1:1 mixture (v/v) of 30 μM ApoRd with 840 μM $CoCl_2$, in 50 mM MES buffer pH 6.25. The green line represents the theoretical values obtained at this wavelength (696nm). The inset represents the residuals for the fit of the overall data.

Applying the obtained data to the previously described software, it was also possible to fit the data with four first order rate constants, as in the nickel assay. The first of the four constants is a pseudo-first order constant and as such it was plotted against the concentration of Co^{2+} (Fig.IV.10). The other constants were again independent of metal concentration and were determined to be (11± 3) s^{-1}, (1.2 ± 0.7) s^{-1} and (0.5 ± 0.03) s^{-1}, for k_2, k_3 and k_4, respectively.

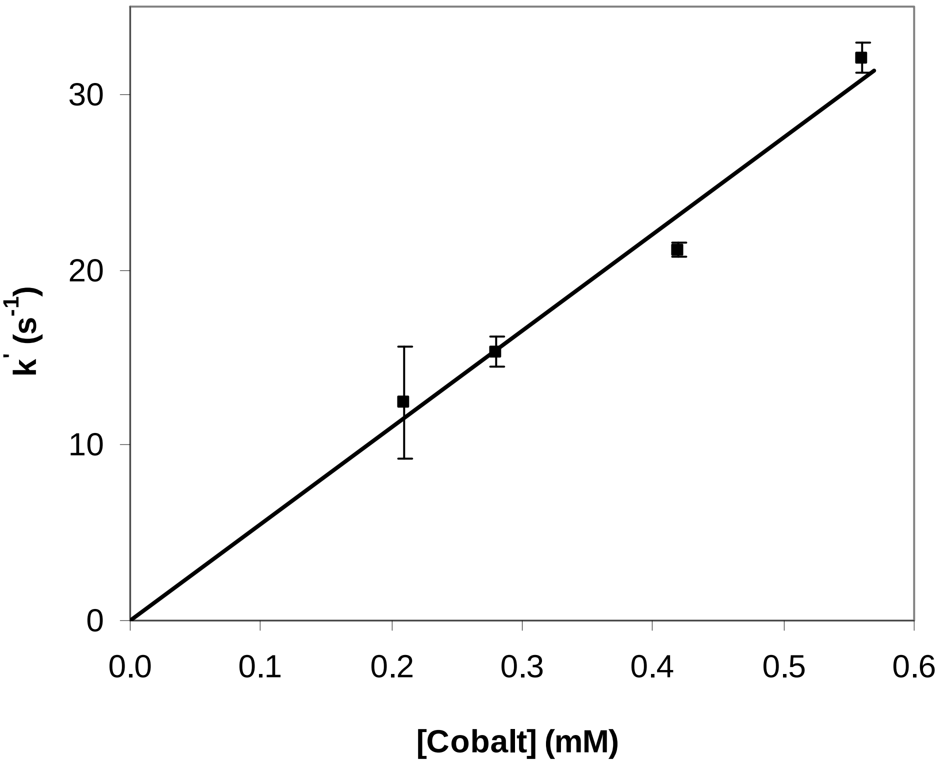

Figure IV. 10 - Metal concentration dependence for the calculated k'. The slope of the trend line indicates the second order rate constant for the first step.

From the presented plot, the second order rate constant corresponding to the first step of the reaction was determined to be (5.51 ± 0.15) x 10^4 $M^{-1}.s^{-1}$. Once again the evolution of each species in time was determined by the formation/decay rate constants. An example is show figure IV.11.

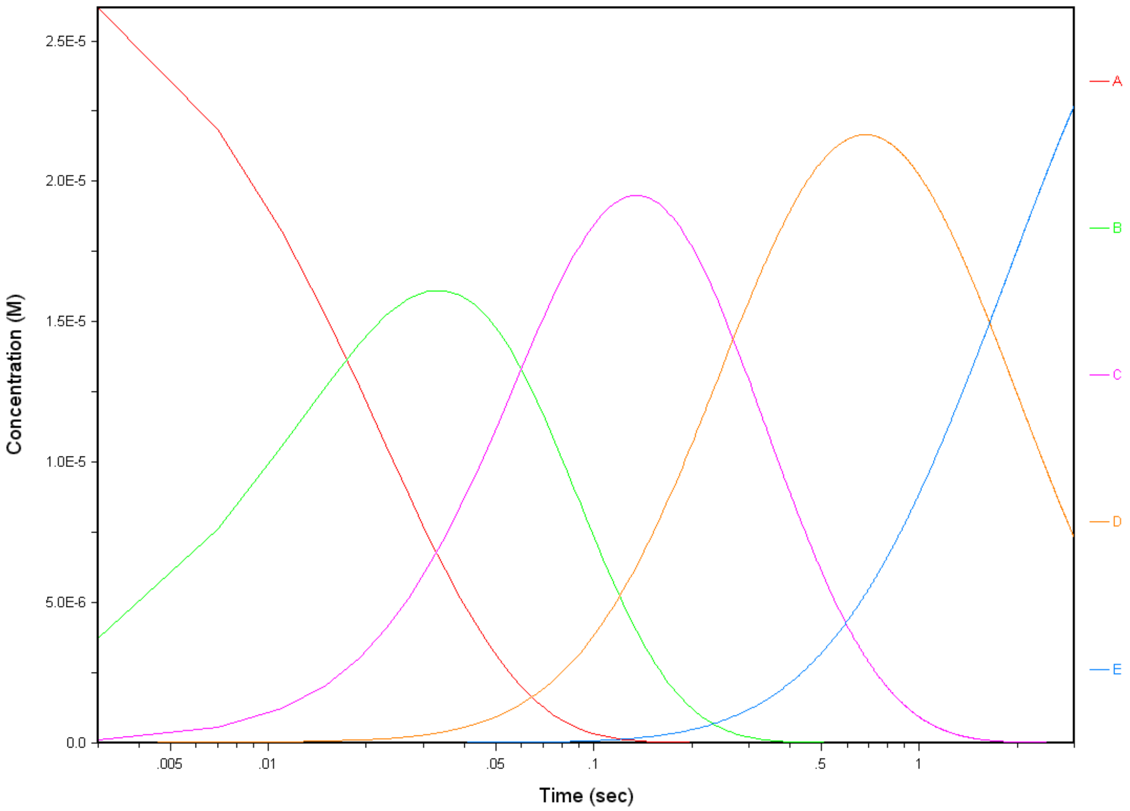

Figure IV. 11 - Species evolution with time of a mixture 1:1 (v/v) of 30 μM ApoRd with 840 μM $CoCl_2$, in 50 mM MES buffer pH 6.25. The concentration of the species was determined with the calculated rate constants for this assay.

For Fe^{2+} and Zn^{2+} (two other metals under study) no visible spectroscopic bands exist. For this reason the experimental procedure was slightly changed. In this case, the appearance of the cysteine-ligand charge transfer band (320nm) was used to follow the reaction and to obtain the kinetic data.

With this approach it is not possible to obtain spectral data of the intermediates, but it is enough to obtain kinetic data of metal incorporation. So, the evolution of a single wavelength was followed at 320 nm, corresponding to the cysteine charge transfer band[6]. For this purpose, MOS-250 (Bio-Logic™) was used instead of the Diode Array. This device is also connected to the observation head with optical fibers (Appendix A).

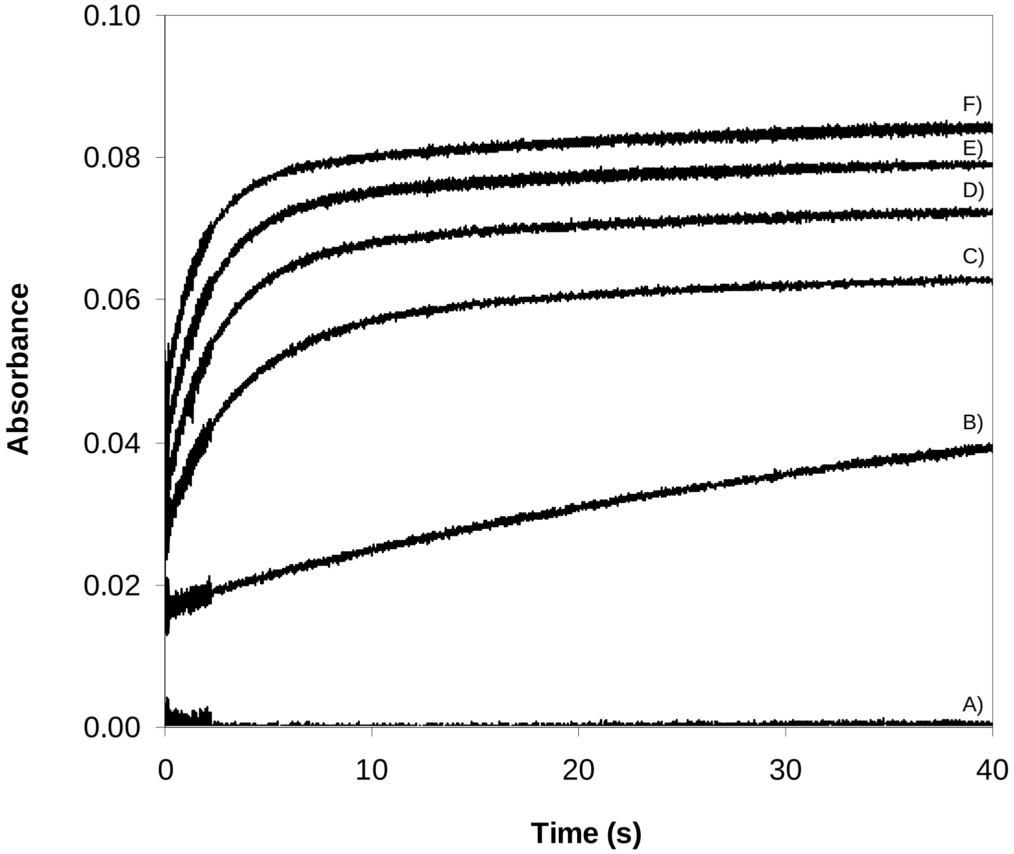

Figure IV. 12 – Kinetic traces followed at 320 nm of several ratios of protein/Fe^{2+} mixed 1:1 (v/v) in 50 mM MES buffer pH 6.25. The protein concentration was 30 μM and the iron varied from 0 to 700 μM; A) 0 μM, B) 175 μM, C) 263 μM, D) 350 μM, E) 467 μM and F) 700 μM.

The obtained data was fitted with only two first order rate constants, contrary to the previous four used for nickel and cobalt. As only a single wavelength was used to study the iron incorporation, the possibility of a 3D spectral analysis was eliminated. However, the obtained k' values were plotted against iron concentrations in the assays and the second order rate constant for the first step was calculated as being $(9.71 \pm 0.24) \times 10^2\ M^{-1}.s^{-1}$.

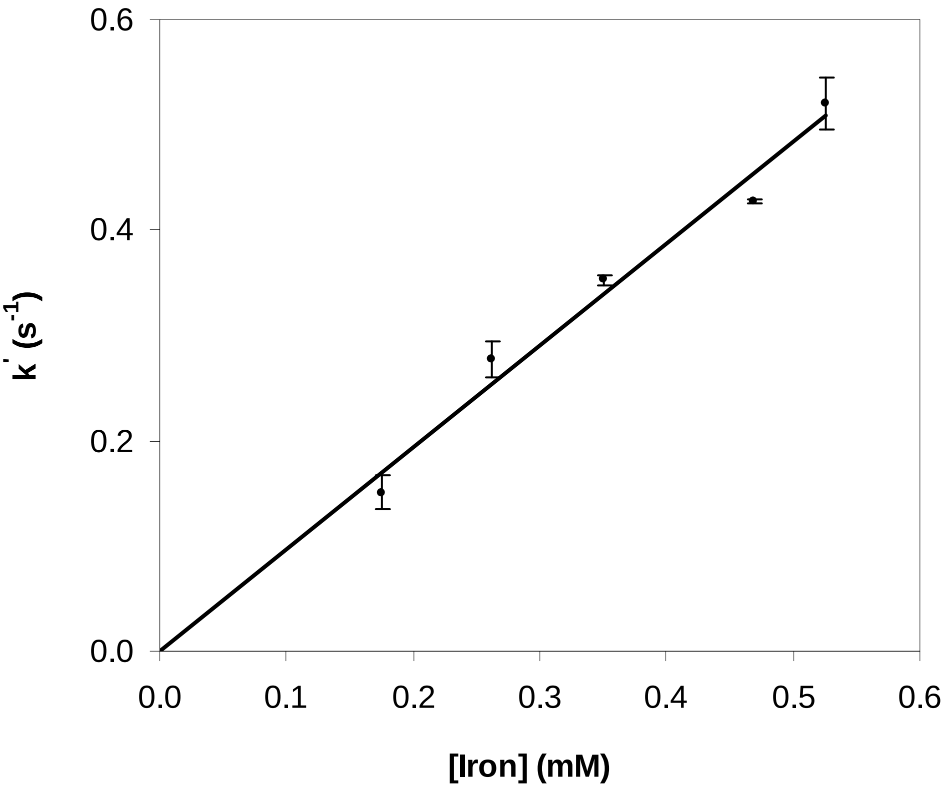

Figure IV. 13 - Metal concentration dependence for the calculated k'. The slope of the trend line indicates the second order rate constant for this step.

The same experiment was performed for Zn^{2+} incorporation. However, the obtained results were not reproducible and no values were calculated. It was only possible to conclude that the reaction is slower than for the other metals, needing more than 30 minutes to achieve the complete incorporation.

Table IV. 1 – Values of the rate constants obtained for the metal incorporation in the ApoRd

Metal	Rate Constants			
	k_1 ($M^{-1}.s^{-1}$)	k_2 (s^{-1})	k_3 (s^{-1})	k_4 (s^{-1})
Ni^{2+}	$(1.40 \pm 0.02) \times 10^4$	1.1 ± 0.9	0.7 ± 0.3	0.1 ± 0.04
Co^{2+}	$(5.51 \pm 0.15) \times 10^4$	11 ± 3	1.2 ± 0.7	0.5 ± 0.03
Fe^{2+}	$(9.71 \pm 0.24) \times 10^2$	0.06 ± 0.01	-	-

Looking at the data obtained, it is possible to assume that, apparently, rubredoxin does not incorporate all the metals with the same mechanism. There are changes in the reaction rate and also in the number of reaction steps. Apparently the Ni^{2+} and Co^{2+} incorporation involves three intermediate species, with four rate constants in a scheme such as, the one presented by Eq. IV.3.

$$A \xrightarrow{k_1} B \xrightarrow{k_2} C \xrightarrow{k_3} D \xrightarrow{k_4} E \qquad \text{Eq. IV.3}$$

On the other hand, Fe^{2+} incorporation follows, apparently, a different mechanism from cobalt and nickel, with only two rate constants observable. In a first approach this could mean that the apoprotein is able to bind the iron in only two steps, with only one intermediate. This reaction also needs more time than the one with other transition metals (cobalt and nickel) to be completed. Because of this, we could think that it is more difficult to incorporate iron than cobalt or nickel. However, from the biological point of view and according to the natural abundance of iron rubredoxin, the opposite seems to occur. Because for this metal there are no other Uv-Vis features than the one observed at 320 nm, it could be possible that the obtained data lacks sufficient information for a complete explanation of the iron center assembly. Another experimental approach was necessary to study this hypothesis. The fact that this is an iron protein allowed us the use of Mössbauer spectroscopy which is particularly suited to the study of ferrous iron centers.

IV.2.4 – Iron incorporation by apoprotein form of rubredoxin: Rapid Freeze-Quench ^{57}Fe Mössbauer spectroscopy

^{57}Fe Mössbauer spectroscopy proved to be very useful to understand and monitor iron containing proteins[7]. This technique is even more powerful when coupled to fast kinetic techniques like Rapid Freeze-Quench which enables the capture of reaction intermediates[8, 9]. In this particular case, these two techniques combined can provide clear information not only on the number of intermediates, but also on the reaction kinetics.

Since there are some experimental limitations, the experiment had to be changed in order to fulfil the needed requirements. The kinetic approach is no longer pseudo-first order, because for this experiment the initial concentrations of both apoprotein and metal were the same. As before, this experiment was also performed in anaerobic conditions (see Appendix B) and in 50 mM MES buffer pH 6.25.

In order to help with data analysis two samples were prepared to study the spectral features of the initial iron environment (free Fe^{2+} in buffer solution) and the final reaction product (^{57}Fe rubredoxin). The spectrum for the initial iron environment was fitted with a quadrupole doublet with an average ΔE_Q = 3.29mm/s and δ = 1.37 mm/s. These parameters correspond to a high-spin ferrous iron (S=2) coordinated either by oxygen or nitrogen ligands. This is in accordance with the fact that the iron ions are free in solution (aqua complex). This fact also justifies the abnormally large line width that indicates that the data should be fitted with more than one quadrupole doublet, due to the distribution of iron species in solution. The ^{57}Fe reconstituted rubredoxin was also fitted with a single quadrupole doublet with ΔE_Q = 3.25 mm/s and δ = 0.70 mm/s. These parameters correspond to a high-spin ferrous iron (S=2) coordinated by sulphur ligands, and they are in accordance with the previously published values for native, reduced as-isolated rubredoxins[10-12]. The next data was obtained for the samples generated in the RFQ experiment.

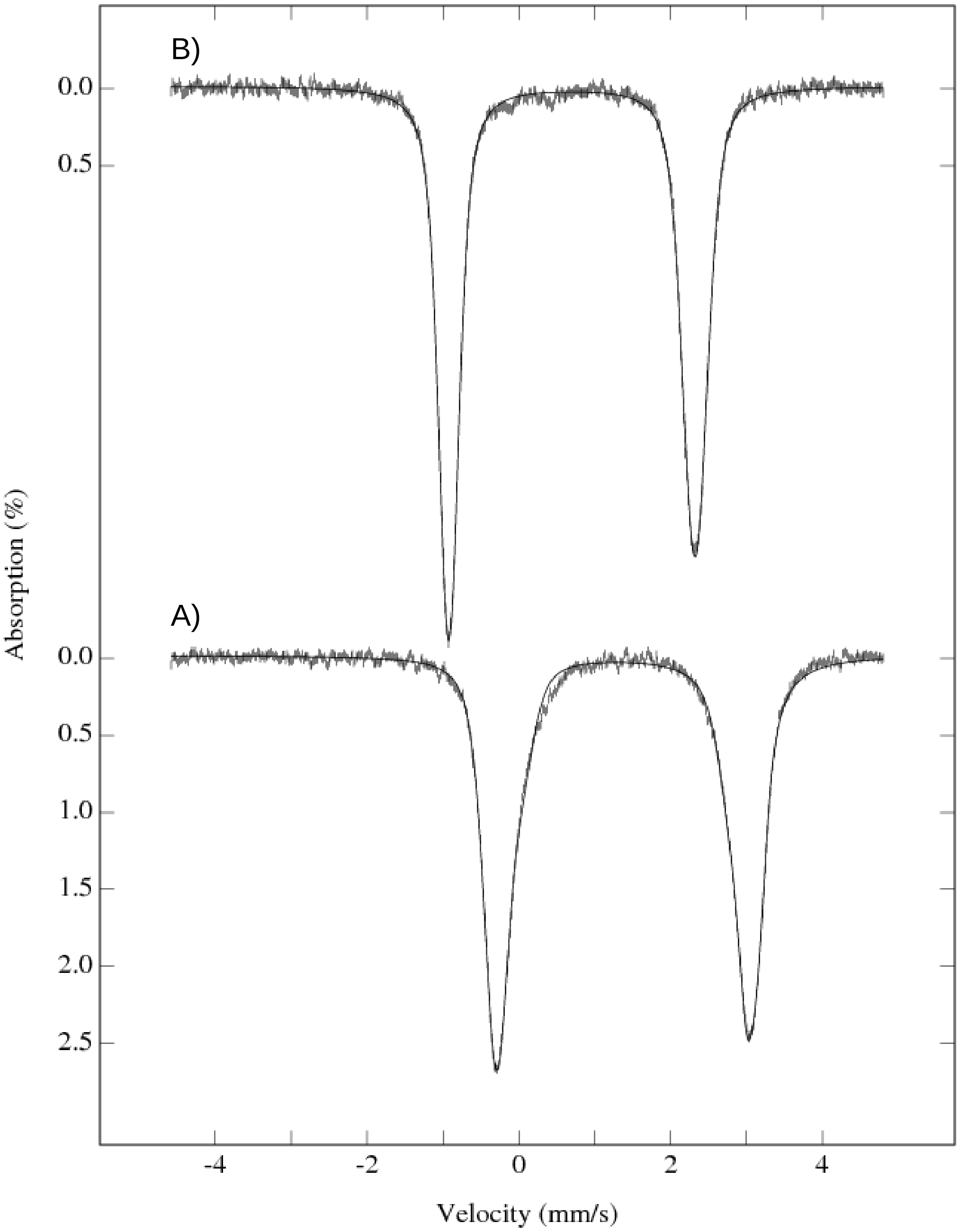

Figure IV. 14 – Mössbauer spectra of A) 700 μM ^{57}Fe in 50 mM MES buffer, pH 6.25 and B) 700 μM *Dg* rubredoxin reconstituted with ^{57}Fe in the same buffer. The solid lines represent the best fits for the experimental data.

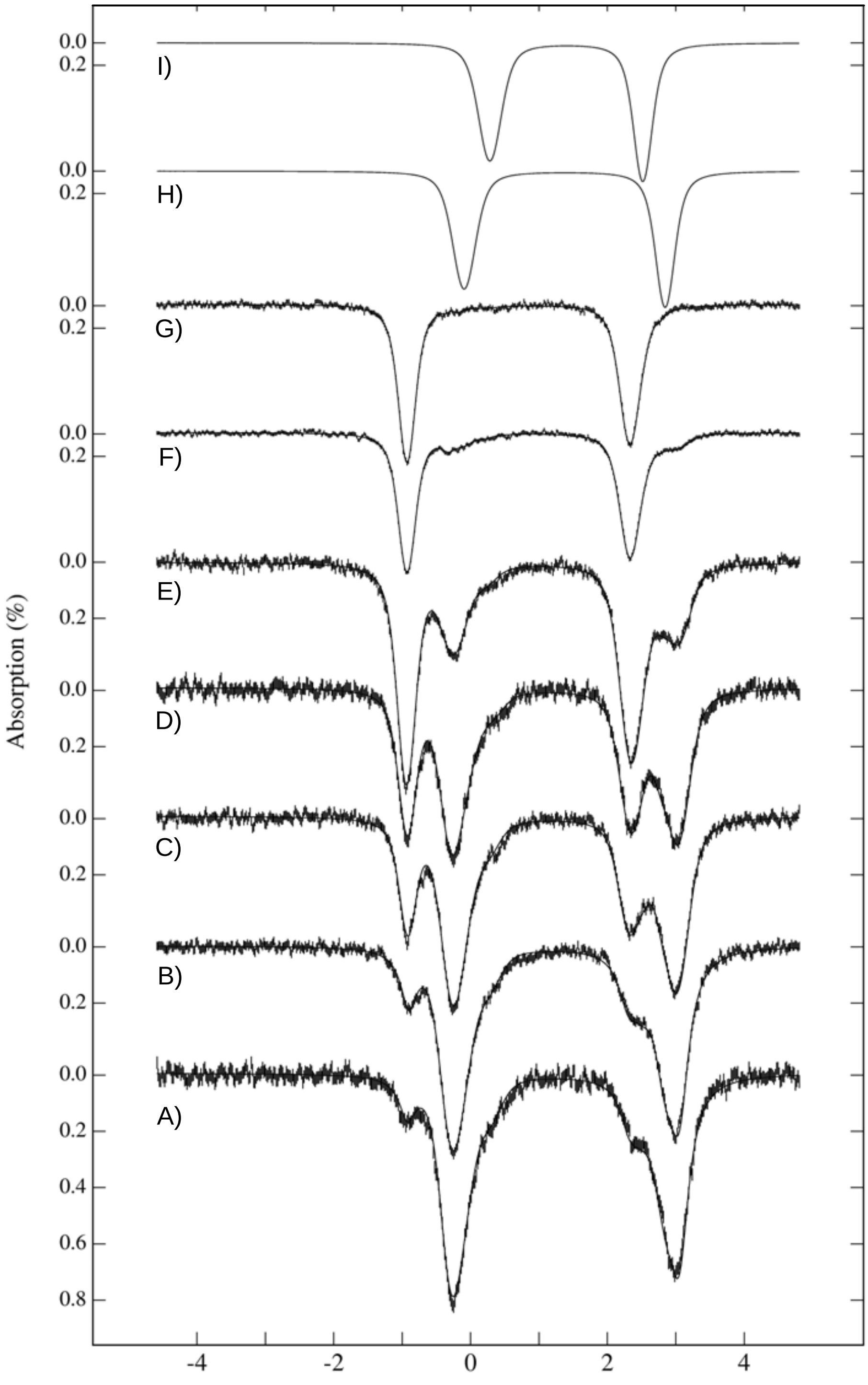

Figure IV. 15 – Mössbauer plot with the spectra obtained for the RFQ time course. A) 10 ms; B) 16 ms; C) 80 ms; D) 125 ms; E) 500 ms; F) 5 s; G) 1 min 15 s; H) Intermediate 1; I) Intermediate 2; The overlapped solid lines represent the best fits to the experimental data.

The analysis of the data obtained in the RFQ experiment revealed a three step reaction, with two intermediate species. In the table below are shown the parameters used to fit the experimental data. The evolution of each species with time is presented in the table IV.3.

Table IV. 2 – Parameters used to fit the Mössbauer spectra of the samples obtained in the rapid freeze-quench experiment.

	Species		
	I1	I2	Reduced Rubredoxin
δ (mm/s)	1.38 ± 0.02	1.40 ± 0.02	0.70 ± 0.01
ΔE_Q (mm/s)	2.93 ± 0.05	2.19 ± 0.02	3.26 ± 0.02
Γ	0.35 ± 0.03	0.34 ± 0.03	0.35 ± 0.02

Table IV. 3 – Percentage for species of table IV.2 in each sample studied

Sample	%			
	Fe^{2+}	Reduced Rubredoxin	I1	I2
10 ms	52	10	27	11
16 ms	50	15	25	10
80 ms	48	28	17	7
125 ms	42	37	15	6
500 ms	22	64	9	5
5 s	8	86	4	2
1 min 15 s	0	100	0	0

The values presented in table IV.2 show at least two different iron environments. One is similar to that observed in the iron solution, without the protein, and corresponds to a high-spin ferrous iron (S=2) coordinated either by oxygen or nitrogen ligands, with ΔE_Q ranging from 2 to 3 mm/s and δ always close to 1.4 mm/s. The other can be attributed to the reconstituted rubredoxin with ΔE_Q = 3.26 mm/s and δ = 0.70 mm/s, which correspond to a high-spin ferrous iron (S=2) coordinated by sulphur.

IV.3 - Discussion

Metallic centers have an enormous relevance in biology. They are responsible for several functions that range from catalysis to electron transfer. The difference between all the centers and their function must lie on its nature (metal ion and coordination). So, how does Nature “decide” which metal to incorporate in a certain cluster/protein? Maybe studying the incorporation of a certain metal in well characterized proteins will help to understand why a certain metal ion is “chosen” instead of another.

In this case an iron center was studied. The iron centers represent only one example, even though they are associated with several types of reactions/mechanisms. Rubredoxin, for example, is normally associated with electron transfer[2, 3, 5, 13].

The data presented in this chapter reveal some apparently unexpected results. Since the native protein is an iron protein, it was expected that from all the studied metals, the fastest to be incorporated in the protein was iron. However, the data obtained by stopped-flow pointed, in a first approach, not only to a faster process for incorporation reactions of both nickel and cobalt, but also to a different mechanism between these two metal ions when compared to iron.

With the conditions used in this experiment, cobalt and nickel follow a four consecutive step mechanism, where the first rate constant is dependent on the reagents’ concentration (second order). Despite being difficult to assign the obtained rate constants to a specific path in the metal incorporation, it is possible to assume that, in these cases (cobalt and nickel), the metal binds to the protein (to one or more cysteine residues) in the first step. The following steps can be attributed either to the binding of the other cysteines or to some sort of conformational change.

On the other hand, the stopped-flow data collected for iron incorporation showed a mechanism defined by only two rate constants. The first remained dependent on the reagents' concentration, and the second remained independent. These data could point to a different pathway for iron incorporation. Also, the obtained values were much smaller than for cobalt and nickel.

However, the data obtained from the rapid freeze-quench Mössbauer brought some important aspects to the forefront. Despite the differences in the experimental procedure, the data obtained indicated not only to the presence of at least two intermediate species, but also a fast appearance of a first intermediate (27 % of the total in the first 10 ms).

Another interesting aspect lies in the values obtained from the fit of the Mössbauer data. The intermediate species parameters point to a high-spin ferrous iron coordinated by either oxygen or nitrogen (similar to what was found for iron solution) which means, in a first approach, that the iron is not coordinated by the cysteine residues. These parameters are also different from the ones previously published by Yoo and coworkers, referring to the C9S and C42S rubredoxin mutants from *Clostridium pasteurianum*. In these proteins the metallic center was modified in order to have one cysteine less as a ligand for iron. As a result, in that work two different species were reported, A and B, that were characterized and presented ΔE_Q = 2.95 mm/s and δ = 0.79 mm/s for form A and ΔE_Q = -3.27 mm/s and δ = 0.79 mm/s for form B[10].

Thus, a possible explanation could be related to some kind of "chelating" behavior from apoRd which removes the iron from the solution and goes through several conformational adjustments until it reaches its final structure. As it is difficult to assign the steps obtained with cobalt and nickel, maybe the process is similar and the obtained rate constants for the mechanism kinetically describe the process.

The fact that rubredoxin has only one tryptophan in its sequence makes possible the use of other techniques like stopped-flow coupled to fluorescence, for example, to understand if there are conformational adjustments during metal incorporation[14, 15].

Therefore, since it is not possible to assume large differences between the incorporation of the studied metals, it is possible to assume that in Nature the “choice” for iron instead of other metal can be related to other properties of this type of centers, like redox potentials for example, that favor the reactions in which they are involved. Thus, in a biological approach, a cobalt-rubredoxin or a nickel-rubredoxin, could not be adapted in order to accomplish the role in the cell metabolism.

Besides, this study only aimed the metal incorporation by the protein, meaning that there is not data concerning the stability of the rubredoxins formed (cobalt and nickel), and the fact that they are faster in the metal incorporation does not necessarily mean that they are more stable. In addition, an unstable behavior of these forms could also be an explanation for the use of iron instead of these metals in the native protein.

IV.4 – References

[1] A.S. Pereira, P. Tavares, F. Folgosa, R.M. Almeida, I. Moura, J.J.G. Moura, Superoxide reductases, European Journal of Inorganic Chemistry (2007) 2569-2581.

[2] J.V. Rodrigues, I.A. Abreu, L.M. Saraiva, M. Teixeira, Rubredoxin acts as an electron donor for neelaredoxin in Archaeoglobus fulgidus, Biochem Biophys Res Commun 329 (2005) 1300-1305.

[3] E.D. Coulter, D.M. Kurtz, Jr., A role for rubredoxin in oxidative stress protection in Desulfovibrio vulgaris: catalytic electron transfer to rubrerythrin and two-iron superoxide reductase, Arch Biochem Biophys 394 (2001) 76-86.

[4] I. Moura, M. Teixeira, J. LeGall, J.J. Moura, Spectroscopic studies of cobalt and nickel substituted rubredoxin and desulforedoxin, J Inorg Biochem 44 (1991) 127-139.

[5] F. Auchere, S.R. Pauleta, P. Tavares, I. Moura, J.J. Moura, Kinetics studies of the superoxide-mediated electron transfer reactions between rubredoxin-type proteins and superoxide reductases, J Biol Inorg Chem 11 (2006) 433-444.

[6] M.J. Winter, d-Block chemistry, Oxford University Press, 1994.

[7] E. Munck, Mossbauer spectroscopy of proteins: electron carriers, Methods Enzymol 54 (1978) 346-379.

[8] J.M. Bollinger, Jr., W.H. Tong, N. Ravi, B.H. Huynh, D.E. Edmondson, J.A. Stubbe, Use of rapid kinetics methods to study the assembly of the diferric-tyrosyl radical cofactor of E. coli ribonucleotide reductase, Methods Enzymol 258 (1995) 278-303.

[9] N. Ravi, J.M. Bollinger, B.H. Huynh, D.E. Edmondson, J. Stubbe, Mechanism of Assembly of the Tyrosyl Radical-Diiron(Iii) Cofactor of Escherichia-Coli Ribonucleotide Reductase .1. Mossbauer Characterization of the Diferric Radical Precursor, J. Am. Chem. Soc. 116 (1994) 8007-8014.

[10] S.J. Yoo, J. Meyer, C. Achim, J. Peterson, M.P. Hendrich, E. Munck, Mossbauer, EPR, and MCD studies of the C9S and C42S variants of Clostridium pasteurianum rubredoxin and MDC studies of the wild-type protein, J Biol Inorg Chem 5 (2000) 475-487.

[11] I. Moura, B.H. Huynh, R.P. Hausinger, J. Le Gall, A.V. Xavier, E. Munck, Mossbauer and EPR studies of desulforedoxin from Desulfovibrio gigas, J Biol Chem 255 (1980) 2493-2498.

[12] C. Schulz, P.G. Debrunner, Rubredoxin, a simple iron-sulfur protein: its spin Hamiltonian and hyperfine parameters Journal de Physique Colloques 37 (1976) 153 - 158.

[13] F. Auchere, R. Sikkink, C. Cordas, P. Raleiras, P. Tavares, I. Moura, J.J. Moura, Overexpression and purification of Treponema pallidum rubredoxin; kinetic evidence for a superoxide-mediated electron transfer with the superoxide reductase neelaredoxin, J Biol Inorg Chem 9 (2004) 839-849.

[14] M. Frey, L. Sieker, F. Payan, R. Haser, M. Bruschi, G. Pepe, J. LeGall, Rubredoxin from Desulfovibrio gigas. A molecular model of the oxidized form at 1.4 A resolution, J Mol Biol 197 (1987) 525-541.

[15] M. Bruschi, The amino acid sequence of rubredoxin from the sulfate reducing bacterium, Desulfovibrio gigas, Biochem Biophys Res Commun 70 (1976) 615-621.

Methods

A.1 – *E.coli* BL21(DE3) transformation protocol

The transformation protocol used in this work was based on the one recommended by the manufacturer[1]. It will be briefly described in this section.

1. Thaw the competent cells on ice.

2. Aliquot the cells in three prechilled eppendorf tubes.

3. Add to each tube 1.7 μL of a freshly prepared sterile β-mercaptoethanol solution (1:10 dilution). Swirl the tubes gently.

4. Incubate the reactions on ice for 10 minutes, swirling gently every two minutes.

5. Add the DNA desired for the transformation to each eppendorf following the table below.

Table A. 1 - Volumes used for transformation

	Reaction	Positive control	Negative control
Plasmid	3-4 μL	-	-
pUC18	-	1 μL	-
H_20 Sterile	-	-	1 μL

6. Incubate the reactions on ice for 30 minutes.

7. Preheat SOC medium (see A.5.3) in a 42 ºC water bath. This medium will be used in step 10.

8. Heat-shock each transformation reaction at 42 ºC for 42 seconds. **This is a critical step, every condition of temperature and time must be exactly followed.**

9. Incubate the reactions on ice for 2 minutes.

10. Add 450 μL of SOC medium to each eppendorf and incubate for 1 hour at 37 ºC and 225 rpm.

11. Using a sterile spreader, spread 3 different volumes of the grown cells (such as 50, 100 and 200 μL) onto LB-Agar plates supplemented with 0.1 mg/mL ampicillin. For positive and negative control, plate only one volume, such as 200 μL.

12. Incubate the plates overnight at 37 ºC.

When using this protocol it is expected to obtain enough colonies for use in the next steps of overexpression.

A.2 – SDS-PAGE electrophoresis: Solutions and methods

The sodium dodecyl sulfate polyacrylamide gel electrophoresis (SDS-PAGE) is a technique widely used for both determination of protein molecular mass and to evaluate the purity of protein fractions. It is based on the technique described by Laemmli and in this thesis it was used mainly for purity assessment[2]. The following tables describe the solutions used for this technique.

Table A. 2 – Volumes of each solution used for the SDS-PAGE gel electrophoresis.

Solution	Stacking gel	Running gel				
	5 % of Acrylamide (volumes in mL)	% of Acrylamide (volumes in mL)				
		5	7.5	10	12.5	15
I	-	0.75	0.75	0.75	0.75	0.75
II	0.45	-	-	-	-	-
III	0.30	1.25	1.33	1.67	2.08	2.5
10% SDS	0.018	0.05	0.05	0.05	0.05	0.05
dH_2O	0.94	2.93	2.85	2.51	2.1	1.66
10% PSA	13.5 μL	38 μL	38 μL	38 μL	38 μL	38 μL
TEMED	2 μL	2.5 μL	2.5 μL	2.5 μL	2.5 μL	2.5 μL

Table A. 3 – Stock solutions used for the SDS-PAGE gel electrophoresis

Solution		Reagents	Amount	Obs.
I	Running gel Buffer	2.5 M Tris Base	30.3 g	pH 8.8-9.0
		37% HCl	until pH8.8	
		H_2O	until 100 mL	
II	Stacking gel buffer	0.5 M Tris Base	6.06 g	pH 6.6-6.8
		37% HCl	until pH 6.8	
		H_2O	until 100 mL	
III	Acrylamide/ Bisacrylamide (30:0.8)	Acrylamide	30 g	-
		Bisacrylamide	0.8 g	
		H_2O	Up to 100mL	
IV	10% SDS	SDS	10 g	-
		H_20	Up to 100 mL	
V	10 % APS	Ammonium Persulfate	0.5 g	Prepare prior to use
		H_2O	Up to 5 mL	
VI	Tris-Glycine Buffer	0.25 M Tris Base	30.3 g	pH 8.3 Dilute 1:10 prior to use
		1.92 M Glycine	144.1 g	
		SDS	10 g	
		H_2O	Up to 1000 mL	
VII	Sample Buffer	Solution II	5 mL	Add 1:1 to the sample
		10% SDS	8 mL	
		b-Mercaptoethanol	1 mL	
		Glycerol	2 mL	
		Bromophenol Blue	4 mg	
		H_2O	Up to 20 mL	
VIII	Coomassie Brilliant Blue Staining	Coomassie Blue R-250	1 g	-
		Glacial Acetic Acid	15 mL	
		Methanol	90 mL	
		H_2O	Up to 200 mL	
IX	Distaining solution	Glacial Acetic Acid	75 mL	-
		Methanol	450 mL	
		H_2O	Up to 1000 mL	

A.3 – Protein quantification: Lowry method

Nowadays, there are several methods available for protein quantification. In this work the method described by Lowry and coworkers was used[3] .

1. Prepare three protein samples with different concentrations into a final volume of 0.1 mL.
2. Add to each sample 1 mL of solution C and incubate for 10 minutes.
3. Add 0.1 mL of solution D, mix and incubate for 30 minutes.
4. Measure the absorbance at 580, 680 and 750 nm.

The solutions used in this method are described in the table below. A bovine serum albumin (BSA solution 2 mg/mL purchased from Sigma®) was used as standard.

Table A. 4 - Solutions used for Lowry method

Solution	Description	Preparation details
A	2% Na_2CO_3 in 0.1 N NaOH	2 g of 2% Na_2CO_3 + 0.4g of NaOH in 100 mL of H_20
B1	1% $CuSO_4.5H_20$	1 g of $CuSO_4.5H_20$ in 100 mL of H_20
B2	2% Sodium tartarate	2 g of sodium tartarate in 100 mL of H_20
B	1:1 mixture of B1 and B2	- (prepared prior to use)
C	Alkaline copper solution	50 mL of A + 1 mL of B (prepared prior to use)
D	Folin reagent 1:1 diluted	- (prepared prior to use)

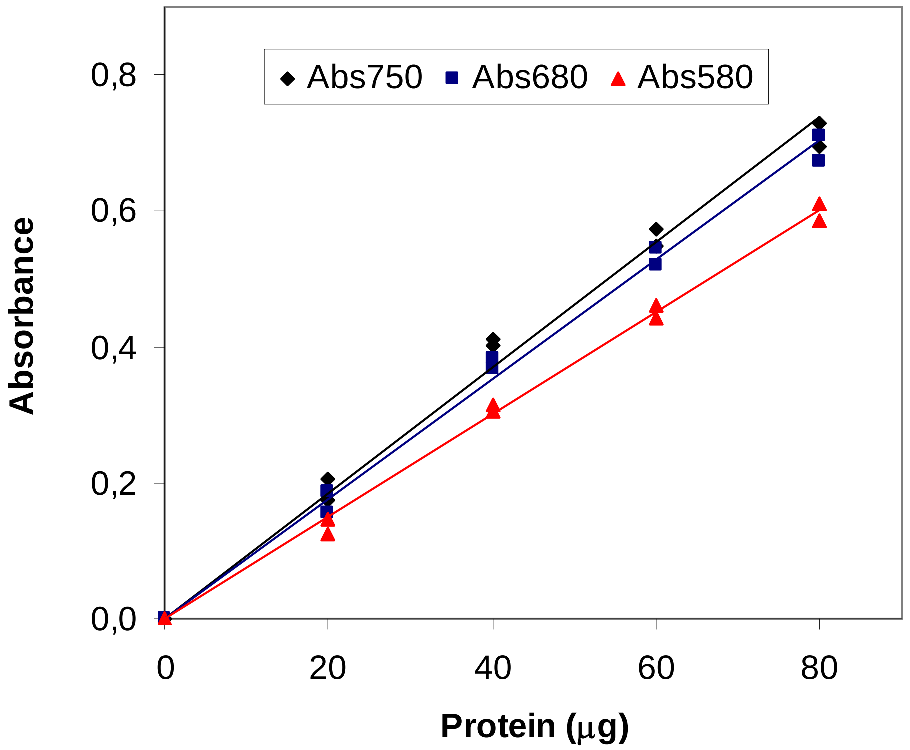

Figure A. 1 – Typical calibration curve obtained with the BSA standard for the Lowry method.

A.4 – Growth media description: LB, M9 and SOC

All the proteins used in the work described in this thesis were obtained using overexpression systems. In this section all the growth media used for this work will be described. All the volumes mentioned are for 1 L of culture medium.

A.4.1 – Luria-Bertani broth

The Luria-Bertani broth is widely used for bacterial growth. It provides a large amount of nutrients and other important elements for cell growth and protein overexpression.

Table A. 5 – Reagents used for LB medium preparation

Reagent	Amount per Liter
NaCl	10 g
Tryptone	10 g
Yeast extract	5 g

The solution is made with deionized water and the pH is adjusted to 7.0 with a concentrated solution of NaOH. The solution is finally autoclaved for 15min at 121 ºC to keep sterile. The LB-Agar solution used for plates has the same preparation but with addition of 20 g of agar.

A.4.2 – M9 growth medium

The necessity of controlling the growth conditions sometimes requires the use of a defined growth media. In this thesis the chosen medium was the M9. This medium allows us to control not only the amount but also the type of metal ions available for cell growth.

Table A. 6 – Solutions used to supplement the M9 medium.

M9 Salts (10x)		Vitamin (200x)	
Reagent	Amount per Liter	Reagent	Amount per Liter
Na_2HPO_4	128 g	Thiamine -HCl	1 g
KH_2PO_4	30 g	Biotin	0.2 g
NH_4Cl	10 g	Choline chloride	0.2 g
NaCl	5 g	Folic acid	0.2 g
		Nicotinic acid	0.2 g
		Calcium pantothenate	0.2 g
		Pyridoxine	0.2 g
		Riboflavin	0.02 g

The M9 salts should be diluted with Millipore® grade water (100 mL M9 salts plus 880 mL of water) and autoclaved. The vitamin solution should be filtered sterile and stored at 4 ºC.

Table A. 7 - Reagents used for M9 medium preparation

M9 Medium

Reagent	Amount per Liter
1M $MgSO_4$	1 mL
0.1M $CaCl_2$	1 mL
20% Glucose	20 mL
0.1% Thiamine -HCl	0.5 mL
Vitamin (200x)	5 mL
0.1M Metal ion solution	1 mL
100 mg/mL Ampicillin	1 mL

These reagents should be added to the diluted M9 salts solution prior to use. The amount of "metal ion solution" used should take into account the solubility of the metal and its toxicity to the cells. All the solutions used should be kept sterile.

A.4.3 – SOC medium

Like LB, the SOC is a rich culture medium that provides a large amount of nutrients important for the fast cell growth. As such, it is widely used in transformation procedures, were a fast cell growth is important to obtain good results.

Table A. 8 - Reagents used for SOC medium preparation

Reagent	Amount per Liter
Tryptone	20 g
Yeast extract	5 g
NaCl	0.5 g
1M $MgCl_2$	10 mL
1M $MgSO_4$	10 mL
20% Glucose	20 mL

The solution should be autoclaved before the addition of $MgCl_2$, $MgSO_4$, and glucose. At the end it should be filtered and kept sterile.

A.5 – Buffer solutions

All the buffer solutions used in this work were prepared by dilution from the correspondent 1 M stock solution at room temperature. The stock solutions and the buffers used for HPLC were filtered (45 μm filter pore size) prior to use.

A.5.1 – Tris-HCl buffer

In order to prepare 1000 mL of a 1 M of Tris-HCl buffer solution, 121 g of Tris(hydroxymethyl)aminomethane (purchased from Sigma®) powder was dissolved in about 800 mL of deionized water. Then, a certain amount of concentrated HCl solution (37% (w/v)) was added in order to obtain the desired pH value. Finally, the pH value was verified and the volume was adjusted to 1000 mL. The table below shows the volumes of hydrochloric acid necessary to obtain the desired pH value in a 1 M buffer solution.

Table A. 9 – Volumes of HCl 37% (w/v) added to obtain the desired pH value

Volume Added (mL)	Final pH
68.5	7.4
63.6	7.6
53.8	7.8
44.4	8.0

A.5.2 – Phosphate buffer

In order to prepare 100 mL of a 1 M solution of phosphate buffer, two solutions were prepared (solution A and B).

Solution A is a 1 M solution of monobasic potassium phosphate (139 g in 1000 mL of H_2O). Solution B is a 1 M solution of dibasic potassium phosphate (268 g in 1000 mL of H_2O). These two solutions were mixed in different ratios to obtain a final 1 M solution of phosphate buffer with the desired pH.

Table A. 10 – Volume ratios used to obtain a 1 M solution of phosphate buffer at a certain pH

Volume A (mL)	Volume B (mL)	Final pH
19.0	81.0	7.4
13.0	87.0	7.6
8.5	91.5	7.8
5.3	94.7	8.0

A.5.3 – MES Buffer

The 4-morpholineethanesulfonic acid (MES) sodium salt was used as buffer for the rubredoxin metal incorporation experiments. This salt can serve as an efficient buffer for pH values ranging from 5.5 to 6.7. This buffer was prepared by adding 21.72 g of MES in 100 mL of Millipore® grade water, up to 1 M final concentration. The final pH was adjusted with an HCl 37 % (w/v) solution.

Like for the other buffers, all the solutions used were made by dilution of the 1M solution with Millipore® grade water.

A.6 – References

[1] Stratagene, BL21(DE3) Competent Cells, Instruction Manual, Stratagene, La Jolla, 2004.

[2] U.K. Laemmli, Cleavage of structural proteins during the assembly of the head of bacteriophage T4, Nature 227 (1970) 680-685.

[3] O.H. Lowry, N.J. Rosebrough, A.L. Farr, R.J. Randall, Protein measurement with the Folin phenol reagent, J Biol Chem 193 (1951) 265-275.

Equipment

As was mentioned before, for this work several setups were used in order to achieve the best experimental conditions. For this purpose, some commercial equipment had to be customized. This customization will be briefly described in this Appendix.

B.1 – Stopped-Flow apparatus: aerobic and anaerobic setup

All the stopped-flow experiments were performed using a Bio-Logic apparatus. Our equipment is composed by two SFM-300 modules (each one composed by three syringes and three independent stepping motors, one per syringe), powered by a MPS-60 unit and controlled by a PC with BioKine32 v.4.45 software provided by Bio-Logic. One of these SFM-300 modules is kept under anaerobic conditions inside a glove box (mBraun UniLab, less than 1 ppm of oxygen) to achieve the best conditions for the experiments. The SFM-300 module also allows temperature control, an important feature that was used in all the procedures and was particularly important for the electron transfer experiments where the temperature was lowered to 10 ºC to reduce the velocity of the reaction.

In the experiments described in this thesis two detection methods were used coupled to the stopped-flow equipment. The first was a Diode Array spectrophotometer (TIDAS, J&M) with 256 diodes ranging from 300 to 1100 nm. This diode array is able to collect as many as 3690 spectra at 0.8 ms/spectrum. For better signal to noise ratio, larger integration times were used (never lower than 1 ms/spectrum). This equipment is particularly useful when 3D analysis is needed.

The second detection apparatus used was a MOS-250 (Bio-Logic). This is a fast UV-Vis spectrophotometer that is able to cover an emission spectral range from 220 to 1010 nm. This equipment is able to work in three different modes: as a transient recorder, a scanning spectrophotometer and a chart recorder. However, it was only used as a transient recorder. In this mode it is able to collect data (single wavelength at a time) from 50 μs to 1000 s per point.

Both equipments are connected via optical fibers to the observation head (where the cuvette is placed) of SFM-300 and are controlled with the same software. The anaerobic experiments were performed inside a glove box (UniLab model from mBraun) which was adapted for this purpose. The modifications included a set of custom made doors specially built (ERT, Equipamentos e Reparações Técnicas, Lda) to allow the total electronic control of the equipment from outside.

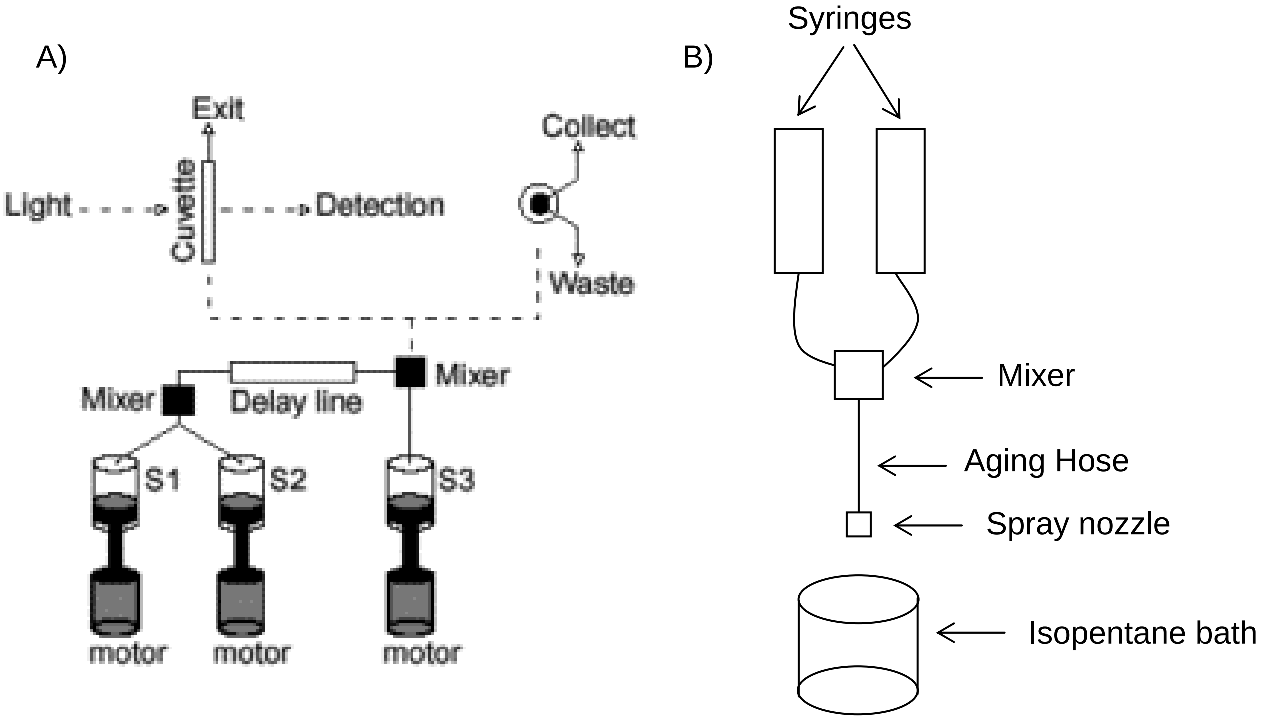

Figure B. 1 – A) Scheme of Bio-Logic SFM300 module used for the stopped-flow and rapid freeze-quench experiments. Adapted from [1]. B) Generic scheme of a rapid freeze -quench apparatus.

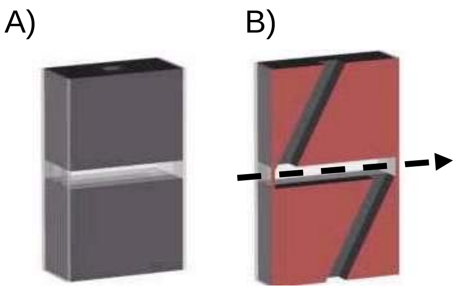

Figure B. 2 – A) Scheme of the Bio-Logic TC 100/10 cuvette, used for the stopped-flow experiments. B) Vertical cut of the TC 100/10 cuvette. The dashed arrow represents the light path. Adapted from [1].

B.2 – Rapid Freeze-Quench apparatus: aerobic and anaerobic setup

The RFQ setup installed in Chemistry Department of Faculdade de Ciências e Tecnologia da Universidade Nova de Lisboa consists of a set of drive syringes, RFQ module, a power unit, a computer and a quenching bath.

In order to perform the rapid freeze-quench experiments presented in chapter 4 of this thesis, it was necessary to fit the RFQ module (Update Instrument Inc) to our stopped-flow machine and isopentane bath equipments (Bio-Logic). The RFQ module consist of a set of small nylon hoses that connect the SFM-300 module to a mixing chamber, a set of different aging hoses that allow different reaction times and a spray nozzle which is used to vaporize the sample into an isopentane bath. This cooling bath is kept at -140 ºC with a liquid nitrogen refrigerated system.

Therefore, the RFQ experiment involves mixing two or three reagents rapidly and efficiently through the mixing chamber, allowing the reaction to proceed for a specific period of time (from 10 millisecond to hours depending on the volume of the tube), freeze-quenching the reaction mixture by squirting it into the quenching bath and packing the frozen sample into a Mössbauer sample cell. A similar setup was previously described by Ravi and coworkers[2].

The anaerobic apparatus is based on the one described above but in this case only the aging hose and the isopentane bath stand outside the glove box, meaning that all the other manipulations are performed in anaerobic conditions. Because the aging hose is accessible from the outside it is simple to change it in order to obtain different reaction times. Another advantage of this equipment is the fact that it is totally controlled from the outside.

Like for the anaerobic stopped-flow experiments, another set of structural modifications was performed in the glove box in order to allow the equipment control/communication from the outside. These modifications consisted in a set of custom made doors specially designed and built (ERT, Equipamentos e Reparações Técnicas, Lda) to allow the collection of the sample outside the glove box. The following figure illustrates the setup.

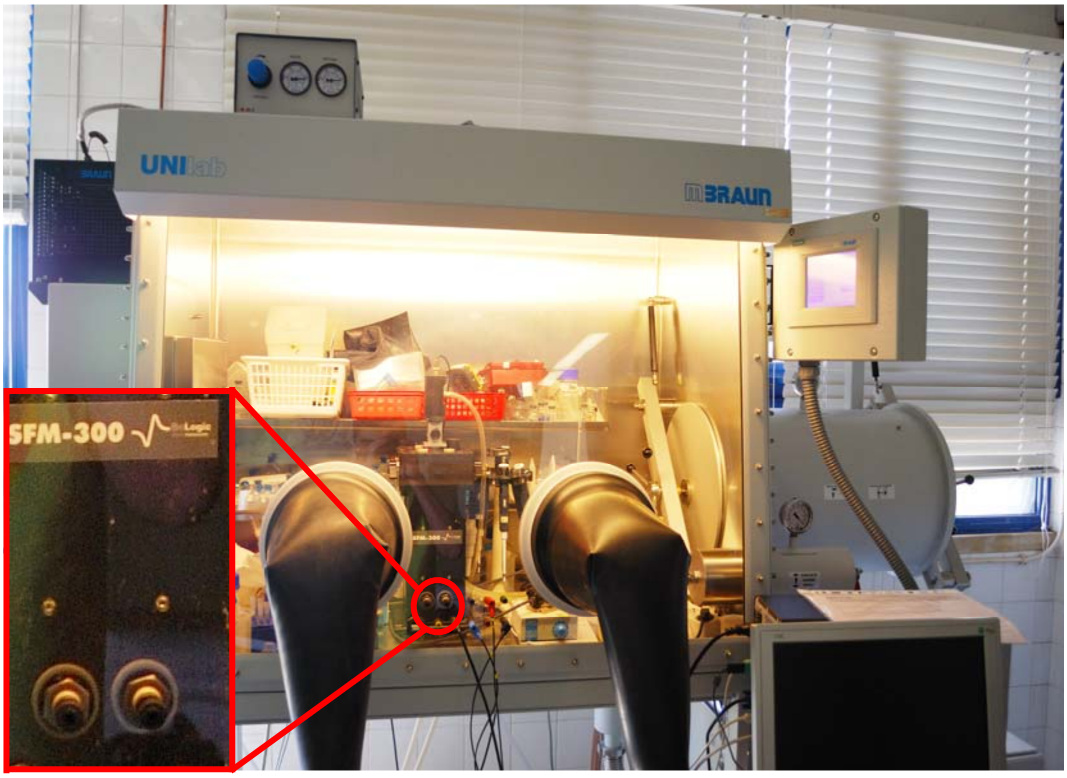

Figure B. 3 – Anaerobic stopped-flow apparatus (SFM-300 from Bio-Logic) installed inside a UniLab glove box (from mBraun). The inset shows the custom made connectors designed to fit the equipment that is used for the anaerobic RFQ experiments.

B.3 – Closed-Cycle Refrigerator (CCR) Mössbauer spectrometer: a general overview

As has been showed in this thesis, Mössbauer spectroscopy is very useful to characterize iron containing proteins. However, because of the spectroscopic properties of these samples it is necessary to achieve very low temperatures to obtain significant data. This process can be very expensive if we consider that most of the times the cryogenic temperatures are obtained using liquid Helium.

In the Mössbauer facility installed in Chemistry Department of Faculdade de Ciências e Tecnologia da Universidade Nova de Lisboa, the low temperatures are achieved with a Closed-Cycle Refrigerator (CCR). The CCR is used to cool down the sample reaching temperatures that range from 4.2 K to 325 K. This type of equipment circulates a fixed volume of gas during operation and is based on the Gifford-McMahon thermodynamic cycle, based on the controlled compression and expansion of helium gas.

In this type of refrigerators a compressor unit is used to provide the high pressure helium gas needed for the cycle. This unit is physically separated from Mössbauer spectrometer. The connection is made via flexible pressure tubes with self-sealing screw-couplings, virtually excluding any loss of helium gas even when screwed on and off repeatedly. The refrigerator includes two cold stages, one for cooling the sample and one for cooling a radiation shield that surrounds the sample.

This separation between compressor unit and cold head proved to be the great advantage of the Gifford-McMahon principle. This provides higher flexibility as the lighter weight cold head can be operated in any mounting position.

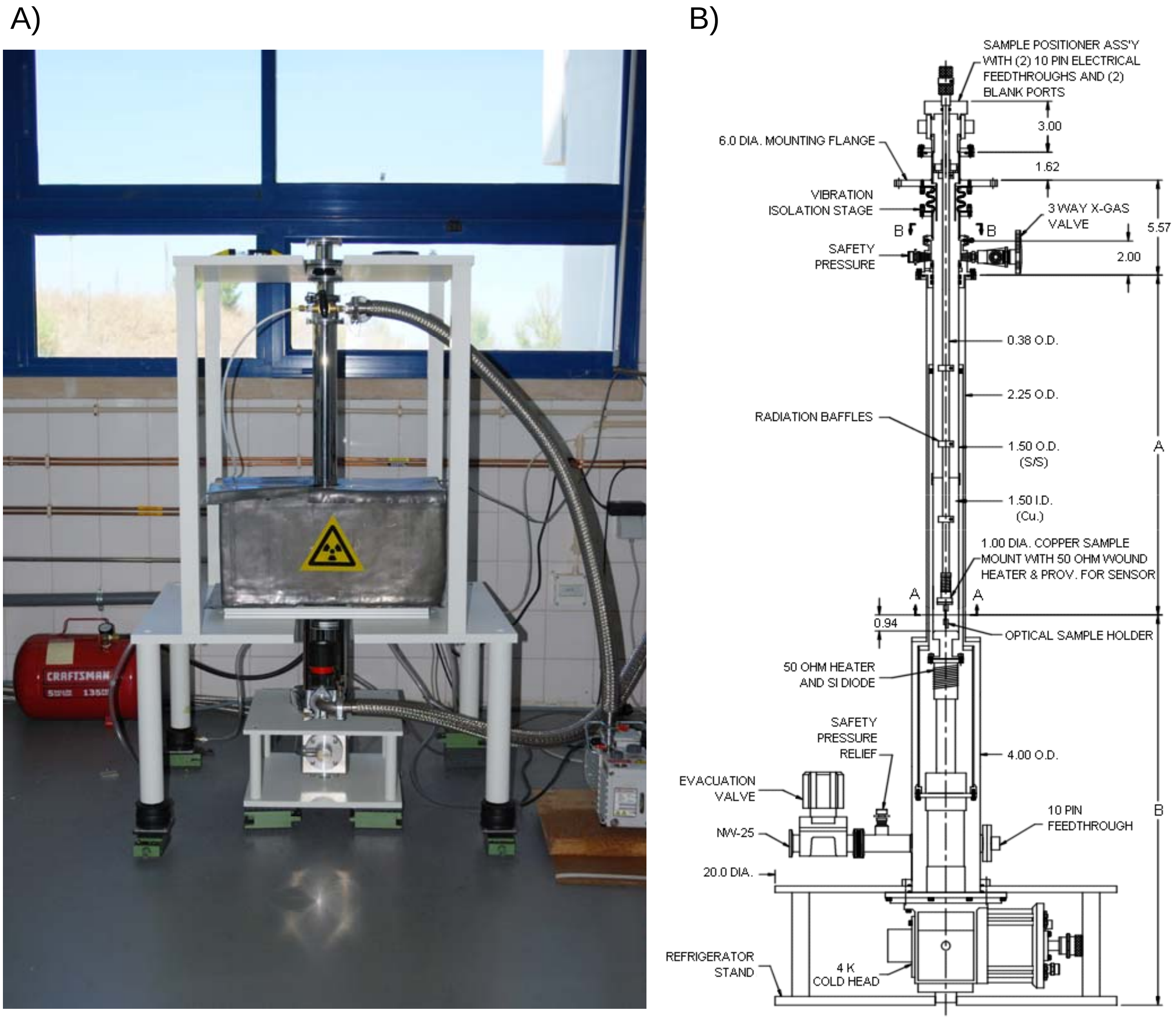

Figure B. 4 – A) Weak field Mössbauer spectrometer installed in Chemistry Department of Faculdade de Ciências e Tecnologia da Universidade Nova de Lisboa. B) Schematic figure of a Mössbauer spectrometer equipped with a CCR, adapted from[3].

In a simplified view, the Gifford-McMahon principle can be divided into four steps (see figure B.5).

1. The displacer is on the left-hand side of the expansion volume (V) which in this position corresponds to the dead volume. The low-pressure side is blocked by the respective valve position, the high-pressure side is opened. In the pV diagram this means a rise from low pressure (p_L) toward high pressure (p_H) at constant minimum volume (V_{min})
2. The displacement piston is drawn back, with the high-pressure valve open, whereby the volume (V), at constant pressure p_H increases to its maximum value (V_{max}).
3. Now the high-pressure valve (H) is closed and the low-pressure valve (L) is opened. The helium gas expands from pressure p_H to pressure p_L at constant volume V_{max}.
4. Now, at constant pressure p_L, the displacer is brought to its initial position whereby the helium gas cycle is completed.

The theoretical value of the transferred amount of heat during one cycle corresponds to the rectangular area in the pV diagram:

$$Q_{ideal} = (V_{max} - V_{min}) (p_H - p_L) \qquad \text{Eq. B1}$$

In the cold head the high-pressure or low-pressure helium gas is controlled by means of a rotary valve fitted on the shaft of an electric synchronous motor. The rotary valve rotates on the control disk. The displacer with integrated regenerator is pneumatically actuated by a control piston. Through additional holes in the control disk the control chamber is supplied alternatingly with high pressure and low pressure by means of the control piston. The operating frequency is around 2 Hz.

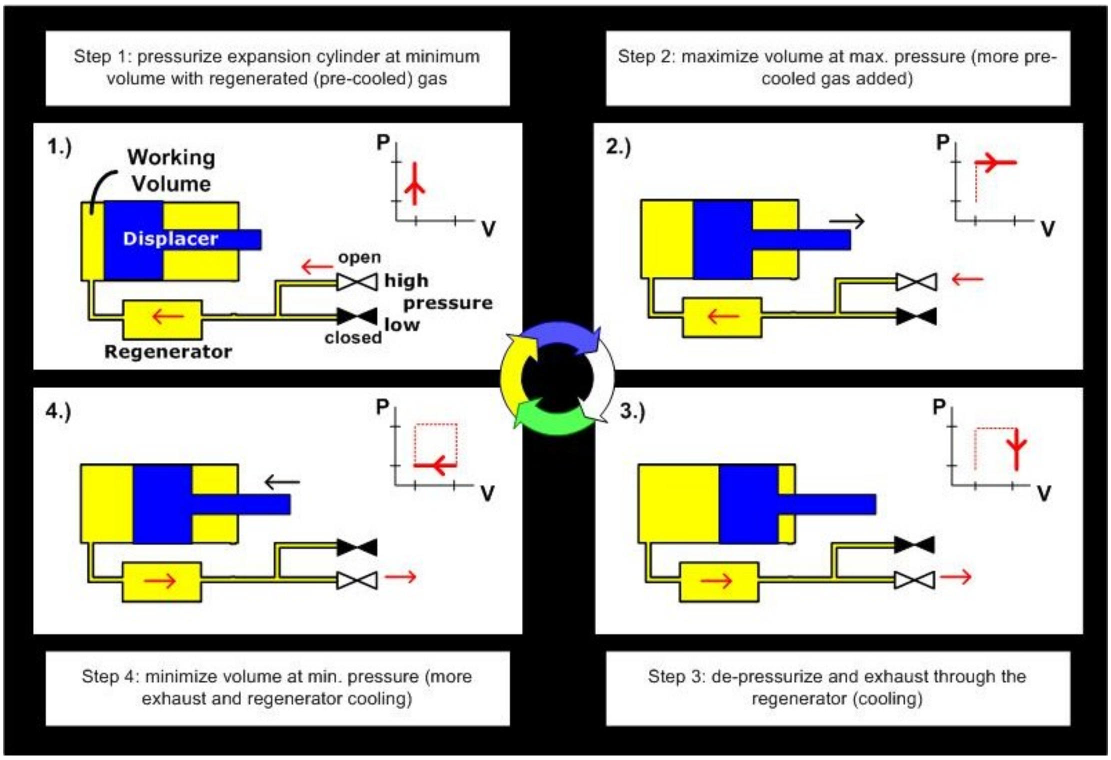

Figure B. 5 – Generic scheme of the Gifford-McMahon principle used in Closed-Cycle Refrigerators. Adapted from [4, 5].

B.4 – References

[1] Bio-Logic, http://www.bio-logic.info/rapid-kinetics/spectros.html#spectros_2, 2008.

[2] N. Ravi, J.M. Bollinger, B.H. Huynh, D.E. Edmondson, J. Stubbe, Mechanism of Assembly of the Tyrosyl Radical-Diiron(Iii) Cofactor of Escherichia-Coli Ribonucleotide Reductase .1. Mossbauer Characterization of the Diferric Radical Precursor, J. Am. Chem. Soc. 116 (1994) 8007-8014.

[3] Janis, http://www.janis.com/p-a4k23.html, (2008).

[4] E.S.R. F., http://www.esrf.eu/exp_facilities/ID18/pages/exp/cryo/ccr/ccr.html#pictures, (2008).

[5] Janis, http://www.janis.com/p-ccrs2.html, 2008.